Helmholtz-Zentrum Potsdam
Deutsches
GeoForschungsZentrum

Kaifei He

GNSS Kinematic Position and Velocity Determination for Airborne Gravimetry

Scientific Technical Report STR15/04

www.gfz-potsdam.de

Recommended citation:

He, K. (2015), DGNSS Kinematic Position and Velocity Determination for Airborne Gravimetry. *Scientific Technical Report 15/04, GFZ German Research Centre for Geosciences*. doi: 10.2312/GFZ.b103-15044.

Imprint

HELMHOLTZ CENTRE POTSDAM
**GFZ GERMAN RESEARCH CENTRE
FOR GEOSCIENCES**

Telegrafenberg
D-14473 Potsdam

Published in Potsdam, Germany
March 2015

ISSN 2190-7110

DOI: 10.2312/GFZ.b103-15044
URN: urn:nbn:de:kobv:b103-15044

This work is published in the GFZ series
Scientific Technical Report (STR)
and electronically available at GFZ website
www.gfz-potsdam.de

GNSS Kinematic Position and Velocity Determination for Airborne Gravimetry

Zur GNSS-basierten Bestimmung von Position und Geschwindigkeit in der Fluggravimetrie

vorgelegt von
M. Eng.
Kaifei He
geb. in Xianyang, Shaanxi, China

von der Fakultät VI – Planen Bauen Umwelt
der Technischen Universität Berlin
zur Erlangung des akademischen Grades

Doktor der Ingenieurwissenschaften
– Dr.-Ing. –

genehmigte Dissertation

Promotionsausschuss:
Vorsitzender: Prof. Dr.-Ing. Dr. h.c. Harald Schuh
Gutachter: Prof. Dr.-Ing. Frank Neitzel
Gutachter: Prof. Dr.-Ing. Frank Flechtner
Gutachter: Prof. Dr. Phil. nat. Markus Rothacher (ETH Zürich)

Tag der wissenschaftlichen Aussprache: 03. Dezember 2014

Berlin 2015

Scientific Technical Report STR 15/04
DOI: 10.2312/GFZ.b103-15044

Deutsches GeoForschungsZentrum GFZ

Abstract

The Global Navigation Satellite System (GNSS) plays a significant role in the fields of airborne gravimetry. The objective of this thesis is to develop reliable GNSS algorithms and software for kinematic highly precise GNSS data analysis in airborne gravimetry. Based on the requirements for practical applications in airborne gravimetry and shipborne gravimetry projects, the core research and the contributions of this thesis are summarized as follows:

Estimation Algorithm: Based on the accuracy requirements for GNSS precise positioning in airborne gravimetry, the estimation algorithms of least squares including the elimination of nuisance parameters as well as a two-way Kalman filter are applied to the kinematic GNSS data post-processing. The goal of these adjustment methods is to calculate non-epoch parameters (such as system error estimates or carrier phase ambiguity parameters) using all data in the first step, followed by the calculation of epoch parameters (such as position and velocity parameters of the kinematic platform) at every epoch. These methods are highly efficient when dealing with massive amounts of data, and give the highly precise results for the GNSS data analyzed.

Accuracy Evaluation and Reliability Analysis: The accuracy evaluation and reliability analysis of the results from precise kinematic GNSS positioning is studied. A special accuracy evaluation method in GNSS kinematic positioning is proposed, where the known distances among multiple antennas of GNSS receivers are taken as an accuracy evaluation index. The effect of the GNSS receiver clock error in the accuracy evaluation for GNSS kinematic positioning results of a high-speed motion platform is studied and a solution is proposed.

Kinematic Positioning Based on Multiple Reference Stations Algorithms: In order to overcome the problem of decreasing accuracy in GNSS relative kinematic positioning for long baselines, a new relative kinematic positioning method based on a priori constraints for multiple reference stations is proposed. This algorithm increases the accuracy and reliability of kinematic positioning results for large regions resp. long baselines.

GNSS Precise Positioning Based on Robust Estimation: In order to solve the problem of outliers occurring in positioning results which are caused by the presence of gross errors in the GNSS observations, a robust estimation algorithm is applied to eliminate the effects of gross errors in the results of GNSS kinematic precise positioning.

Kinematic Positioning Based on Multiple Kinematic Stations: In airborne gravimetry, multiple antennas of GNSS receivers are usually mounted on the kinematic platform. Firstly, a GNSS kinematic positioning method based on multiple kinematic stations is proposed. Using the known constant distances among the multiple GNSS antennas, a kinematic positioning method based on a priori distance constraints is proposed to improve the reliability of the system. Secondly, such an approach is also used for the estimation of a common atmospheric wet delay parameter among the multiple GNSS antennas mounted on the platform. This method does not only reduce the amount of estimated parameters, but also decreases the correlation among the atmospheric parameters.

Kinematic Positioning Based on GNSS Integration (GPS and GLONASS): To improve the reliability and accuracy of kinematic positioning, a kinematic positioning method using multiple GNSS systems integration is addressed. Furthermore, a GNSS integration algorithm based on Helmert’s variance components estimation is proposed to adjust the weights in a reasonable way. This improves the results when combining data of the different GNSS systems.

Velocity Determination Using GNSS Doppler Data: Airborne gravimetry requires instantaneous velocity results, thus raw Doppler observations are used to determine the kinematic instantaneous velocity in high-dynamic environments. Furthermore, carrier phase derived Doppler observations are used to obtain precise velocity estimates in low-dynamic environments. Then a method of Doppler velocity determination based on GNSS integration with Helmert’s variance components estimation and robust estimation is studied.

Software Development and Application: In order to fulfill the actual requirements of airborne as well as shipborne gravimetry on GNSS precise positioning, a software system (HALO_GNSS) for precise kinematic GNSS trajectory and velocity determination for kinematic platforms has been developed. In this software, the algorithms as proposed in this thesis were adopted and applied. In order to evaluate the effectiveness of the proposed algorithm and the HALO_GNSS software, this software is applied in airborne as well as shipborne gravimetry projects of GFZ Potsdam. All results are compared and examined, and it is shown that the applied approaches can effectively improve the reliability and accuracy of the kinematic position and velocity determination. It allows the kinematic positioning with an accuracy of 1-2 cm and the velocity determination with an accuracy of approximately 1 cm/s using raw and approximately 1 mm/s using carrier phase derived Doppler observations.

Keywords: GNSS, Kinematic Precise Positioning, Airborne Gravimetry, Least Squares, Nuisance Parameter Elimination, Two-way Kalman filter, Receiver Clock Error, Multiple Reference Stations, Robust Estimation, Multiple Kinematic Stations, A Priori Distance Constraint, Common Troposphere Parameterization, GNSS Integration, Helmert’s Variance Components Estimation, Doppler Velocity Determination, GEOHALO, HALO, HALO_GNSS.

Zusammenfassung

Das weltumspannende Satelliten-Navigationssystem GNSS spielt eine wichtige Rolle für die Fluggravimetrie. Gegenstand dieser Arbeit ist die Entwicklung zuverlässiger GNSS-Algorithmen und Software für die hochgenaue GNSS-Datenanalyse in der Fluggravimetrie. Ausgehend von den Anforderungen für praktische Anwendungen der Fluggravimetrie lassen sich die Beiträge und Schwerpunkte dieser Dissertation wie folgt zusammenfassen:

Ausgleichs- bzw. Schätzungs-Algorithmen: Ausgehend von den Genauigkeitsanforderungen an die GNSS-basierte Positionsbestimmung in der Fluggravimetrie werden in einer kinematischen GNSS-Daten-Auswertung eine Schätzung nach kleinsten Quadraten einschließlich der Eliminierung von Störparametern sowie ein Zwei-Wege-Kalman-Filter angewendet. Das Ziel der beiden Ausgleichsverfahren ist es, an jedem Messzeitpunkt zunächst globale Parameter (wie System-Fehler und Trägerwellen-Ambiguities) und anschließend lokale Parameter (wie Position und Geschwindigkeit der bewegten Messplattform) zu bestimmen. Die angewandten Methoden sind sehr effizient und ergeben hochpräzise Resultate für die GNSS-Datenanalyse.

Analyse von Genauigkeit und Zuverlässigkeit: Die Genauigkeit und Zuverlässigkeit der Resultate der präzisen kinematischen GNSS-Positionsbestimmung werden untersucht. Dabei wird eine besondere Methode zur Bewertung der Genauigkeit der kinematischen GNSS-Positionsbestimmung vorgeschlagen, wo bekannte Entfernungen zwischen mehreren GNSS-Antennen als Genauigkeits-Maßstab genommen werden. Weiterhin wird der Einfluss der Uhrenfehler der GNSS-Empfänger auf die Genauigkeit der kinematischen Positionsbestimmung für die Hochgeschwindigkeits-Plattform untersucht. Für dabei auftretende Probleme wird eine Lösung vorgeschlagen.

Algorithmen der kinematischen Positionsbestimmung die auf mehreren Referenzstationen beruhen: Um das Problem der im Falle langer Basislinien abnehmenden Genauigkeit in der relativen kinematischen GNSS-Positionsbestimmung zu bewältigen, wird ein neuer Algorithmus vorgeschlagen. Er beruht auf der apriori Einführung von Exzentrizitäts-Bedingungen für mehrere Referenzstationen. Dieser Algorithmus erhöht die Genauigkeit und Zuverlässigkeit der Ergebnisse in der kinematischen Positionsbestimmung für große Regionen resp. lange Basislinien.

Präzise GNSS-Positionsbestimmung, beruhend auf robuster Schätzung: Das Vorhandensein von groben Fehlern in den GNSS-Beobachtungen verursacht das Auftreten von Ausrei-

ßern in den Ergebnissen der Positionsbestimmung. Um dieses Problem zu überwinden, wird ein robuster Ausgleichungs-Algorithmus angewendet, der die Auswirkungen von groben Fehlern in den Ergebnissen der kinematischen GNSS-Positionsbestimmung beseitigt.

Kinematische Positionierung auf der Basis mehrerer bewegter Stationen: In der Fluggravimetrie werden in der Regel mehrere GNSS-Antennen auf einer bewegten Plattform installiert. In diesem Zusammenhang wird deshalb erstens ein kinematisches GNSS-Positionsbestimmungsverfahren vorgeschlagen, das auf mehreren gleichzeitig bewegten GNSS-Stationen basiert. Aus den bekannten, konstanten Distanzen zwischen den GNSS-Antennen werden dabei apriori Exzentrizitäts-Bedingungen abgeleitet und in die Positionsschätzung eingeführt. Dies verbessert die Zuverlässigkeit des Messsystems. Zweitens wird solch ein Ansatz auch zur Bestimmung eines gemeinsamen Refraktionsparameters aller GNSS-Antennen der Plattform für den feuchten Teil der Atmosphäre verwendet. Dieses Verfahren reduziert nicht nur die Menge der geschätzten Parameter, sondern verringert auch die Korrelation zwischen den atmosphärischen Parametern.

Kinematische Positionierung basierend auf der Kombination verschiedener GNSS-Systeme: Um die Zuverlässigkeit und Genauigkeit der kinematischen Positionsbestimmung zu verbessern, werden die Signale mehrerer GNSS-Systeme (d.h. GPS und GLONASS) gemeinsam registriert und ausgewertet (sog. GNSS-Integration). Zur Optimierung des relativen Gewichts zwischen den Daten der verschiedenen GNSS-Systeme wird die Helmertsche Varianz- Komponenten-Schätzung angewandt. Der auf dieser Basis entwickelte Kombinationsalgorithmus ermöglicht die Verbesserung der Beiträge von mehreren GNSS-Systemen.

Geschwindigkeitsbestimmung mit GNSS-Doppler-Daten: Die Auswertung der Schwere-Messdaten in der Fluggravimetrie verlangt die hochgenaue Bestimmung des Geschwindigkeitsvektors der bewegten Plattform. Deshalb werden rohe GNSS-Doppler-Beobachtungen verwendet, um die Geschwindigkeit der bewegten Plattform im Falle hoch-dynamischer Flugbedingungen kinematisch zu bestimmen. Darüber hinaus werden aus der Trägerphase abgeleitete Doppler-Beobachtungen verwendet, um präzise Geschwindigkeitsschätzungen im Falle weniger dynamischer Flugbedingungen zu erhalten. Die Kombination verschiedener GNSS-Systeme wird auch bei der Doppler-Geschwindigkeitsbestimmung angewandt. Hierzu wird die Anwendung der Helmertschen Varianzkomponenten-Schätzung und einer robuste Schätzung untersucht.

Software Entwicklung und Anwendung: Um die aktuellen Anforderungen der GNSS-basierten Positionsbestimmung in der Flug- sowie Schiffsgravimetrie zu erfüllen, wurde ein Software-System (HALO_GNSS) für die präzise kinematische GNSS-Flugbahn- und Ge-

schwindigkeitsberechnung kinematischer Plattformen entwickelt. Die in dieser Arbeit vorgeschlagenen Algorithmen wurden in diese Software integriert. Um die Effizienz der vorgeschlagenen Algorithmen und der HALO_GNSS Software zu prüfen, wurde diese Software sowohl in Flug- aus auch in Schiffsgravimetrie-Projekten des GFZ Potsdam angewandt. Alle Ergebnisse werden verglichen und geprüft und es wird gezeigt, dass die angewandten Methoden die Zuverlässigkeit und Genauigkeit der kinematischen Positions- und Geschwindigkeitsbestimmung effektiv verbessern. Die Verwendung der Software HALO_GNSS ermöglicht kinematische Positionsbestimmung mit einer Genauigkeit von 1-2 cm sowie Geschwindigkeitsbestimmung mit einer Genauigkeit von ca. 1 cm/s mit Roh- und etwa 1 mm/s mit aus der Trägerphase abgeleiteten Doppler-Beobachtungen.

Stichworte: GNSS, Kinematische präzise Positionsbestimmung, Fluggravimetrie, Ausgleichung nach kleinsten Quadraten, Parameter-Eliminierung, Zwei-Wege-Kalman-Filter, GNSS-Uhrfehler, Mehrfache Referenzstationen, Robuste Schätzung, Mehrfache bewegte GNSS-Stationen, A Priori Exzentrizitäts-Bedingungen, Gemeinsame Troposphären-Parametrierung, GNSS-Integration, Helmertsche Varianzkomponenten-Schätzung, Doppler-basierte Geschwindigkeits-Bestimmung, GEOHALO, HALO, HALO_GNSS.

Table of Contents

List of Figures

List of Tables

List of Abbreviations

AC	Analysis Center
AdV	Arbeitsgemeinschaft der Vermessungsverwaltungen der Länder der Bundesrepublik Deutschland (i.e. the Working Committee of the Surveying Agencies of the States of the Federal Republic of Germany)
ARP	Antenna Reference Point
BDS	the Chinese BeiDou navigation Satellite System
BKG	Bundesamt für Kartographie und Geodäsie (i.e. Federal Agency for Cartography and Geodesy, Germany)
BMBF	Bundesministerium für Bildung und Forschung (i.e. German Federal Ministry for Education and Research)
C/A	Coarse/Acquisition code
CDDIS	Crustal Dynamics Data Information System
CDMA	Code Division Multiple Access
CODE	Centre of Orbit Determination in Europe
CORS	Continuously Operating Reference Stations
CS	Commercial Service
DCB	Differential Code Biases
DD	Double Difference
DF	Dual-Frequency
DFG	Deutsche Forschungsgemeinchaft (i.e. German Research Foundation)
DLR	Deutsches Zentrum für Luft- und Raumfahrt (i.e. German Aerospace Centre)
DOD	the U.S. Department of Defense
ECMWF	European Centre for Medium-Range Weather Forecasts
ESA	European Space Agency
EU	European Union
EX_WL	Extra-widelane Linear Combination
FDMA	Frequency Division Multiple Access
Galileo	the European Union satellite navigation system
GEO	Satellites in Geostationary Orbit
GEOHALO	GEOscience High Altitude and LOng range research project
GFZ	Helmholtz-Zentrum Potsdam Deutsches-GeoForschungsZentrum (i.e. Helmholtz-Centre Potsdam-GFZ German Research Centre for

	Geosciences)
GIM	Global Ionospheric Map
GLONASS	the Russian GLObal NAvigation Satellite System
GLOT	GLONASS Time
GMF	Global Mapping Function
GNSS	Global Navigation Satellite System
GPS	Global Positioning System
GPST	GPS Time
HALO	High Altitude and LOng range airborne gravimetric project
HGF	Helmholtz-Gemeinschaft forscht (i.e. Helmholtz Association)
IAR	Integer Ambiguity Resolution
IGR	IGS Rapid orbit
IGS	International GNSS Service
IGSO	Inclined Geosynchronous Orbit
IGU	IGS Ultra-rapid orbit
INS	Inertial Navigation System
IOV	In-Orbit Validation
IRNSS	Indian Regional Navigation Satellite System
ITRF	International Terrestrial Reference Frame
KIT	Karlsruher Institut für Technologie (i.e. Karlsruhe Institute for Technology)
KNITs	Coordination Scientific Information Centre of the Russia
LC	Ionosphere-free Linear Combination
LEO	Low Earth Orbit
MDB	Minimal Detectable Bias
MEO	Medium altitude Earth Orbit
MET	Meteorology
MPG	Max-Planck-Gesellschaft (i.e. Max Planck Society)
MW_WL	MW Widelane Linear Combination
NASA	National Aeronautics and Space Administration
NOAA	National Oceanic and Atmospheric Administration
NRTK	Network-based Real Time Kinematic positioning
OCS	Operational Control Segment
OS	Galileo are Open Service
PCO	Phase Centre Offsets
PCV	Phase Centre Variation
PLL	Phase Lock Loop

PNT	Positioning, Navigation and Timing
PPP	Precise Point Positioning
PPP-RA	Precise Point Positioning Regional Augmentation
PPS	Precise Positioning Service
PRS	Public Regulated Service
PRN	Pseudo-Random Noise
PZ-90	Parametry Zemli 1990
QZSS	Quasi-Zenith Satellite System of Japan
RMS	Root Mean Square
RTK	Real-Time Kinematics
SAPOS	Satellite Positioning Service of the German State Survey
SAR	Search and Rescue
SD	Single Difference
SDev	Standard Deviation
SoL	Safety-of-Life Service
SP3	IGS Standard Product 3
SPS	Standard Positioning Service
STD	Slant Total Delay
UPD	Un-calibrated Phase Delays
USNO	US Naval Observatory
USSR	Union of Soviet Socialist Republics
UTC	Coordinated Universal Time
VCE	Variance Components Estimation
WL	Widelane Combination
WGS-84	World Geodetic System 1984
ZHD	Zenith Hydrostatic Delay
ZTD	Zenith Total Delay
ZWD	Zenith Wet Delay

1 Introduction

1.1 Motivation

Precise kinematic position and velocity determination based on the Global Navigation Satellite System (GNSS) is widely used in many scientific research and engineering fields, such as geodesy, spatial science, geophysics and meteorology (Chen, 1998; Leick, 2004, p. 2; Hofmann-Wellenhof et al., 2008, pp. 1-12; Xu, 2007, p. 1). Meanwhile, measuring the Earth's gravity field is one of the most important activities in scientific and economic applications, such as geodesy, geophysics, exploration purposes, geoid determination and satellite orbits prediction (Kwon and Jekeli, 2001; Kreye and Hein, 2003). In this context, airborne gravimetry plays a very important role in recovering the Earth's gravity field in the range of medium to high frequencies, which then closes the gap between the terrestrial gravity filed measurements on the ground and the global gravity models based on the satellite gravimetry at wavelengths between 1 and 100-200 km (Hein, 1995; Kwon and Jekeli, 2001).

In the fields of airborne gravimetry, GNSS position and velocity determination plays a significant role as well (Forsberg and Olesen, 2010), since the state information of a kinematic platform with an airborne gravimeter can be obtained independently from the GNSS observations. The trajectory and attitude of such a kinematic platform are indispensable information for analysing its airborne gravimetry data. The acceleration information as derived from the position and/or velocity information for such a kinematic platform can be used to separate the disturbing kinematic accelerations affecting the airborne platform from the gravitational signal. Therefore, the estimation of accurate state information for such a kinematic platform by precise GNSS position and velocity determination is the key factor for any successful implementation of airborne gravimetry (Torge, 1989; Hannah, 2001; Kreye and Hein, 2003). More details about the principle of airborne gravimetry are given in Section 1.2.1.

However, there are still many remaining challenges in the application of GNSS position and velocity determination in airborne gravimetry. Firstly, the novel airborne gravimetric project GEOHALO on the German High Altitude and Long Rang Research Aircraft HALO (cf. Section 1.2.2), which is characterized by its high-altitude, long-range and high dynamics, requires more accurate and reliable GNSS-based state information for the kinematic platform than before in "traditional" airborne gravimetry. Secondly, the rapid development of multiple GNSS systems (GPS, GLONASS, etc.) provides more information and new opportunities (cf. Section 1.2.3) for improving the accuracy and reliability of the GNSS results for kinematic platforms. In this study, the algorithms and methods for the multiple GNSS systems are applied and analyzed. Finally, most of the currently available GNSS software tools incl. the therein adopted methods do not meet the requirements for HALO. For instance, the usage of multiple GNSS systems is not possible in some software systems like GAMIT (Herring et al., 2010) or HALO_GPS (Wang et al., 2010). Furthermore, some of the GNSS software systems like the RTKLIB (Takasu, 2013) cannot exploit information of multiple reference stations for large regions. And most of the GNSS software cannot provide velocity information of a kinematic platform. Therefore, new algorithms and software have to be developed to fulfill the requirements of the novel airborne gravimetry on HALO. Thus, the objective of this thesis is the development, application and evaluation of specific precise and reliable GNSS algorithms and software of kinematic GNSS data analysis for airborne gravimetry on the high-altitude and long-range aircrafts like HALO.

1.2 Background

1.2.1 The Role of GNSS Application in Airborne Gravimetry

Airborne gravimetry is an emerging technology that provides a powerful tool for both geodesy and geophysical exploration. Using airborne techniques, detailed local and regional gravity field information can be collected in a rapid and cost-effective manner (Bruton et al., 1999). For instance, it is used for geoid determination and for mapping of gravity anomalies in the contest of geophysical exploration (Forsberg and Olesen, 2010).

The idea of using an airborne platform for gravity measurements is not completely new. It has been attempted since the 1960s (Lacoste, 1967; Schwarz and Wei, 1995), and recognized that if an appropriate level of accuracy could be achieved airborne gravimetry would be vastly superior in economy and efficiency to point-wise terrestrial gravimetry (Alberts, 2009). In the beginning, airborne gravimetry did not become a major tool for gravity filed mapping, although the first experiments gave promising results (Thompson and LaCoste, 1960). The reason is the disturbing kinematic accelerations of the aircraft which are very difficult to determine due to the lack of sufficient navigation technologies at that time (Hannah, 2001). Nevertheless, in the late 1980s and early 1990s this situation rapidly improved with the availability of the Global Positioning System (GPS) and the development of kinematic positioning using its carrier phase signals. Meanwhile, the accuracy of GNSS-based trajectory and velocity determination for airborne gravimetry has reached a useful level (Torge, 1989; Hannah, 2001).

In principle, airborne gravimetry requires both a device determining the sum of all gravity and kinematic accelerations affecting the airborne platform, plus a positioning system (such as radar, laser altimeter, or GNSS) for the determination of the kinematic accelerations alone (Hannah, 2001). The gravity vector is determined by differencing between them. The basic principle is shown in Figure 1.1.

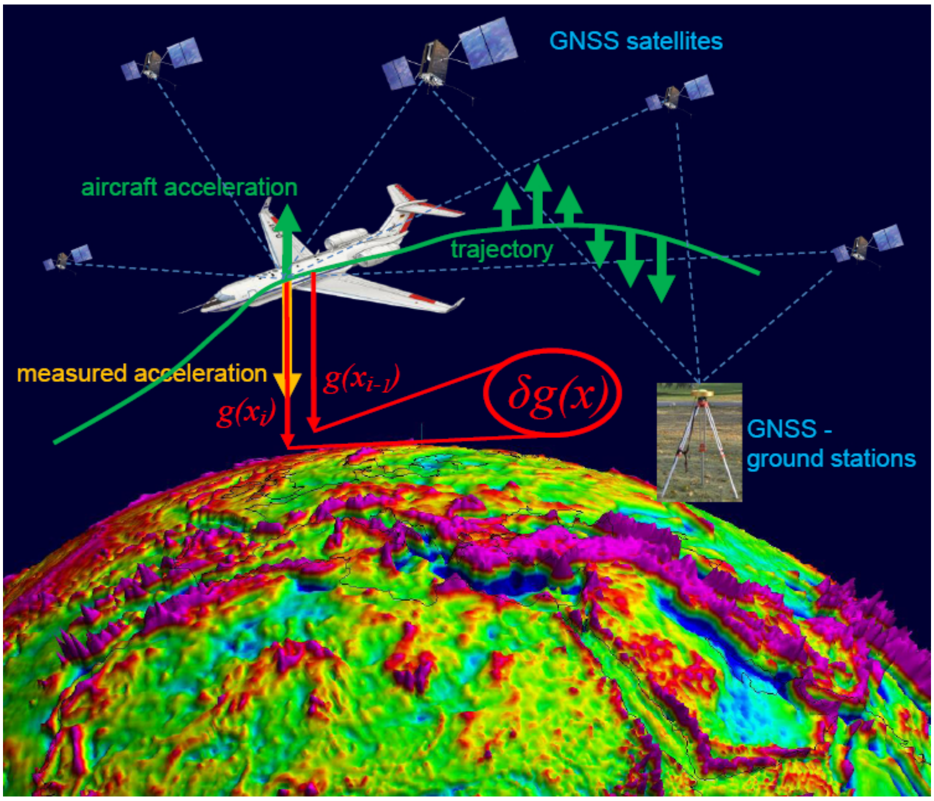

Figure 1.1: Basic principle of the airborne gravimetry (GFZ, 2013)

In Figure 1.1, the yellow arrow means the superposition of all vertical accelerations (a) measured by the gravimeter inside of the airplane. The green arrow indicates the non-gravitational kinematic acceleration ($\ddot{x}$) to be estimated from the GNSS-recorded trajectory and/or velocity. The difference between the measured and the kinematic accelerations is the gravity acceleration (g) at the trajectory (GFZ, 2013) which can be expressed in the following basic formula as

$$g = a - \ddot{x} . \tag{1.1}$$

Airborne gravimetry techniques face a number of difficulties that typically do not occur in the classical field of gravimetry on the ground or on slowly moving vessels like ships. Some of these difficulties are given by Torge (1989, p. 287) and Hannah (2001):

- The high platform velocities require short averaging times and high position and particularly velocity accuracies.
- Elevation changes (uncertainties) directly influence the measured value of gravity.

- The power of the gravity field (especially the short-wavelength part), attenuates steadily with altitude thus causing the signal-to-noise ratio to decrease at a higher altitude. In general, an increase of the altitude of the aircraft decreases the resolution capability of the gravimetric system at short wavelengths.

As mentioned above, GNSS is used for the reduction of the disturbing non-gravitational accelerations of the measuring kinematic platform. GNSS allows for a highly accurate estimation of position and velocity. Hence, precise GNSS position and velocity determination is widely used, and plays a significant role in the field of airborne gravimetry (Kreye and Hein, 2003; Petrovic et al., 2013).

1.2.2 The New Airborne Gravimetric Project

The High Altitude and LOng Range (HALO) project is a joint new project of several German institutes for atmospheric research and Earth observation (DLR, 2013b). The main project partners are the German Federal Ministry for Education and Research (BMBF), the German Centre for Aeronautics and Space Research (DLR), the German Research Foundation (DFG), the Max Planck Society (MPG) and the Helmholtz Association (HGF) incl. its members Research Centre Juelich (Forschungszentrum Jülich), Karlsruhe Institute for Technology (KIT) and German Research Centre for Geosciences (GFZ).

The new German HALO aircraft is a business jet G550 produced by the Gulfstream Aerospace Corporation, shown in Figure 1.2. The aircraft has a spacious cabin for installing various atmospheric and remote sensing equipment and instruments, which makes the HALO aircraft an extraordinary platform for atmospheric and geophysical research.

Figure 1.2: The HALO aircraft (DLR, 2013b)

The goal of the GEOHALO project is an aircraft-based geodetic-geophysical survey over the whole territory of Italy and adjacent regions of the Mediterranean using a variety of measurement systems and remote sensing equipment mounted on the HALO aircraft. The main fields of the GEOHALO project include: GNSS precise position and velocity determination, GNSS reflectometry (Semmling et al., 2013; Semmling et al., 2014), airborne gravimetry (Petrovic et al., 2013), magnetometry and laser altimetry (Scheinert et al., 2013).

From June 6 to 12, 2012, the GEOHALO mission conducted 4 flights, which started from the German Aerospace Centre (DLR) in Oberpfaffenhofen Germany, scanning around over Italy and the adjacent regions of the Mediterranean. Every flight lasted up to 10 hours and the flown trajectories had a total length of 16150 kilometres. The speed of the aircraft on the survey tracks was approximately 450 km/h. The flight altitude was about 3500 m (Scheinert et al., 2013; Heyde et al., 2013). GNSS precise position and velocity determination plays an important role in the whole project, since all remote sensing instruments and measuring devices are mounted on this kinematic platform. Therefore, precise information about the state of the platform is a prerequisite and a key factor for the successful accomplishment of the entire research project. In particular, the high speed of HALO is a challenge for the airborne gravimetry on this aircraft since “classical” airborne gravimetry is usually done on a smaller and slower aircraft.

1.2.3 The Development Status of GNSS

The advent of satellite navigation technologies has greatly changed the way of human's life and production. With the development during a few decades, GNSS has been applied widely in many areas, such as air, sea and land Positioning, Navigation and Timing (PNT), low earth orbit (LEO) satellite orbit determination, static and kinematic positioning, flight-state monitoring, sea surface monitoring (Galas et al., 2013; Semmling et al., 2014), atmospheric profiling (Haase et al., 2014), as well as surveying, etc. GNSS has become a necessity in daily life, industry, research and education (Xu, 2007, p. 1). The application of GNSS is limited by the human's imagination only.

GNSS includes several different satellite navigation systems, namely the Global Positioning System (GPS) developed by the United States, the GLObal NAvigation Satellite System (GLONASS) developed by Russia, Galileo developed by the European Union, the BeiDou navigation Satellite System (BDS) developed by China, the Quasi-Zenith Satellite System (QZSS) developed by Japan and the Indian Regional Navigation Satellite System (IRNSS) developed by India. As of April 2014, only GPS and GLONASS were fully globally operational. Galileo and BDS are in the process of growth. QZSS and IRNSS are regional satellite navigation system. All kinds of GNSS consist of three segments: the space, control and user segment (Hofmann-Wellenhof et al., 2008, pp. 6, 7; Yang et al., 2011a).

1.2.3.1 The Development Status of GPS

The Global Positioning System (GPS) is the earliest satellite navigation system. It was designed and built, and is operated and maintained by the U.S. Department of Defence (DOD). GPS permits land, sea, airborne and space users to determine their three-dimensional position, velocity and time 24 hours a day, in all weather, anywhere in the world with a precision and accuracy far better than other radio navigation systems available today or in the foreseeable future (NAVCEN, 2014).

The first GPS satellite was launched in 1978 and the system became fully operational in the mid-1990s. At the moment, the GPS constellation consists of about 30 satellites in six orbital planes with about five satellites in each plane. The GPS satellites fly in Medium Earth Orbits (MEO) at an altitude of approximately 20200 km. The orbital planes are inclined 55 degrees with respect to the equator. Each GPS satellite is in a nearly circular orbit with a semi-major axis of 26578 km and a period of about twelve hours, and circles the Earth twice a day (Xu, 2007, p. 2; Hofmann-Wellenhof et al., 2008, p. 322; NOAA, 2014b).

In April 2014, the GPS constellation consisted of 31 satellites, divided into four groups: 8 Block IIA, 12 Block IIR, 7 Block IIR(M) and 4 Block IIF. In the future, GPS satellite Block III will be launched, due to the GPS modernization. The major characteristics of each Block are shown in Table 1.1 (NOAA, 2014b).

Table 1.1: GPS satellite block characteristics in April 2014 (NOAA, 2014b)

Block	IIA	IIR	IIR(M)	IIF	III
Operational Satellite Number	8	12	7	4	0
Launch Period	1990-1997	1997-2004	2005-2009	Since 2010	Planning 2016
Design Life	7.5-year	7.5-year	7.5-year	12-year	15-year
CDMA Signals	L1, L2 P1, P2 C/A	L1, L2 P1, P2 C/A	L1, L2 P1, P2 C/A M1, M2 L2C	L1,L 2, L5 P1, P2 C/A M1, M2 L2C, L5C	L1, L2, L5 P1, P2 C/A M1, M2 L1C, L2C, L5C

The GPS satellites listed in Table 1.1 use the Code Division Multiple Access (CDMA) technique to transmit data on the L-band frequencies, L1 (1575.42 MHz), L2 (1227.60 MHz) and L5 (1176.45 MHz), depending on the block type of the particular satellite. The L1, L2 and L5 carrier frequencies are generated by multiplying the fundamental frequency (10.23 MHz) by 154, 120 and 115, respectively. Pseudorandom noise (PRN) codes, along with satellite ephemerides, ionospheric models and satellite clock corrections are superimposed onto the carrier frequencies L1, L2 and L5. The measured transmitting times of the signals that travel from the satellites to the receivers are used to compute the pseudoranges. The 1st civil signal Coarse-Acquisition (C/A) code, sometimes called the Standard Positioning Service (SPS), is a pseudorandom noise code that is modulated onto the L1 carrier. The precision (P) code, sometimes called the Precise Positioning Service (PPS), is modulated onto the L1, L2 and L5 carriers allowing for the removal of the effects of the ionosphere (Xu, 2007, p. 3). The transmission of the military M-code started with the launch of the Block IIR(M) satellites. The main characteristics of this military code are a higher resistance against jamming, increased navigation performance, higher security based on the new cryptography algorithms, and the possibility of higher transmission power, denoted as flex-power. The M-code is modulated onto the L1 and L2 carrier frequencies. The new civil signals L1C, L2C and L5C are modulated onto L1, L2 and L5, respectively. The 2nd civil signal L2C has been designed to meet in particular commercial needs. The 3rd civil signal L5C has been designed to especially meet the requirements of safety-of-life (SoL) applications. The 4th civil signal L1C has been designed to enable interoperability between GPS and the other international satellite navigation systems, such as Galileo, BDS, QZSS and IRNSS (Hofmann-Wellenhof et al., 2008, p. 336; NOAA, 2014b).

The Operational Control Segment (OCS) started to operate in 1985 and consists of a global network of ground facilities that track the GPS satellites, monitor their transmissions, perform analyses, and send commands and data to the constellation. The current OCS includes a master control station in Colorado Springs, an alternate master control station, 12 command and control antennas, and 16 monitoring sites. The locations of these facilities are shown in Figure 1.3 (NOAA, 2014a). The monitoring stations track all GPS satellites in view and collect ranging information from the satellite broadcasts. The monitoring stations send the information they collect from each of the satellites back to the master control station which computes precise satellite orbits. The information is then formatted into updated navigation messages for each satellite. The updated information is transmitted to each satellite via the ground antennas, which also transmit and receive satellite control and monitoring signals (Hofmann-Wellenhof et al., 2008, pp. 324-327; Xu, 2007, p. 3; Marreiros, 2012; NOAA, 2014a).

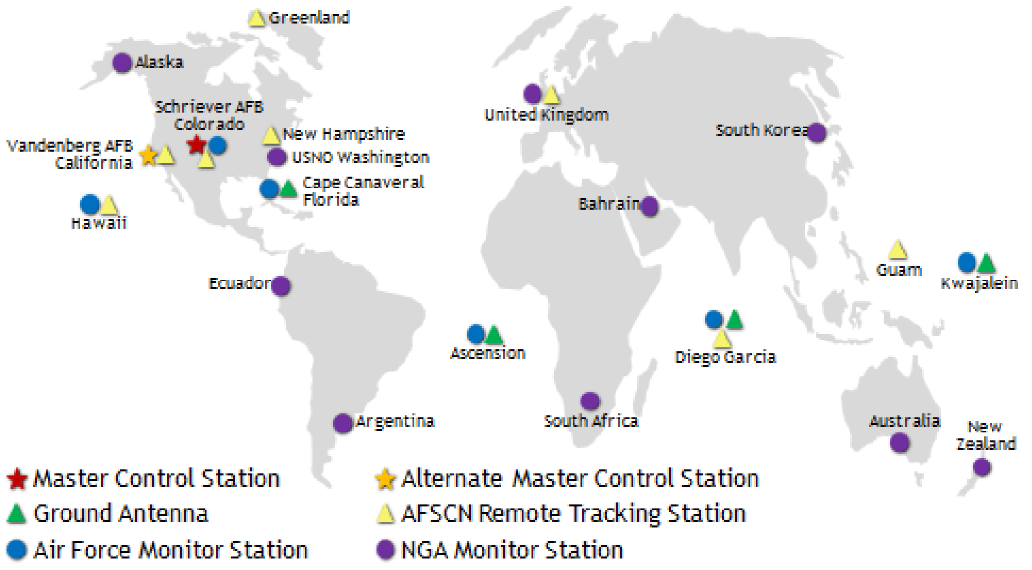

Figure 1.3: GPS control segment (NOAA, 2014a)

1.2.3.2 The Development Status of GLONASS

The GLObal Navigation Satellite System (GLONASS) is a satellite navigation system developed by the former Union of Soviet Socialist Republics (USSR) for military use. Now, GLONASS is managed by the Russian Space Forces and the system is operated by the Coordination Scientific Information Centre (KNITs) of the Ministry of Defence of the Russian Federation (Xu, 2007, p. 3).

The first GLONASS satellite was launched into orbit in 1982. The system consists of 24 satellites in three orbital planes, with three in-orbit spares. The ascending nodes of three orbital planes are separated by 120 degrees, and the satellites within the same orbit plane are equally spaced by 45 degrees. The arguments of latitude of satellites in equivalent slots in two different orbital planes differ by 15 degrees. Each satellite operates in a nearly circular orbit with a semi-major axis of 25510 km. Each orbital plane has an inclination angle of 64.8 degrees, and each satellite completes an orbit in approximately 11 hours 16 minutes (Xu, 2007, p. 3).

As of April 2014, 29 satellites were in orbit with 24 GLONASS-M satellites operational (IAC, 2014). In the future, GLONASS satellites GLONASS-K1, GLONASS-K2 and GLONASS-KM will be launched, due to the ongoing GLONASS modernization. The major characteristics of each type are shown in Table 1.2 (Revnivykh, 2012; IAC, 2014).

Table 1.2: GLONASS satellite characteristics in April 2014 (IAC, 2014)

Type	M	K1	K2	KM
Operational Satellite Number	24	0	0	0
Launch Period	2003-2016	2011-2014	2015-2024	Planning 2025
Design Life	7-year	10-year	10-year	12-year
FDMA Signals	G1F, G2F G1OF, G2OF G1SF, G2SF	G1F, G2F G1OF, G2OF G1SF, G2SF	G1F, G2F G1OF, G2OF G1SF, G2SF	G1F, G2F G1OF, G2OF G1SF, G2SF
CDMA Signals	G3C G3OC (from 2014)	G3C G3OC	G1C, G2C, G3C G1OC, G2OC, G3OC G1SC, G2SC	G1C, G2C, G3C G1OC, G2OC, G3OC G1SC, G2SC, G3SC
Interoperability CDMA Signals				G1CM, G3CM, G5CM G1OCM, G3OCM, G5OCM
Note	F: denotes FDMA. C: denotes CDMA. CM: denotes Interoperability CDMA. O: denotes standard-accuracy signal, likes C/A code of GPS. S: denotes high-accuracy signal, likes P code of GPS.			

As seen from Table 1.2, GLONASS implements the Frequency Division Multiple Access (FDMA) technique to differentiate among the signals of different satellites. In this way, the GLONASS satellites transmit coded signals in two frequencies located on two frequency bands, which can be computed by the simple formula (Leick et al., 1998; Habrich, 2000; Dach et al., 2007)

$$f_1^k = f_1^0 + k \cdot \Delta f_1 \tag{1.2}$$

and

$$f_2^k = f_2^0 + k \cdot \Delta f_2 , \tag{1.3}$$

where k denote frequency channel number, $k = -7, \ldots, +6$ (since 2005), it is part of the navigation message. $f_1^0 = 1602$ MHz, $f_2^0 = 1246$ MHz, $\Delta f_1 = 0.5625$ MHz, $\Delta f_2 = 0.4375$ MHz. From 2014 onward, the new GLONASS satellites will feature a full suite of modernized

CDMA signals in the existing G1 (1600.995 MHz), G2 (1248.04 MHz), G3 (1202.25 MHz) bands, which includes standard-accuracy signal and high-accuracy signal, respectively. GLONASS-KM satellites will increase the open signals (Interoperability CDMA Signals) to enable interoperability between GLONASS and the other international satellite navigation systems. The open signal G1OCM is modulated onto the G1 (1575.42 MHz), similar to modernized GPS signal L1C and Galileo/BDS signal E1. The open signal G3OCM is modulated onto the G3 (1207.14 MHz), similar to Galileo/BDS signal E5b. The open signal G5OCM is modulated onto the G5 (1176.45 MHz), similar to the GPS safety of life signal L5C and Galileo/BDS signal E5a (InsideGNSS, 2010).

The ground control stations of the GLONASS are maintained only on the territory of the former Soviet Union due to the historical reasons. This lack of global coverage is not optimal for the monitoring of a global navigation satellite system (Xu, 2007, p. 4).

1.2.3.3 The Development Status of BDS

The BeiDou navigation Satellite system (BDS) is a Chinese global navigation satellite system. BeiDou means the constellation of the Big Dipper (or Great Bear) in Chinese. Following the deployment and operation of the BeiDou Satellite Navigation Experimental System (BeiDou-1), China is in the progress of deploying BDS (formerly known as COMPASS and BeiDou-2). The build-up of BDS is divided into two steps. The first step is establishing regional navigation and positioning services, consisting of 5 satellites in Geostationary Orbit (GEO), 5 in Inclined Geosynchronous Orbit (IGSO), and 4 in Medium altitude Earth Orbit (MEO). This step has been completed by the end of October 2012. The second step will complete the constellation, which comprises 5 GEO, 3 IGSO, 27 MEO satellites by the end of 2020. Then, the BDS system will provide global navigation services similar to GPS, GLONASS and Galileo (Zhao et al., 2013; Shi et al., 2013; Montenbruck et al., 2013; BDS, 2014).

In April 2014, the BDS constellation consisted of 14 satellites, divided into three types, 5 GEO, 5 IGSO, and 4 MEO. The GEO satellites are operating in orbits with an altitude of 35786 km and are positioned at 58.75°E, 80°E, 110.5°E, 140°E and 160°E, respectively. The IGSO satellites are operating in orbits with an altitude of 35786 km and an inclination of 55° w.r.t. to the equatorial plane. The phase difference of the right ascensions of the ascending nodes of the orbital planes is 120°. The MEO satellites are operating in orbits with an altitude of 21528 km and an inclination of 55° to the equatorial plane. The satellite recursion period is 13 rotations within 7 days. The respective positions of satellites are shown in Figure 1.4 (BDS-ICD, 2013; BDS-OS-PS, 2013).

The positioning services transmit signals using B1, B2 and B3. The nominal frequency is 1561.098 MHz, 1207.140 MHz and 1268.520 MHz for B1, B2, B3, respectively (BDS-ICD, 2013).

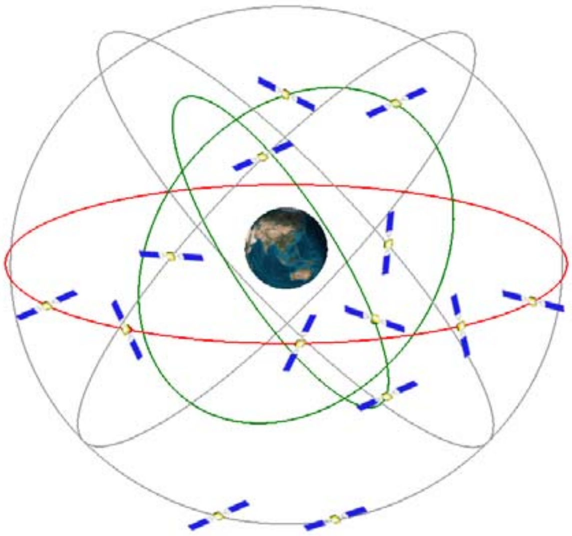

Figure 1.4: BDS space constellation (BDS-OS-PS, 2013)

1.2.3.4 The Development Status of Galileo

The Galileo satellite navigation system is the first civilian GNSS. It has been created by the European Union (EU) and the European Space Agency (ESA) to provide a highly accurate navigation and positioning service designed specifically for civilian purposes and run solely by civilians.

The fully functional Galileo constellation will consist of 27 satellites and 3 spares, positioned in three orbital planes with nine equally spaced operational satellites in each plane plus one inactive spare satellite. The ascending nodes of the orbital planes are equally spaced by 120 degrees. The orbital planes are inclined at 56 degrees. Each Galileo satellite is in a nearly circular orbit with a semi-major axis of 29600 km (Xu, 2007, p. 4; Galileo-ICD, 2010).

The first Galileo test satellite was launched in December 2005. The first four satellites were launched into orbit in 2011 and 2012. Four satellites is the minimum number needed to obtain a unique solution. The full completion of the 30-satellite Galileo system is expected by 2019 (ESA, 2014).

The Galileo navigation signals are transmitted in four frequency bands, E5a (1176.450 MHz), E5b (1207.140 MHz), E6 (1278.570 MHz) and E1 (1575.420 MHz). They provide a wide bandwidth for the transmission of the Galileo Signals (Galileo-ICD, 2010; ESA, 2014).

Mission and services of Galileo are Open Service (OS), Safety-of-Life Service (SoL), Commercial Service (CS), Public Regulated Service (PRS) and Search and Rescue Service (SAR) (ESA, 2014).

It should be noted, however, that the GNSS data used for this thesis is based on the current performance of GNSS.

1.3 Related Research of GNSS Data Processing

With regards to the emergence and development of GNSS, theories and methods of GNSS data processing have been developed. Scientists and technologists made outstanding contributions which improve the accuracy of GNSS precise positioning results. Differential (or relative) and undifferential (or absolute) positioning are the main data processing methods in GNSS precise positioning. They have specific advantages and disadvantages, differences and common characteristics.

Double Differencing (DD) is a classical and early GNSS data processing method, which can reduce common errors (such as receiver clock error, satellite clock error, satellite orbits error, tropospheric delay, ionospheric effects and so on) by differential observations in a small region. The DD method can provide a positioning service with an accuracy of centimetre or even millimetre, which depends on the baseline length. This method has been widely used because it does not consider the complex model of error correction. In contrast, it has less unknown parameters, higher accuracy of positioning results and it keeps the integer characteristics of the DD integer ambiguities (Blewitt, 1989; Dong and Bock, 1989; Wei and Ge, 1998; Chen, 1998; Hofmann-Wellenhof et al., 2008, p. 175; Wang et al., 2010; Shi et al., 2013). Real Time Kinematic (RTK) positioning, Network-based Real Time Kinematic (NRTK) positioning and Continuously Operating Reference Stations (CORS) can provide real-time kinematic positioning servers with an accuracy of centimetre or millimetre, based on one or more reference stations or a reference network (Bock and Shimada, 1990; Wübbena et al., 1996; Han, 1997; Chen et al., 2000; Chen et al., 2001; Grejner-Brzezinska et al., 2007; Snay and Soler, 2008).

In applications for short distances (about 10 km), a common practice is to neglect the common error effects. However, in the case of longer distances (hundreds or even thousands of km), differential common error residuals increase and may hamper the differential process, or may decrease the accuracy (Genrich and Bock, 1992; Wielgosz et al., 2005; Li et al., 2010; Li et al., 2013; Chu and Yang, 2013; Stephenson et al., 2011). Therefore, the reduction of differential error effects is one of the most important steps to improve the relative kinematic positioning. Hence, the medium and long-range precise kinematic positioning is studied here in this thesis.

In the most recent decades, an innovative Precise Point Positioning (PPP) technology based on undifferenced data processing strategies has been extensively studied. Based on the precise satellite clock and orbit products of the International GNSS Service (IGS), the standard PPP can provide positioning accuracy of decimetre to a few centimetre levels in post-processing mode in a global reference frame (Zumberge et al., 1997; Kouba and Héroux, 2001; Dixon, 2006; Geng et al., 2010; Zhang et al., 2011b). Following RTK and NRTK technological revolution, PPP is an innovative and flexible technology, without requiring users to set up their own ground reference stations, providing unlimited operating distance at low cost. It can be widely used in LEO satellite precise orbit determination, GNSS meteorology, investigation of ionospheric effects, precise timing, GNSS seismology, earth plate movement and dynamics research, engineering applications areas and many other earth science disciplines, with important application value (Chen et al., 2004; Zhang and Andersen, 2006; Bisnath and Gao, 2008).

In order to improve the accuracy of the standard PPP technology, the PPP Regional Augmentation (PPP-RA) technology (very similar to the PPP-RTK technology) has been developed to generate undifferential corrections in the observation domain from a regional reference network which can be disseminated by reference stations and applied to user observations for an instantaneous ambiguity-fixing. In such a service, instantaneous ambiguity resolution is accessible for regions with these observation corrections as regional augmentation information. At the user’s side, the data processing is similar to standard PPP and the difference is whether the corrections based on the regional network are applied or not. PPP-RA can provide services of positioning with a few centimetres accuracy after a convergence time of about 30 minutes or after successful ambiguity fixing, and instantaneous positioning at a few centimetres level in the regions where augmentation information is available (Collins et al., 2008; Mervart et al., 2008; Teunissen et al., 2010; Zhang et al., 2011a; Geng et al., 2011; Ge et al., 2012; Li et al., 2014).

In summary, to reach a higher precision in GNSS precise positioning for large-scale areas or long baselines more information is needed, which comes from multiple reference stations or a regional reference network. In this situation, undifferential and differential GNSS data processing are essentially different implementations for the usage of the network data and are integrated into a unified service (Li et al., 2013). In 2002 it was algebraically demonstrated for the first time that the undifferential and differential algorithms of GNSS are equivalent (Xu, 2002; Xu, 2007, pp. 111, 112; Xu et al., 2010). However, this depends on the way how the satellite and receiver clocks are analysed. In undifferenced algorithm, the clocks can be estimated, e.g. precise times corrections. Furthermore, most of these previous studies used the results of

DD processing taken as “true value”, to evaluate their results of the proposed approach. Therefore, the method of DD processing is deeply studied in this research.

1.4 Challenges and Research Objectives

In the GEOHALO airborne gravimetric project, the new German scientific aircraft HALO was used. Its characteristics are ultra-high-altitude, ultra-long-range, and high dynamics. The role of GNSS precise positioning in airborne gravimtery and development of GNSS technology imposed the following challenges and research objectives.

GNSS precise positioning is required to provide high-precision state information of the kinematic platform in airborne gravimetry. Since here not only the position but also velocity information for the platform are needed, the existing estimation method needs to be improved. Furthermore, since the GNSS data from airborne gravimetric projects are of high frequency, high dynamic, long range, and contain large amounts of data, the traditional estimation method is not efficient. Therefore, a GNSS estimation method of high-precision and efficiency needs to be developed. In this thesis, in order to obtain high-precision results for GNSS kinematic precise positioning, the estimation methods of least squares including the elimination of nuisance parameters and a two-way Kalman filter are applied. Furthermore, accuracy evaluation and reliability analysis of GNSS kinematic precise positioning is studied in-depth.

From the background of GNSS data processing, we know that both undifferential (PPP-RTK and PPP-RA) and differential data processing are essentially different implementations (utilizations) for the data of reference stations or a reference network. In order to obtain the high-precision results of GNSS precise positioning, the information of far away reference stations or a large scale reference network should be considered. Since the differential method shows high-precision results for GNSS precise positioning, by using only the existing IGS tracking stations or establishment of several temporary reference stations in the survey area, differential methods are thus widely used in airborne gravimetry. However, the survey area of possible future airborne gravimetric projects might stretch over thousands of kilometres (like closing the Antarctic polar gap in satellite-only gravity field models), so that the traditional single baseline model is facing new challenges. If the length of a single baseline for the relative positioning mode is too long, the tropospheric and other effects cannot be completely eliminated by the methods of model correction by applying DD between the kinematic and the reference station. In addition, the amount of visible common satellites will be reduced with the increasing length of the single baseline. Therefore, in order to solve this problem, a new method of GNSS precise positioning based on multiple reference stations is developed.

In airborne gravimetry, multiple antennas of GNSS receivers are usually mounted on the kinematic platform. The geometric relations between the multiple GNSS antennas and the similar characteristic of atmospheric effects within a small area above the kinematic platform should be taken into account for the improvement of the accuracy and reliability in the positioning. In this thesis, a GNSS kinematic positioning method based on multiple kinematic stations is proposed. Also, using the constant distance among multiple GNSS antennas, a kinematic positioning method based on a priori distance constraints is proposed to improve the reliability of the system. Furthermore, due to the similar characteristic of atmospheric effects in a small area above the kinematic platform, a common tropospheric wet delay parameter for the multiple GNSS antennas mounted on the platform is applied.

The trend of the development of GNSS is based on multiple systems and interoperability, with an increased amount of visible satellites. This makes studying multiple GNSS systems very essential. In addition, the reliability of a single GNSS system is lower. When there are not enough observations or no observations, the kinematic positioning results are of a poor accuracy or fail. Therefore, a method of kinematic positioning using GNSS integration is employed to improve the system reliability and accuracy. For this purpose, a GNSS integration algorithm based on Helmert's variance components estimation is proposed to reasonably adjust the weights and the contributions of different GNSS systems.

The velocity information for the kinematic platform is an important state parameter in airborne gravimetry. By the methods of position differencing and carrier phase differencing, we can only get the average velocity between observation epochs. However, a high dynamic and high speed aircraft can be used in an airborne gravity project such as GEOHALO. The average velocity (computed by position or carrier phase differencing) cannot meet the requirements of airborne gravimetry in such a case. Therefore, the instantaneous velocity of the kinematic platform determined by GNSS is much more important in airborne gravimetry on the HALO aircraft. Thus, raw Doppler observations are used to determine the kinematic instantaneous velocity in high dynamic environments. Furthermore, the carrier phase derived Doppler observations are used to obtain precise velocity results in low dynamic environments. Then, a new method of Doppler velocity determination based on GNSS integration with Helmert's variance components estimation and robust estimation is developed to obtain more precise velocity information.

Finally, based on the algorithm proposed in this thesis, combined with the actual requirements of airborne gravimetry and shipborne gravimetry, a high-precision kinematic GNSS position and velocity determination software (HALO_GNSS) has been developed for airborne gravimetry.

1.5 Contributions of this Research

The main outcomes of the research done in this thesis are:

- The parameter estimation algorithms of least squares adjustment including the elimination of nuisance parameter as well as the two-way Kalman filter were applied in kinematic GNSS data post-processing to fulfill the high accuracy requirements of airborne gravimetry.
- The specific accuracy evaluation methods for GNSS kinematic precise position determination have been developed and applied. In this context, the receiver clock errors including clock jumps were analyzed for high dynamics GNSS precise positioning.
- A new approach for the kinematic positioning using multiple reference stations based on an a priori constraint is addressed to increase the accuracy and reliability of the GNSS precise kinematic positioning in a large region. In this context, a robust estimation theory is used to suppress the impact of observation outliers on the trajectory estimates for airborne gravimetry.
- A new method of GNSS kinematic positioning based on multiple kinematic stations with an a priori distance constraint and a common tropospheric delay parameter is developed, which can enhance the accuracy and reliability of the state estimates as well.
- A kinematic positioning method using multiple GNSS systems integration based on Helmert's variance component estimation is addressed to improve the reliability and accuracy of GNSS kinematic positioning, and to adjust the weights in a reasonable way whilst to enhance the contributions among multiple GNSS systems.
- Velocity estimates were determined by the use of Doppler observations which were obtained either from the receiver-generated raw Doppler or from carrier phase derived Doppler data. A new approach for velocity determination based on the GNSS integration with Helmert's variance component estimation and the robust estimation has been developed.
- A reliable and precise kinematic GNSS position and velocity determination software system (HALO_GNSS) has been developed based on the algorithms proposed in this thesis. This software can be applied in many fields and allows the GNSS kinematic positioning with an accuracy of 1-2 cm and GNSS velocity determination with an accuracy of about 1 cm/s using raw and about 1 mm/s using carrier phase derived Doppler observations.

1.6 Overview of Dissertation

This thesis documents the approach in the development of algorithms, software, and analysis methods for precise GNSS kinematic position and velocity determination for airborne gravimetry. It includes nine chapters and has the following outline.

Firstly, Chapter 1 presents the introduction, motivation, background, challenges and research objectives of this thesis and specifies the contributions of this research.

Chapter 2 introduces the fundamentals of GNSS data processing and explains several different combinations of GNSS observations as used in this thesis for different purposes. The main error sources of GNSS observations are given in this chapter as well.

Chapter 3 addresses the nuisance parameter elimination in the least squares adjustment as well as the two-way Kalman filter for kinematic positioning. The methods of accuracy evaluation for static and kinematic positioning results are described. The influence of receiver clock errors in kinematic positioning is analyzed as well.

Chapter 4 explains the development of a method for multiple reference stations relative positioning based on a priori constraints. The application of robust estimation in the algorithm is addressed as well.

Chapter 5 shows the improvements of the method of kinematic positioning based on multiple kinematic stations as well as of the method based on a priori distance constraints among multiple kinematic stations. The algorithm of using a common tropospheric parameter among multiple kinematic stations is addressed too.

Chapter 6 highlights the precise positioning based on the integration of different GNSS systems as well as the Helmert's variance component estimation used in this algorithm.

Chapter 7 gives the details of the velocity determination from the GNSS Doppler observations. The used Doppler data were from receiver-generated raw Doppler observations as well as the carrier phase derived Doppler data. Furthermore, the Doppler velocity determination based on GNSS integration and robust estimation is addressed.

Chapter 8 describes the characteristics and structure of the HALO_GNSS software based on the algorithm of this thesis. The application of the kinematic GNSS algorithms and software in the kinematic data analysis in an airborne gravimetric project and in shipborne gravimetry is demonstrated.

Finally, Chapter 9 summarizes the main results as obtained in the previous chapters, presents the final conclusions and suggests recommendations for future work.

2 GNSS Observations and Error Sources

2.1 Introduction

The basic GNSS observables are the code pseudoranges and carrier phases as well as Doppler measurements. The principle of the GNSS measurements and their mathematical expressions are described below. In particular, several different linear combinations of GNSS observations are used in this thesis for different purposes.

The key point for the GNSS precise positioning is an ability to mitigate all potential error sources and disturbances in the system. All errors in GNSS observations caused by the space segment, by the signal propagation, by the environment around the receiver, and by the hardware of the receiver itself need to be mitigated. The mitigation can be carried out by modelling, estimating, and forming single station observation combinations as well as by using differential techniques. These observation errors will be discussed in detail in this chapter.

2.2 GNSS Observations

The fundamental measurements recorded by a GNSS receiver are the differences in time or phase between the signals transmitted by the GNSS satellites and reference signals generated inside the receiver. The GNSS signals are transmitted at different frequencies (Chen, 1998). GNSS receivers generate various observables from the GNSS signals. The observation types of code pseudorange, carrier phase and Doppler are discussed in this section.

2.2.1 Pseudorange

Unlike the terrestrial electronic distance measurements, GNSS satellite navigation and positioning uses the “one-way concept” where satellite and receiver clocks are involved. Thus the ranges are biased by satellite and receiver clock errors. Consequently, they are denoted as pseudoranges (Hofmann-Wellenhof et al., 2008, p. 105). The GPS receiver generates a copy of the pseudorandom code and compares it to that arriving from the satellite. A time offset is computed by an autocorrelation function between the received pseudorandom code from the satellite and that generated by the receiver. This offset contains the signal travel time and the mis-synchronization of the satellite and receiver clocks. The pseudorange measurements typically have a precision on the order of 1-10 meters. The equation for the pseudorange observable is given in (Xu, 2002; Seeber, 2003, p. 255; Deng, 2012)

$$P_{r,j}^{s} = \rho_r^s + c(dt_r - dt^s) + I_{r,j}^{s} + T_r^s + b_{r,j} - b_j^s + \varepsilon_{r,j}^{s}, \tag{2.1}$$

where the superscript s refers to a given satellite, subscript r refers to the receiver, subscript j identifies the frequency of the frequency-dependent terms, $P_{r,j}^{s}$ is the pseudorange between the receiver r and the satellite s at the frequency j, ρ_r^s is the geometic distance from the receiver r to the satellite s, including relativistic corrections as well as phase centre offset and variations. c denotes the speed of light in vacuum, dt_r and dt^s are the offsets of the receiver and satellite clock with respect to system time, $I_{r,j}^{s}$ is the ionosphere delay on the signal path at frequency j, T_r^s is the troposphere delay on the signal path, $b_{r,j}$ and b_j^s are the code bias of receiver r and satellite s at frequency j, respectively, $\varepsilon_{r,j}^{s}$ represents the effect of observation noise and all non-modeled error sources, such as errors in the satellite clock and orbit prediction, inaccuracies in ionospheric and tropospheric modeling, multipath. Unit meter (m) is used for all terms. In this thesis, the pseudorange measurement is mainly used to obtain an approximate or initial position and to construct the ionosphere-free, geometry-free measurements.

2.2.2 Carrier Phase

Carrier phase observations are obtained by comparing the phases between a signal transmitted by a satellite and a similar signal generated by a receiver. The receiver records the fractional phase of the GNSS satellite and keeps track of the changes of the received carrier phase. The initial phase, called ambiguity, is unknown. In order to use phase observations the so-called phase ambiguity must be resolved. The phase observations have a noise of a few millimetres and are much more accurate than pseudoranges. The equation of the carrier phase measurements can be written as (Chen, 1998; Leick, 2004, p. 256; Hofmann-Wellenhof et al., 2008, p. 106)

$$\lambda_j^s \cdot \varphi_{r,j}^{s} = \rho_r^s + c \cdot (dt_r - dt^s) - I_{r,j}^{s} + T_r^s + \lambda_j^s \cdot N_{r,j}^{s} + d_{r,j} - d_j^s + e_{r,j}^{s}, \tag{2.2}$$

where λ_j^s is the carrier wavelength of satellite s at frequency j, $\varphi_{r,j}^{s}$ is the carrier phase observation in cycles between the receiver r and the satellite s at the frequency j, ρ_r^s is again the geometric distance from the receiver r to the satellite s including relativistic corrections as well as phase centre offset and variations, $I_{r,j}^{s}$ is the ionosphere delay for carrier phase observation on the path at frequency j scaled to units of length, it has the same magnitude as for pseudorange measurements, but is of the opposite sign, $N_{r,j}^{s}$ is the integer ambiguity for a particular receiver-satellite pair at frequency j, $d_{r,j}$ and d_j^s are the carrier phase biases of receiver r and satellite s at frequency j, respectively, $e_{r,j}^s$ represents unmodeled effects, modeling errors and measurement errors for carrier phase observations, it is three or four orders of magnitude lower than that of code measurements.

2.2.3 Doppler

The Doppler effect is a phenomenon of frequency shift of the electromagnetic signal caused by the relative motion of the emitter w.r.t. the receiver. In a first approximation, the Doppler shift is given as (Hofmann-Wellenhof et al., 2008, p. 108; Xu, 2007, p. 41)

$$D_{r,j}^s = f_j^s - f_{r,j}^s = \frac{V_{\rho_r^s}}{c} f_j^s = \frac{V_{\rho_r^s}}{\lambda_j^s}, \tag{2.3}$$

where $D_{r,j}^s$ is the Doppler shift between satellite s and receiver r at frequency j, f_j^s denotes the emitted frequency j of satellite s, $f_{r,j}^s$ the received frequency j from satellite s, $V_{\rho_r^s}$ is the relative velocity along the distance line between satellite s and receiver r, λ_j^s is carrier wavelength of satellite s at frequency j. The Eq. (2.3) for the observed Doppler shift scaled to range rate is given by

$$V_{\rho_r^s} = \lambda_j^s \cdot D_{r,j}^s = \dot{\rho}_r^s + c \cdot (d\dot{t}_r - d\dot{t}^s) + \varepsilon, \tag{2.4}$$

where the derivatives with respect to time are indicated by a dot, ε is the measurement error.

The Doppler frequency shift is a by-product of the carrier phase measurements, an independent observable and a measure of the instantaneous range rate. When a satellite is moving toward the GNSS receiver, the Doppler shift is positive; so one gets more Doppler counts when the range is diminishing.

In this thesis, the GNSS Doppler observations are used to estimate the velocity of the kinematic platform and will be discussed in detail in Chapter 7.

2.3 Linear Combinations of GNSS Observations

Several linear combinations of the original GNSS carrier phase and code measurements are used during data analyses to eliminate or reduce certain components of the observation equation. For instance, a linear combination can be formed to remove the effect of the ionosphere. These combinations are listed below, followed by a brief description. φ_j represents the phase observations in cycles at frequency j, P_j denotes the code observations in meters at frequency j.

2.3.1 Ionosphere-free Linear Combination (LC)

The ionosphere delay caused by the refraction of the electromagnetic GNSS signal when propagating through the ionospheric layer in the atmosphere ranges from 6 to 150 m. The normal approach to eliminate the ionospheric delay is forming a dedicated linear combination of GNSS observations. This combination is called the “ionosphere-free measurement LC”. For the carrier phase observation Eq. (2.2) and the code observation Eq. (2.1), the ionosphere-free combination can be written as (cf. Hofmann-Wellenhof et al., 2008, p. 127; Xu, 2007, p. 97)

$$\varphi_{LC} = \frac{f_1^2}{f_1^2 - f_2^2}\varphi_1 - \frac{f_1 \cdot f_2}{f_1^2 - f_2^2}\varphi_2 \tag{2.5}$$

and

$$P_{LC} = \frac{f_1^2}{f_1^2 - f_2^2}P_1 - \frac{f_2^2}{f_1^2 - f_2^2}P_2 . \tag{2.6}$$

The ionospheric delay is frequency-dependent. Eq. (2.5) and Eq. (2.6) eliminate the effect of the first-order ionospheric delay on the observables which is widely used in GNSS data processing. The disadvantage of this linear combination is that the noise from the φ_1 and φ_2 carrier phase measurements is increased almost by a factor of three (Seeber, 2003, p. 263), and that the ambiguities cannot directly be solved as integer numbers.

For receivers that have dual-frequency capability the LC combination is usually the preferred method in geodetic and atmospheric applications for the estimation of coordinates, tropospheric delay values and receiver clock biases.

2.3.2 Widelane Combination (WL)

The widelane observation is a popular linear combination mainly used for ambiguity and cycle slip fixing which can be described as

$$\varphi_{WL} = \varphi_1 - \varphi_2 . \tag{2.7}$$

The combined wavelength λ_{WL} of the L1 and L2 carrier phase measurements amounts to 86 cm. This long wavelength simplifies the ambiguity solution. It is commonly used in the analysis for GNSS stations which are distant from each other by more than a few tens of km. In the data pre-processing it can also be applied for detecting cycle slips (Blewitt, 1990).

2.3.3 Extra-widelane Linear Combination (EX_WL)

Since φ_1 and φ_2 carry the same geometric information, a position-independent quantity can be constructed by subtracting the φ_2 carrier phase observation multiplied by the frequency ratio from the φ_1 carrier phase observation as given by

$$\varphi_{EX\_WL} = \varphi_1 - \frac{f_1}{f_2}\varphi_2 . \tag{2.8}$$

This extra-widelane linear combination eliminates the geometric (orbits, station coordinates), tropospheric, and clock synchronization components of the carrier phase equation. Thus it is often called geometry-free linear combination or extra-widelane. Since the combination of the initial phase ambiguities remains, EX_WL can only represent the complete variation of the ionospheric delay during a continuous tracking (Chen, 1998).

For the GPS data pre-processing it is possible to construct a polynomial fit for EX_WL, and to identify discontinuities such as cycle slips or outliers. But under high ionospheric activity conditions it is difficult to detect cycle slips with the ionosphere linear combination (Blewitt, 1990).

2.3.4 MW Widelane Linear Combination (MW_WL)

The widelane observation in Eq. (2.7) still contains the position information. But the ionospheric effects and position information from the widelane observation can be eliminated, due to the fact that the ionosphere effects on the code and phase measurements are equal but have opposite signs in Eq. (2.1) and Eq. (2.2). When both, code and phase information are all available on two frequencies, the position-free and ionosphere-free observation can be given as (Chen, 1998)

$$\varphi_{MW\_WL} = \varphi_1 - \varphi_2 - \frac{f_1 - f_2}{f_1 + f_2}\left(\frac{P_1}{\lambda_1} + \frac{P_2}{\lambda_2}\right). \tag{2.9}$$

This quantity is called the Melbourne-Wübbena combination (Melbourne, 1985; Wübbena, 1985). It combines the phase and code observations to eliminate the ionospheric, geometric and clock effects and will be used for ambiguity initialization in GNSS data processing. Only the error of multipath and the pseudorange noise are still contained in MW_WL, but they can be reduced or eliminated by averaging multiple epoch (Blewitt et al., 1988).

2.4 Error Sources

The prerequisite of an accurate GNSS precise positioning is to reduce the errors resp. disturbances contained in GNSS measurements, which include ionospheric effects, tropospheric effects, relativistic effects, Earth tide and ocean loading tide effects, clock errors, antennas phase centre corrections, multipath effects, antenna phase wind up as well as hardware biases. The main errors will be discussed in this section. Further information can be found in Seeber (2003), Leick (2004), Xu (2007) and Hofmann-Wellenhof et al. (2008).

2.4.1 Satellite Orbit and Clock Errors

The impact of satellite orbit and clock errors depends on the type of the applied GNSS processing technique. Based on a simple rule of thumb (Beser and Parkinson, 1982; Seeber, 2003, p. 302) the impact of the satellite orbit error on single point positioning can be given as

$$dp = \mathrm{PDOP} \cdot dr \,, \tag{2.10}$$

where dp is the point positioning error, PDOP is the Positional Dilution Of Precision (Langley, 1999) and dr is the error of the satellite orbit in meter. For $\mathrm{PDOP} = 2$, a 2 m position error will be caused by a 1 m orbit error.

For differential positioning, the impact of orbit errors on the solutions will grow larger with the increase of the distance between the reference station and the kinematic GNSS stations (Abdel-salam, 2005). It has been demonstrated that the relative accuracy of a baseline obtained from DD GNSS observations can be related to the satellite position error by a rule of thumb

$$db = \frac{b}{r} dr \tag{2.11}$$

as given by Beser and Parkinson (1982), Parrot (1989), Dach et al. (2007) and Seeber (2003, p. 304), where db is the baseline error, b is the baseline length, dr is the orbit error, r denotes the distance between the receiver and satellite (about 23000 km), According to this relation, to achieve a baseline error below 1 cm, the admissible orbit errors as given in Table 2.1 are required for specified baseline lengths.

Table 2.1 clearly shows that, for differential positioning over short distances, the required orbit accuracy is not a critical factor. However, the requirement for 1 cm accuracy over very large distances, for example, in geodynamic applications over 500 km and more, implies an orbit accuracy of better than 1 m. Nevertheless, the impact of satellite orbit errors on positioning is much larger for single point positioning than for differential positioning.

Table 2.1: The relation between admissible orbit error and baseline length for an 1 cm baseline error for differential GNSS positioning

Baseline length	**Required admissible orbit error**
10 km	23 m
50 km	4.6 m
100 km	2.3 m
500 km	0.46 m
1000 km	0.23 m
1500 km	0.15 m
2000 km	0.11 m

In contrast to the orbit error, there is no baseline-dependent component for the satellite clock correction (Parkinson, 1996). By using global GNSS tracking networks (shown as Figure 3.1) GNSS satellite orbit and clock parameter can be estimated with high accuracy. The International GNSS Service (IGS), formerly the International GPS Service, provides orbits and clocks in different latencies and accuracies as shown in Table 2.2.

Table 2.2: IGS combined orbit and clock products (IGS, 2013)

GNSS Products Type			**Accuracy**	**Latency**	**Updates**	**Interval**
GPS	Broadcast	orbits	~100 cm	real time	--	daily
		Sat. clocks	~5 ns RMS ~2.5 ns SDev			
	Ultra-Rapid (predicted half)	orbits	~5 cm	real time	at 03, 09, 15, 21 UTC	15 min
		Sat. clocks	~3 ns RMS ~1.5 ns SDev			
	Ultra-Rapid (observed half)	orbits	~3 cm	3 - 9 hours	at 03, 09, 15, 21 UTC	15 min
		Sat. clocks	~150 ps RMS ~50 ps SDev			
	Rapid	orbits	~2.5 cm	17 - 41 hours	at 17 UTC daily	15 min
		Sat. & Stn. clocks	~75 ps RMS ~25 ps SDev			5 min
	Final	orbits	~2.5 cm	12 - 18 days	every Thursday	15 min
		Sat. & Stn. clocks	~75 ps RMS ~20 ps SDev			Sat.: 30 s Stn.: 5 min
GLONASS	Final		~3 cm	12 - 18 days	every Thursday	15 min

The IGS has presently 12 Analysis Centres (ACs). The IGS ACs use the collected data from more than 360 stations worldwide to generate and provide precise GNSS ephemerides and adjusted clock parameters. GFZ operates one of the IGS Analysis Centres since the very beginning of the IGS activities (Deng, 2012). Compared to the Broadcast ephemeris, the GNSS orbit and clock uncertainties can be significantly reduced by using the IGS ultra-rapid (IGU), rapid (IGR) and final products.

2.4.2 Antenna Phase Centre Offset and Variation

The GNSS observation refers to the distance between the satellite and receiver antenna phase centres, which varies with the frequency and the receiver-satellite orientation (Mader, 1999). The need for satellite-related corrections is caused by the difference between the GNSS satellite centre of mass and the phase centre of its antenna. Since the force models used for satellite orbit modelling refer to the satellite centre of mass, the IGS GNSS precise satellite coordinates and clock products also refer to the satellite centre of mass. In contrast the orbit ephemerides in the GNSS broadcast navigation message refer to the satellite antenna phase centre. However, all GNSS measurements are made to the antenna phase centre, thus one must know the satellite phase centre offsets and has to monitor the orientation of the offset vector in space as the satellite orbits the earth (Kouba, 2009a). Ignoring these phase centre variations can lead to serious (up to 10 cm) vertical errors (Mader, 1999). Due to the differentiation between the satellite's centre of mass and the antenna phase centre position, the corrections for satellite antenna Phase Centre Offsets (PCO) and Phase Centre Variations (PCV) must be considered in GNSS data analysis for highly precise applications in particular for long baselines.

Analogously to the satellite, the phase centre of the GNSS receiver antenna is different from its Antenna Reference Point (ARP) and should be taken into account (Rothacher, 2001). The mean position of the electrical phase centre is determined for each frequency and the location with respect to the ARP in a local reference system is denoted as PCO. However, the actual electrical phase centre may depend on satellite-receiver direction. The deviation from the mean phase centre is known as PCV (Moreno Monge, 2012).

Besides individual corrections for a specific antenna, there are also type-specific antenna corrections (Schmid et al., 2007). These are mean values from calibrations of several antennas of the same antenna type, which can then be used for all antennas of this type. The IGS calibrations of the GNSS satellite and station antennas can be downloaded from the IGS ftp site (ftp://igscb.jpl.nasa.gov/pub/station/general/).

2.4.3 Satellite and Receiver Hardware Biases

The satellite as well as the receiver hardware systems cause time delays in the measured ranges, which differ from each other for every frequency and every modulating code. The manufacturers spend a lot of work to avoid or at least to calibrate these biases. Yet, these biases cannot be calibrated completely, since they depend on several influences (Roßbach, 2001). Thus, they must be carefully estimated in precise GNSS applications. These biases are known as hardware or electronic biases, including satellite code biases b_j^s and receiver code biases $b_{r,j}$ in Eq. (2.1), satellite phase biases d_j^s and receiver phase biases $d_{r,j}$ in Eq. (2.2) (Banville et al., 2008).

These biases impose a different clock datum on each observable, so that the true clock errors dt_r and dt^s cannot really be recovered (Collins et al., 2005). And it must be taken into account that IGS precise satellite clock corrections are estimated from the ionosphere-free combination of phase and code observations in P1 and P2, therefore they contain the ionosphere-free linear combination of the satellite hardware biases (Dach et al., 2007).

The receiver hardware delays are different for GPS and GLONASS observations. Whereas for carrier phase observations the hardware delays are absorbed by the initial ambiguities, such errors can reach several ns for the code observations. Nevertheless, when DD are formed, satellite and receiver hardware biases can be cancelled out. But in point positioning it’s difficult to correct these errors caused by receiver code biases since they occur during the analysis of doubly differential data from more than one receiver type, where their effect is not cancelled out (Moreno Monge, 2012).

The hardware biases cannot be determined in an absolute sense, but they can be mostly eliminated from the code observations by using the Differential Code Biases (DCB) corrections, which are provided by the IGS (Collins et al., 2005; Banville et al., 2008). The DCB corrections can be downloaded from the ftp site of the Centre for Orbit Determination in Europe (CODE) (ftp://ftp.unibe.ch/aiub/CODE/).

2.4.4 Tropospheric Effects

The troposphere is the lowest part of the atmosphere over the Earth’s surface. In contrast to the ionosphere, the troposphere is a non-dispersive medium for the GPS carrier frequencies. In other words, the tropospheric effects on the GPS signal transmission are independent from the working frequency and the electromagnetic signals are affected by the neutral atoms and molecules in the troposphere. The effects are called tropospheric delay or tropospheric refraction. (Xu, 2007, p. 55). The principle of the tropospheric delay is shown in Figure 2.1.

The troposphere causes a transmission delay of the GNSS signals both through signal path bending and the alteration of the wave propagation velocity. The amount of tropospheric delay in the zenith direction is about 2 m and it increases with the decrease of the elevation angle of the sight line from the receiver to the satellite. For satellite elevation angles lower than 10 degrees, the tropospheric delay of the GNSS signal can reach up to about 20 meters (Xu, 2007, p. 55; Wang et al., 2009b). Therefore, the tropospheric effect is an important error source in precise GNSS applications.

The tropospheric delay can be split into the hydrostatic (i.e. dry) and the wet component. The hydrostatic component is caused by the dry atmospheric gases and induces about 90% of the total tropospheric delay. The hydrostatic component can be easily modelled (Schüler, 2001; Abdel-salam, 2005). The wet component is mainly caused by the water vapour in the lower part of the troposphere up to 11 km above sea level. The wet component causes 10% of the total tropospheric delay (Abdel-salam, 2005; Hofmann-Wellenhof et al., 2008, p. 129). Due to the variation of the water vapour density with position and time, modelling of the wet component is difficult.

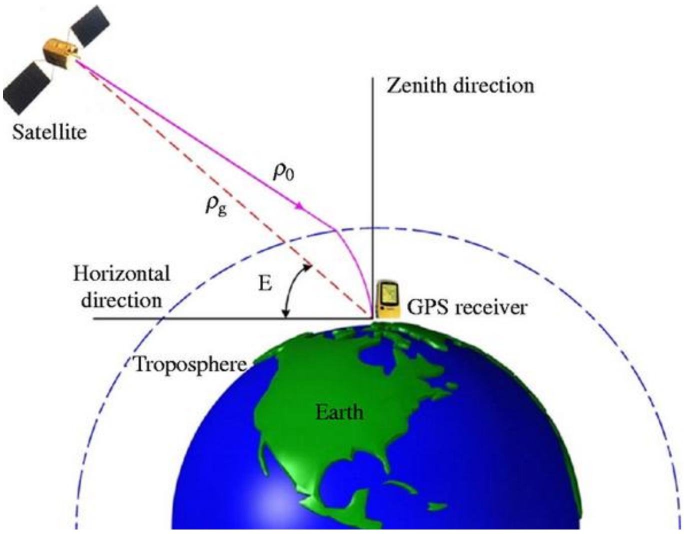

Figure 2.1: The principle of troposphere delay (Wang et al., 2009b)

The excess path length is the troposphere delay and is called Slant Total Delay (STD). The hydrostatic and wet tropospheric delay are usually modelled as delays in zenith direction and then mapped down to the satellite elevation using a mapping function. The STD between satellite and receiver at an elevation angle e can thus be written in the form given below (Davis et al., 1985; Collins and Langley, 1997)

$$\mathrm{STD} = M_h(e) \times \mathrm{ZHD} + M_w(e) \times \mathrm{ZWD}\,, \tag{2.12}$$

where STD is the slant total tropospheric delay between the satellite and receiver, ZHD and ZWD are the zenith hydrostatic delay and the zenith wet delay, respectively. $M_h(e)$ and $M_w(e)$ are the hydrostatic and the wet mapping function, respectively, which depend on the elevation angle e. The ZHD can be modelled with sub-millimetre accuracy using surface pressure measurements under the assumption that the atmosphere is in hydrostatic equilibrium (Janes et al., 1991). The ZHD can be retrieved with an accuracy of 1-3 mm using global Sea Level Pressure (SLP) grids of atmospheric models as provided by the European Centre for Medium-Range Weather Forecasts (ECMWF) together with an adequate model for the height dependence of the atmospheric pressure (Fernandes et al., 2013; Singh et al., 2014). However, ZWD cannot be modelled with an accuracy better than 2cm (Mendes and Langley, 1995; Singh et al., 2014).

Here in the studies for this thesis different tropospheric correction models and mapping functions based on theoretical approaches as well as on measured atmospheric data are used. For the tropospheric path delay in zenith direction the models of Saastamoinen (Saastamoinen, 1972), Hopfield (Hopfield, 1969), Black-Eisner (Black and Eisner, 1984), Ifadis (Ifadis, 1986) and Askne and Mordius (Askne and Nordius, 1987) are applied while the applied mapping functions comprise Davis, Chao, Marini (Mendes and Langley, 1994), Niell mapping function (Niell, 1996), Isobaric mapping function (Niell, 2001), the Vienna mapping function (Boehm and Schuh, 2004) and a Global Mapping Function (GMF) (Bohm et al., 2006) etc.

Basically, three methods are used here for modelling the tropospheric delay. The first method uses DD processing to eliminate the tropospheric error, but this works only for relative positioning on short baselines. The second method uses a tropospheric delay model to revise the error whereas the third method is an adjustment of troposphere parameters to estimate a residual atmospheric delay. The pros and cons are discussed in Section 5.4.

2.4.5 Ionospheric Effects

The ionosphere is the higher stratum of the atmosphere with an extension from about 50-2000 km. The ionospheric refraction causes a group delay and a phase advance in the propagation of the GNSS signals. The magnitude of the ionospheric delay or advance of the GNSS signal can vary from a few meters to more than hundred meters within one day which is larger than the delay caused by the troposphere (Xu, 2007, p. 48). The advance of the carrier phase and the delay in the code observation are of the same magnitude but have opposite signs. However the ionospheric refraction can be eliminated to a first order approximation by forming the mentioned ionospheric-free linear combination of dual-frequency (DF) GNSS observations. This first order ionosphere-free combination can be formed as Eq. (2.5) for the carrier phase observation and Eq. (2.6) for the pseudorange observation.

Single frequency GNSS users can reduce the ionospheric delay by applying a model, such as the Klobuchar model (Klobuchar, 1987) or the NeQuick model (Radicella and Leitinger, 2001), or use the values computed by the IGS Analysis Centre for either a global or a regional ionosphere, such as Global Ionospheric Map (GIM) models (Jee et al., 2010).

2.4.6 Site Displacement Effects

In a global sense, a station undergoes periodic movements (real or apparent) reaching a few dm that are not included in the International Terrestrial Reference Frame (ITRF) "regularized" positions, from which "high-frequency" displacements have been removed using models. Since most of the periodic station movements are nearly the same over broad areas of the Earth, they almost cancel each other in differential positioning over short (<100km) baselines and thus they do not need to be considered. However, if one is to obtain a precise station coordinate solution consistent with the current ITRF conventions in PPP, using undifferential approaches, or in relative positioning over long baselines (> 500 km), the above station movements must be modelled as per recommendation in the IERS Conventions (Kouba and Héroux, 2001; Kouba, 2009a).

2.4.6.1 Earth Tides

The Earth responds as an elastic body to external forces caused by the Sun and the Moon. They cause periodic deformations of the Earth's crust and lead to vertical and horizontal site displacement, which can be computed quite accurately from simple Earth models, while the ocean tides are strongly influenced by the coastal outlines and the shape of the near-coastal ocean floor. The magnitude of the Earth tides is dependent on station latitude, tide frequency, and sidereal time. The effect of the tidal variation is larger for the vertical component than for the horizontal direction and can reach up to 30 cm. The horizontal movement can reach 5 cm (Kouba and Héroux, 2001; Deng, 2012).

The site displacement effects of the Earth tide due to degree 2 of the tidal potential is (McCarthy, 1996; Kouba and Héroux, 2001; Petit and Luzum, 2010)

$$\Delta\bar{r} = \sum_{j=2}^{3} \frac{GM_J}{GM} \frac{r^4}{R_J^3} \left\{ \left[3l_2 \left(\widehat{R}_j \cdot \widehat{r} \right) \right] \widehat{R}_j + \left[3\left(\frac{h_2}{2} - l_2 \right) \left(\widehat{R}_j \cdot \widehat{r} \right)^2 - \frac{h_2}{2} \right] \widehat{r} \right\} + \\ \left\lfloor -0.025m \cdot \sin\phi \cdot \cos\phi \cdot \sin\left(\theta_g + \lambda \right) \right\rfloor \cdot \widehat{r} \quad , \qquad (2.13)$$

where $\Delta\overline{r}$ is the site displacement vector in Cartesian coordinates $\Delta\overline{r} = (\Delta x, \Delta y, \Delta z)^{\mathrm{T}}$. GM and GM_j are the gravitational parameters of the Earth, the Moon ($j = 2$) and the Sun ($j = 3$); r, R_j are the geocentric state vectors of the station, the Moon and the Sun with the corresponding unit vectors $\widehat{r}$ and $\widehat{R}_j$, respectively; l_2 and h_2 are the nominal second degree Love and Shida dimensionless numbers (about 0.608, 0.085); ϕ, λ are the site latitude and longitude and θ_g is Greenwich Mean Sidereal Time.

In the relative airborne kinematic GNSS positioning, the airborne antennas are of course not affected by the Earth tide effects. However, the static reference antennas mounted on the Earth surface are not free from tidal effects. In this case, the tidal displacements are usually independent from the size of the applied area or lengths of the baselines and have to be taken into account (Xu, 2007, p. 67).

2.4.6.2 Ocean Tide Loading

The ocean tide loading displacements affect mostly only the GNSS stations near the coast. The displacements at most of the continental stations are less than 1cm. Loading correction is not commonly considered in GNSS data processing because the computation is more complicated, and its modelling is less accurate. However, for precise applications, loading effects have to be taken into account (Xu, 2007, p. 72). When stations are located not too far away from the nearest coast line (<1000 km), the ocean loading effects should be taken into account for applications such as point positioning with centimetre to millimetre accuracy or GPS meteorology. Otherwise, this effect would be mapped into the ZTD and station clock correction (Kouba and Héroux, 2001; Kouba, 2009b).

The mode of ocean tide loading can be written as (McCarthy, 1996; Petit and Luzum, 2010)

$$\Delta o = \Sigma_j f_j A_{cj} \cos(\omega_j t + \chi_j + u_j - \phi_{cj}), \tag{2.14}$$

where Δo is the displacement due to ocean loading, j represents the 11 tidal waves (known as $M_2, S_2, N_2, K_2, K_1, O_1, P_1, Q_1, M_f, M_m, S_{sa}$), the f_j and u_j depend on the longitude of the lunar node (at 1-3 mm precision $f_j = 1$ and $u_j = 0$), ω_j and χ_j are the angular velocity and the astronomical arguments at time $t = 0$ h, corresponding to the tidal wave component j. A_{cj} is the station specific amplitude, ϕ_{cj} is the station specific phase.

2.4.7 Ambiguities and Cycle Slips

As described in Section 2.2.2, the carrier phase measurement is made by shifting the receiver-generated phase to track the received phase of the satellite signal. The absolute number of full carrier wave oscillations between the receiver and the satellite cannot be counted at the initial signal acquisition. Therefore, measuring the carrier phase means to measure a fractional phase and to keep track of changes in the cycles. Due to the measurement principle in the receiver, the carrier phase observable is an accumulated carrier phase observation (Xu, 2007, p. 39).

A full carrier wave oscillation is called a cycle. The ambiguous integer number of cycles in the carrier phase measurement is called ambiguity. It is necessary to correct the initially measured fractional phase. This is done by setting up an arbitrary integer number at the start epoch in the observations. Such an arbitrary initial setting will then be adjusted to the correct value by modelling the ambiguity parameters (Xu, 2007, p. 39). Without an exact determination of the integer ambiguities, no precise positioning at centimetre level based on GNSS phase observations can be achieved (Chen, 1998).

If the receiver loses the phase lock of the satellite signal, a cycle slip will occur. The reasons for cycle slips may be obstructions, signal noise, low satellite elevation, weak signals, antenna inclination in kinematic application (airplane, ship) and are caused by the signal processing (Seeber, 2003, p. 277). Cycle slips have either to be removed from the data at the pre-processing level, or a new ambiguity has to be determined (Seeber, 2003, p. 277).

The ambiguity estimation as well as the cycle slip detection and repair are not in the focus of this study. More details can be read e.g. in Seeber (2003), Leick (2004), Hofmann-Wellenhof et al. (2008) and Xu (2007).

2.5 Conclusions

In this chapter, the GNSS observations and their combination have been discussed. The main error sources and disturbances of the GNSS observations are described as well. That comprises the fundamental theories and conceptions for the GNSS signal modelling in this study.

In comparison to pseudoranges the carrier phases are much more precise with a precision of a few millimetres. For this reason the carrier phases are the most important observation type for precise GNSS applications like GNSS positioning. The pseudorange observations are only used to obtain an approximate or initial position and to construct the ionosphere-free, geometry-free measurements. The Doppler observations are used to estimate the velocity of the kinematic platform.

The GNSS data analysis algorithms rely on signal combinations and differential positioning. In general, disturbances of the GNSS observations like tropospheric impacts, satellite orbit and clock errors and receiver clock errors can be reduced or eliminated by differential positioning processing. For long baselines, some of the errors, especially the tropospheric signal delay has to be taken into account in precise kinematic positioning.

The following chapters deal with the treatment of these observables and the mathematical models to obtain a user position and velocity information from these measurements.

3 Algorithms Developing and Quality Analysis for GNSS Kinematic Positioning

3.1 Introduction

In this chapter, the mostly used adjustment and filtering algorithms for static and kinematic GNSS data processing are outlined. The adjustment algorithms as discussed here are the least squares adjustment and an equivalent algorithm which is based on what is known as eliminated observation equation system. The filtering algorithms discussed here concern the classic Kalman filter as well as the two-way Kalman filter.

The method used in this thesis for the evaluation of the precision and the reliability of GNSS kinematic precise positioning is discussed. The influence of the GNSS receiver clock error on the accuracy evaluation of the high-dynamics GNSS positioning is analyzed as well. Finally, an advice about the GNSS receiver clock error estimation is given.

3.2 Nuisance Parameter Elimination in Least Squares

In the least squares adjustment, the unknown parameters can be divided into two groups. In practice, sometimes only one group of unknowns is of interest. Therefore, it is often useful to “eliminate” the other group of unknowns (called nuisance parameters) because of its size, for example. In this case, using what is known as the equivalently eliminated observation equation system could be very beneficial. That means the nuisance parameters can be eliminated directly from the observation equations instead of from the normal equations (Zhou, 1985; Xu, 2002; Xu, 2007, p. 146; Shen and Xu, 2008).

In the least squares adjustment for GNSS precise positioning for moving platforms, the unknown parameters can be divided into two groups as well. One group is the state parameters of the kinematic platform, such as the time series of the position and velocity parameters. The other group consists of global parameters, which are connected to all or some part of the data, such as ambiguity parameters. Normally we are interested in the state parameters of the kinematic platform; however, the global parameters such as ambiguity parameters have a huge impact on the state parameters. That means, if the global parameters are inaccurate, it is hard to obtain precise solutions of the state parameters.

In order to obtain highly precise state results for kinematic platforms, the principle of the elimination of nuisance parameters in least squares is used: Firstly, the state parameters are eliminated for every epoch. Secondly, the global parameters are calculated using all data. Finally, by backward substitution of the estimated global parameters into the original equations, the state parameters are calculated at every epoch. This method is based on the classic least squares adjustment as follows.

3.2.1 Classic Least Squares Adjustment

The classic least squares principle can be summarised as follows (Gelb, 1974, p. 23; Mikhail and Ackermann, 1976, pp.103-105; Koch, 1999, p. 188; Ghilani, 2010, pp. 178-182):

The GNSS observational model at epoch i is given as

$$L_i = A_i X_i + e_i, \tag{3.1}$$

where L_i is an $n \times 1$ observation vector at epoch i, A_i is $n \times m$ design matrix, X_i denotes a $m \times 1$ unknown parameter vector, e_i is the theoretical measurement error vector with zero mean and covariance matrix Σ_i, with $\Sigma_i = \sigma_0^2 P_i^{-1}$, where σ_0^2 is the theoretical variance of unit weight and P_i denotes the weight matrix of the observations.

If the $n \times 1$ vector $\hat{L}_i$ denotes the estimator of the expected values $\mathrm{E}(L_i)$ of the observations, then the estimator V_i (which is an $n \times 1$ vector) of the vector e_i of the errors in Eq. (3.1) is given by

$$V_i = \hat{L}_i - L_i, \tag{3.2}$$

with

$$\hat{L}_i = A_i \hat{X}_i, \tag{3.3}$$

where $\hat{X}_i$ is the estimator of the vector X_i of unknown parameters at epoch i. The vector V_i is called vector of the residuals, which plays an important role after the adjustment process. It is basically useful to analyze the elements of V_i in order to test the adequacy of the model (Mikhail and Ackermann, 1976, p. 104).

Following the well-known basic principle of the least squares adjustment (Mikhail and Ackermann, 1976, p. 104; Koch, 1999, p. 187; Ghilani, 2010, p. 179),

$$V_i^{\mathrm{T}} P_i V_i \rightarrow \text{minimum}, \tag{3.4}$$

the solution of Eq. (3.2) and Eq. (3.3) is given by,

$$\hat{X}_i = (A_i^{\mathrm{T}} P_i A_i)^{-1} A_i^{\mathrm{T}} P_i L_i, \tag{3.5}$$

with the covariance matrix $\Sigma_{\hat{X}_i}$ of the estimated parameter vector $\hat{X}_i$ as,

$$\Sigma_{\hat{X}_i} = \hat{\sigma}_0^2 Q_{\hat{X}_i} , \tag{3.6}$$

with

$$Q_{\hat{X}_i} = (A_i^{\mathrm{T}} P_i A_i)^{-1} , \tag{3.7}$$

where $Q_{\hat{X}_i}$ is the cofactor matrix. The empirical a posteriori variance of the unit weight $\hat{\sigma}_0^2$ can be computed from the residual vector V_i as follows

$$\hat{\sigma}_0^2 = \frac{V_i^{\mathrm{T}} P_i V_i}{n-m} = \frac{L_i^{\mathrm{T}} P_i L_i - L_i^{\mathrm{T}} P_i A_i \hat{X}_i}{n-m} , \tag{3.8}$$

where $n > m$.

3.2.2 Nuisance Parameter Elimination in Least Squares

Following the principles of the classic least squares adjustment (Gelb, 1974, p. 23; Mikhail and Ackermann, 1976, pp.103-105; Koch, 1999, p. 188; Ghilani, 2010, pp. 178-182), the unknown parameters can be divided into two groups, one with the state parameters (i.e. local parameters), and the other one with the global parameters. The error equation of the GNSS observational model at epoch i is given by

$$V_i = A_i \hat{X}_i + B_i \hat{Y} - L_i , \tag{3.9}$$

where V_i is the residual vector of dimension $n \times 1$, the vector $\hat{X}_i$ denotes the $m \times 1$ estimated state vector and A_i is the $n \times m$ design matrix of the state vector at the epoch i, the vector $\hat{Y}$ denotes the $k \times 1$ estimated vector of global parameters for all observation periods and B_i is the $n \times k$ design matrix of the global parameter vector at epoch i, L_i is the $n \times 1$ observation vector with zero mean and the covariance matrix Σ_i, with $\Sigma_i = \sigma_0^2 P_i^{-1}$, σ_0^2 is the theoretical variance of unit weight and P_i denotes the weight matrix of the observations.

The normal equation for the least squares adjustment derived from Eq. (3.9) is

$$\begin{bmatrix} A_i^T P_i A_i & A_i^T P_i B_i \\ B_i^T P_i A_i & B_i^T P_i B_i \end{bmatrix} \cdot \begin{bmatrix} \hat{X}_i \\ \hat{Y} \end{bmatrix} = \begin{bmatrix} A_i^T P_i L_i \\ B_i^T P_i L_i \end{bmatrix} . \tag{3.10}$$

Introducing $\begin{bmatrix} N_{XX,i} & N_{XY,i} \\ N_{YX,i} & N_{YY,i} \end{bmatrix} = \begin{bmatrix} A_i^T P_i A_i & A_i^T P_i B_i \\ B_i^T P_i A_i & B_i^T P_i B_i \end{bmatrix}$, and $\begin{bmatrix} U_{X,i} \\ U_{Y,i} \end{bmatrix} = \begin{bmatrix} A_i^T P_i L_i \\ B_i^T P_i L_i \end{bmatrix}$, the Eq. (3.10) can be written as

$$\begin{bmatrix} N_{XX,i} & N_{XY,i} \\ N_{YX,i} & N_{YY,i} \end{bmatrix} \cdot \begin{bmatrix} \hat{X}_i \\ \hat{Y} \end{bmatrix} = \begin{bmatrix} U_{X,i} \\ U_{Y,i} \end{bmatrix}. \tag{3.11}$$

Based on the theory of the equivalent elimination of nuisance parameters (Zhou, 1985; Schaffrin and Grafarend, 1986; Xu, 2002; Schaffrin, 2004; Xu, 2007, p. 146; Shen and Xu, 2008), the estimated state parameter vector $\hat{X}_i$ can be equivalently eliminated at epoch i, and then, the equivalent normal equation of the global parameter vector $\hat{Y}$ can be given as

$$(N_{YY,i} - N_{YX,i} N_{XX,i}^{-1} N_{XY,i}) \cdot \hat{Y} = U_{Y,i} - N_{YX,i} N_{XX,i}^{-1} U_{X,i} . \tag{3.12}$$

Introducing $\overline{N}_{YY,i} = N_{YY,i} - N_{YX,i} N_{XX,i}^{-1} N_{XY,i}$ and $\overline{U}_{Y,i} = U_{Y,i} - N_{YX,i} N_{XX,i}^{-1} U_{X,i}$, the Eq. (3.12) can be written as

$$\overline{N}_{YY,i} \cdot \hat{Y} = \overline{U}_{Y,i} . \tag{3.13}$$

According to Xu (2002) and Xu (2007, p. 124), let’s define the auxiliary matrix J by

$$J = A_i (A_i^{\mathrm{T}} P_i A_i)^{-1} A_i^{\mathrm{T}} P_i . \tag{3.14}$$

Hereby,

$$\overline{N}_{YY,i} = B_i^{\mathrm{T}} P_i (I - J_i) B_i = B_i^{\mathrm{T}} P_i (I - J_i)(I - J_i) B_i = B_i^{\mathrm{T}} (I - J_i)^{\mathrm{T}} P_i (I - J_i) B_i \tag{3.15}$$

and

$$\overline{U}_{Y,i} = B_i^{\mathrm{T}} P_i (I - J_i) L_i = B_i^{\mathrm{T}} (I - J_i)^{\mathrm{T}} P_i L_i . \tag{3.16}$$

where I is the identity matrix. By introducing $D_i = (I - J_i) B_i$, Eq. (3.13) can be rewritten as

$$D_i^{\mathrm{T}} P_i D_i \hat{Y} = D_i^{\mathrm{T}} P_i L_i , \tag{3.17}$$

then, Eq. (3.17) can be seen as the normal equation of the transformed error equation of $\hat{Y}$,

$$W_i = D_i \hat{Y} - L_i \tag{3.18}$$

where, W_i is the respective residual vector having the meaning as V_i in Eq. (3.9). L_i is the original observation vector with its associated weight matrix P_i.

Following the well-known basic principle of the classic least squares adjustment (cf. Section 3.2.1), the solution of Eq. (3.13) is given by,

$$\hat{Y} = (\bar{N}_{YY,i})^{-1}\bar{U}_{Y,i}, \tag{3.19}$$

with the covariance matrix $\Sigma_{\hat{Y}}$ of the estimated parameter vector $\hat{Y}$ as,

$$\Sigma_{\hat{Y}} = \hat{\sigma}_Y^2(\bar{N}_{YY,i})^{-1}, \tag{3.20}$$

Following Eq. (3.8) and considering Eq. (3.18), the empirical a posteriori variance of the unit weight $\hat{\sigma}_Y^2$ at epoch i can be computed from the residual vector W_i as follows

$$\hat{\sigma}_Y^2 = \frac{W_i^{\mathrm{T}} P_i W_i}{n-k} = \frac{L_i^{\mathrm{T}} P_i L_i - L_i^{\mathrm{T}} P_i D_i \hat{Y}}{n-k}, \tag{3.21}$$

where $n > k$.

Here, the data of all observation periods contribute to the calculation of the global parameter vector $\hat{Y}$. Eq. (3.13) can be summed from the first epoch to the last epoch z. The equivalent normal equation for the global parameter vector $\hat{Y}$ is given as

$$\sum_{i=1}^{z} \bar{N}_{YY,i} \cdot \hat{Y} = \sum_{i=1}^{z} \bar{U}_{Y,i}. \tag{3.22}$$

The solution of the global parameter vector $\hat{Y}$ and its covariance matrix $\Sigma_{\hat{Y}}$ can be written as

$$\hat{Y} = \left(\sum_{i=1}^{z} \bar{N}_{YY,i}\right)^{-1} \cdot \left(\sum_{i=1}^{z} \bar{U}_{Y,i}\right) \tag{3.23}$$

and

$$\Sigma_{\hat{Y}} = \hat{\sigma}_Y^2 \left(\sum_{i=1}^{z} \bar{N}_{YY,i}\right)^{-1}. \tag{3.24}$$

Following Eq. (3.21), the empirical a posteriori variance of the unit weight $\hat{\sigma}_Y^2$ of all period can be computed as follows

$$\hat{\sigma}_Y^2 = \frac{\sum_{i=1}^{z} W_i^{\mathrm{T}} P_i W_i}{\left(\sum_{i=1}^{z} n_i\right) - k} = \frac{\sum_{i=1}^{z} L_i^{\mathrm{T}} P_i L_i - \sum_{i=1}^{z} L_i^{\mathrm{T}} P_i D_i \hat{Y}}{\left(\sum_{i=1}^{z} n_i\right) - k}. \tag{3.25}$$

After the global parameters have been calculated, taking them back to the original normal equation Eq. (3.11), the state vectors $\hat{X}_i$ $(i = 1, 2, \ldots, z)$ and their covariance matrices $\boldsymbol{\Sigma}_{\hat{X}_i}$ can be calculated as

$$\hat{X}_i = N_{XX,i}^{-1} \cdot (U_{X,i} - N_{XY,i} \cdot \hat{Y}) \tag{3.26}$$

and

$$\Sigma_{\hat{X}_i} = N_{XX,i}^{-1} + (N_{XX,i}^{-1} \cdot N_{XY,i}) \cdot \Sigma_{\hat{Y}} \cdot (N_{XX,i}^{-1} \cdot N_{XY,i})^{\mathrm{T}} . \tag{3.27}$$

The formulas Eq. (3.9) to Eq. (3.27) are the complete formulas for the algorithm for the elimination of nuisance parameters in the least squares adjustment.

The basic idea of this method is, all of the data are used to calculate global parameters firstly, then the local parameters are calculated based on the precise global parameters. The solution is identical to that of solving Eq. (3.11) and Eq. (3.12) together (Xu, 2002). This elimination process is the same as the Gauss-Jordan algorithm, which is often used for inverting the normal matrix (or solving the linear equation system) (Xu, 2002).

The elimination of nuisance parameters in least squares adjustment is very useful for GNSS kinematic data processing while the Integer Ambiguity Resolution (IAR) is a key approach in high-precision GNSS applications. Without an exact determination of the integer ambiguities, any precise positioning at centimetre level based on GNSS phase observations cannot be achieved (Chen, 1998).

Using the described method for the elimination of nuisance parameters in the least squares adjustment, the ambiguity parameters of the carrier phase observations can be calculated accurately in a first step, where the ambiguity values are obtained as float solutions. These values are then used to fix the integer ambiguities. Then the fixed ambiguities are taken to transform the ambiguous carrier phases into ultra-precise pseudoranges which are eventually used for the precise positioning. Several different methods have been developed to improve the ambiguity estimation (Blewitt, 1989; Teunissen et al., 1996; Teunissen et al., 1999; Wang et al., 2001; Ge et al., 2008; Teunissen et al., 2010). One of the most popular algorithms is the LAMBDAD method (Teunissen et al., 1996) since this approach is numerically efficient and statistically optimum. This method maximizes the probability of a correct integer ambiguity estimation and its integer search is efficient.

3.3 Two-way Kalman Filter

The Kalman filter has been widely applied in many fields such as geodetic measurements (Herring et al., 1990), GNSS kinematic precise positioning (Chen, 1998; Yang, 2010), satellite orbit determination (He and Xu, 2011; Xu et al., 2012), GPS/INS integration (Mohamed and Schwarz, 1999; Mercado et al., 2013) etc. Application of the Kalman filter has become standard for the estimation of linear state space models.

The classic Kalman filter will be described, and then the two-way Kalman filter will be discussed.

3.3.1 Classic Kalman Filter

The system state equation and observation equation of GNSS kinematic positioning are generally expressed as (Schwarz et al., 1989; Koch and Yang, 1998; Yang, 2010)

$$X_i = \Phi_{i.i-1} X_{i-1} + W_i \tag{3.28}$$

and

$$L_i = A_i X_i + e_i , \tag{3.29}$$

where the subscript i is the time t_i, X_i and X_{i-1} are $m \times 1$ state vectors at epoch t_i and t_{i-1}, respectively, $\Phi_{i.i-1}$ is an $m \times m$ transition matrix from state X_{i-1} to X_i, W_i is an $m \times 1$ error vector of system state model with zero mean and covariance matrix Σ_{W_i}, L_i is an $n \times 1$ measurement vector at epoch t_i, A_i is an $n \times m$ design matrix and e_i is a measurement error vector with zero mean and covariance matrix Σ_i, here $\Sigma_i = \sigma_0^2 P_i^{-1}$, σ_0^2 is the variance of unit weight and P_i denotes the weight matrix of observations.

The predicted state vector $\bar{X}_i$ and its covariance matrix $\Sigma_{\bar{X}_i}$ are denoted by

$$\bar{X}_i = \Phi_{i,i-1} \hat{X}_{i-1} \tag{3.30}$$

and

$$\Sigma_{\bar{X}_i} = \Phi_{i,i-1} \Sigma_{\hat{X}_{i-1}} \Phi_{i,i-1}^T + \Sigma_{W_i} . \tag{3.31}$$

The transition matrix $\Phi_{i.i-1}$ of state vector X_i and the covariance matrix Σ_{W_i} of error vector W_i of Kalman filter system state model are given in the literature (Schwarz et al., 1989; Chen, 1998; Abdel-salam, 2005; Yang, 2010).

The error equations for the predicted state vector and the measurement vector are

$$V_{\bar{X}_i} = \hat{X}_i - \bar{X}_i \tag{3.32}$$

and

$$V_i = A_i \hat{X}_i - L_i , \tag{3.33}$$

where $V_{\bar{X}_i}$ and V_i denote the estimator of the vector W_i and e_i, respectively.

According to the classical Kalman filter theory (Kalman, 1960; Kalman and Bucy, 1961; Huep, 1985), the state estimate at epoch i can be expressed as

$$\hat{X}_i = \bar{X}_i + K_i \left(L_i - A_i \bar{X}_i \right), \tag{3.34}$$

with its covariance matrix $\Sigma_{\hat{X}_i}$,

$$\Sigma_{\hat{X}_i} = \left(I - K_i A_i \right) \Sigma_{\bar{X}_i} \tag{3.35}$$

and

$$K_i = \Sigma_{\bar{X}_i} A_i^{\mathrm{T}} \left(A_i \Sigma_{\bar{X}_i} A_i^{\mathrm{T}} + \Sigma_i \right)^{-1}, \tag{3.36}$$

where I is the identity matrix and K_i is the so-called Kalman gain matrix.

3.3.2 Two-way Kalman Filter

There are three types of applications of the Kalman filter for GNSS data analysis: smoothing, filtering and predicting representing the process of providing solutions for past, current, and future epochs, respectively (Chen, 1998). In this thesis, to improve the accuracy of the state vector of the kinematic platform, the two-way Kalman filter is applied, where the filter is performed in both forward and backward directions (He and Xu, 2009; He and Xu, 2011; Xu et al., 2012). A smoothed solution for the two-way Kalman filter and its covariance matrix can be given by

$$\hat{X}_{i,\mathrm{two}} = (\Sigma_{\hat{X}_{i,f}}^{-1} + \Sigma_{\hat{X}_{i,b}}^{-1})^{-1} (\Sigma_{\hat{X}_{i,f}}^{-1} \cdot \hat{X}_{i,f} + \Sigma_{\hat{X}_{i,b}}^{-1} \cdot \hat{X}_{i,b}) \tag{3.37}$$

and

$$\Sigma_{\hat{X}_{i,\mathrm{two}}} = (\Sigma_{\hat{X}_{i,f}}^{-1} + \Sigma_{\hat{X}_{i,b}}^{-1})^{-1}, \tag{3.38}$$

where $\hat{X}_{i,two}$ and $\Sigma_{\hat{X}_{i,\mathrm{two}}}$ are the smoothed solution and its covariance matrix, $\hat{X}_{i,f}$ and $\Sigma_{\hat{X}_{i,f}}$ are the forward solution and its covariance matrix, $\hat{X}_{i,b}$ and $\Sigma_{\hat{X}_{i,b}}$ are the backward solution and its covariance matrix.

The two-way Kalman filter can be seen as a weighted average of the estimated states from the forward and backward runs. By combining the forward and backward results, measurements before and after a given epoch can contribute to the corresponding state estimate, which improves the accuracy of the state vector of the kinematic platform. This method is also useful for the estimation of accurate integer ambiguity solutions. It should be pointed out that the proposed methods are suitable for post-processing of GNSS precise positioning.

3.4 Precision and Reliability Evaluation

The results obtained in the GNSS precise positioning always contain uncertainties, which include random errors, systematic errors, and outliers as well as coloured noise. There are many different measures for evaluating the quality of the positioning results, such as precision, accuracy, reliability and uncertainty. Precision as expressed by the a posteriori obtained covariance matrix of the coordinates, means the survey's characteristics by propagating random errors (Teunissen and Kleusberg, 1998). Accuracy is the closeness of the obtained positioning results to the true values. Typically, an independent or alternative measurement technique is required to assess accuracy. Reliability describes the survey's ability to check for the presence of modelling errors, refers to the ability to detect blunders and to estimate the effects that undetected blunders may cause on a solution (Baarda, 1968; Leick, 2004, p. 161). Uncertainty can refer to vagueness, ambiguity, or anything that is undetermined (Shi, 2010). Although uncertainty comprises many different factors, this thesis will focus attention to a narrower notion of uncertainty, namely that a (GNSS) survey is considered to be qualified for its purpose when it is delivered with sufficient precision and accuracy. The terms precision and accuracy are often used to describe how good the estimated position for a GNSS receiver is (Dixon, 1991).

A distinction must be made between accuracy and precision. Accuracy is the degree of closeness of an estimate to its truth. Generally, it can be measured using root mean square of errors (RMS). Precision is the degree of closeness of observations to their means. It can be measured with standard deviation (SDev).

To evaluate the results of GNSS kinematic precise positioning, based on kinematic processing, here in this study a static and a kinematic experiment were carried out as described in the following sections.

3.4.1 Static Experiment

The GNSS data of a static experiment can be processed kinematically. When the true value of the static station coordinate is unknown, we can compare the kinematic GNSS results with its mean value. The precision is described by

$$\mathrm{SDev} = \sqrt{\frac{1}{z}\sum_{i=1}^{z}(\hat{X}_i - \mu)^2} \ , \tag{3.39}$$

where SDev is the precision of the GNSS results, z is the number of epochs of the GNSS observations, $\hat{X}_i$ is position and/or velocity of the static station at epoch i, μ is the mean value of $\hat{X}_i$, (i.e. $\mu = \frac{1}{z}\sum_{i=1}^{z}\hat{X}_i$). But since precision is an internal statistical evaluation of the kinematic GNSS results, it cannot show the systematic errors. Therefore an additional external evaluation is needed.

If the true value of static station parameters is known as X_{true}, we can compare the GNSS kinematic results with this true value. The more objective accuracy is described as

$$\text{RMS} = \sqrt{\frac{1}{z}\sum_{i=1}^{z}(\hat{X}_i - X_{\text{true}})^2}\ . \tag{3.40}$$

Many GNSS tracking stations like those of the International GNSS Service (IGS) are widely distributed all over the world, shown in Figure 3.1. The highly accurate coordinate estimates and the GNSS observation data of the IGS stations are available on the IGS website (http://www.igs.org/). That means IGS tracking stations can be used for static experiments to check the algorithms and software as applied here in this thesis.

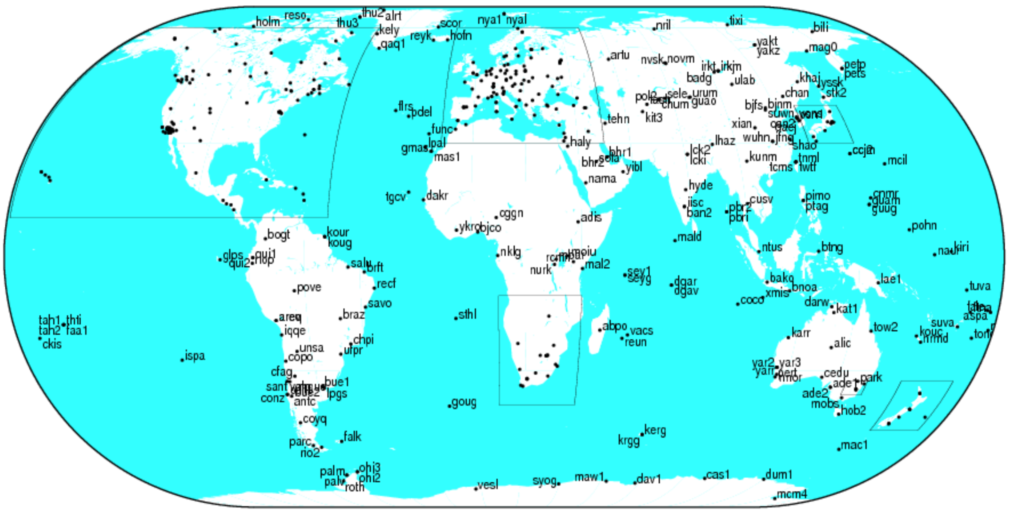

Figure 3.1: The IGS tracking network (IGS, 2014)

3.4.2 Kinematic Experiment

For the kinematic experiment, an evaluation of the results is more difficult than for the static experiment, since the true parameters of the kinematic station at every time epoch are difficult to know. In order to check the algorithm and software, the following evaluation methods were used.

Firstly, a special testing equipment or testing place has been constructed, where a GNSS antenna can be moved over certain horizontal or vertical distances which are measured with mm accuracy by rulers. In this thesis, the antenna movement experiment has been carried out on the roof of building A17 on the Telegrafenberg campus in Potsdam, to check the algorithms and the software. The experiment equipment is shown in Figure 3.2 for horizontal and in Figure 3.3 for vertical movement of an antenna. Both equipments have a fixed ruler which can be used to record the relative position of the moved antenna. The relative positions measured with the ruler were compared with the GNSS results to get an independent picture of the real accuracy of the GNSS positioning. In this thesis only the vertically moving test antenna was applied (cf. Section 4.2.2).

Figure 3.2: Equipment for the horizontal movement experiment of a GNSS antenna

Secondly, the GNSS results of a short kinematic baseline are used to check the results of a long kinematic baseline: The kinematic GNSS antenna in the aforementioned experiment was used to form a short as well as a long baseline. Since the results of the DD kinematic GNSS positioning for a short baseline of about 2 m are of millimetre accuracy they can be considered as true position values of the kinematic antenna w.r.t. to those for a long baseline of about 1000 km. The objective, independent accuracy can be obtained by comparison of the GNSS results for the short and long baselines. The principle can be mathematically written as

$$\mathrm{RMS} = \sqrt{\frac{1}{z}\sum_{i=1}^{z}(\hat{X}_{i,\mathrm{long}} - \hat{X}_{i,\mathrm{short}})^2}\ , \tag{3.41}$$

where $\hat{X}_{i,\mathrm{long}}$ and $\hat{X}_{i,\mathrm{short}}$ are the state vectors of the same kinematic station obtained for the long and the short baseline at the same time, respectively.

Figure 3.3: Equipment for the vertical movement experiment of a GNSS antenna

Finally, the methods as described above are effective in the case of kinematic stations for low dynamic and in a small area, since the position of the kinematic station can be estimated accurately by other approaches such as short kinematic baseline. However, for a highly dynamic and long kinematic baseline situation such as on the HALO aircraft (Figure 1.2), it is difficult to know the true value of the exact position of the moving station at every epoch. Therefore, in order to investigate the accuracy of the kinematic results, two relative testing methods are used.

One relative testing method is based on the fact that the distances between two antennas on a moving kinematic platform are always constant. This fact is used to check the results of the highly dynamic and long baseline kinematic station. Firstly, the positions of the kinematic stations are calculated. Then the length of the baseline between the two kinematic stations was calculated. The accuracy of the kinematic results was then checked by inspection of the temporal variations of the computed length of the baseline between the two kinematic antennas. This principle can be mathematically expressed by

$$\mathrm{RMS} = \sqrt{\frac{1}{z}\sum_{i=1}^{z}(d_i - d_{\mathrm{true}})^2} \tag{3.42}$$

and

$$d_i = \sqrt{(x_i^1 - x_i^2)^2 + (y_i^1 - y_i^2)^2 + (z_i^1 - z_i^2)^2}\ , \tag{3.43}$$

where d_i denotes the distance between the two kinematic antennas at epoch i, d_{true} is the true distance between the two kinematic antennas, which can be measured independently before the aircraft starts. (x_i, y_i, z_i) are the coordinates of kinematic station at epoch i. If the true distance is unknown, the mean value of distance is used for this evaluation. The principle can be expressed as

$$\text{SDev} = \sqrt{\frac{1}{z}\sum_{i=1}^{z}(d_i - d_{\text{mean}})^2}\ , \tag{3.44}$$

where d_{mean} is the mean value over the whole measurement period of the distance between two kinematic antennas.

Another relative testing method is based on the fact that the difference of positioning results coming from two GNSS receivers connected with the same GNSS antenna is theoretically zero. This can also be used to check the results of the highly dynamic and long baseline kinematic station. The principle can be expressed mathematically as

$$\text{RMS} = \sqrt{\frac{1}{z}\sum_{i=1}^{z}(\hat{X}_i^{\text{rec\_1}} - \hat{X}_i^{\text{rec\_2}})^2}\ , \tag{3.45}$$

where $\hat{X}_i^{\text{rec\_1}}$ and $\hat{X}_i^{\text{rec\_2}}$ are the position vectors of same antenna coming from two receivers.

3.4.3 Reliability

For use in geodetic networks, Baarda (1968) developed his testing procedure that ultimately led to a theory of “reliability” with a number of applications (Baarda, 1976; Förstner, 1983; Li, 1985; Förstner, 1987; Li, 1989; Biacs et al., 1990; Schaffrin, 1997; Hewitson and Wang, 2006; Knight et al., 2010). The reliability of GNSS is essentially dependent on the redundancy and geometry of the measurement system as well. Reliability refers to the consistency of the results provided by a system, dictating the extent to which they can be trusted, or relied upon. More specifically, in terms of GNSS kinematic positioning, reliability comprises the ability of the system to detect outliers, referred to as internal reliability, and a measure of the influence of undetectable outliers on the parameter estimations, referred to as external reliability (Baarda, 1968).

The measure of internal reliability is quantified as the minimal detectable bias (MDB) and is indicated by the lower bound for detectable outliers. The MDB is the magnitude of the smallest bias that can be detected for a specific level of confidence and is determined, for correlated measurements (Baarda, 1968; Förstner, 1987) by

$$\nabla_0 l_i = \sigma_{l_i} \frac{\delta_0}{\sqrt{r_i}}, \tag{3.46}$$

where $\nabla_0 l_i$ is the lower bound for detectable outliers, the standard deviation σ_{l_i} is the i^{th} ($i = 1, 2, \ldots, n$) component of precision of the GNSS observations. The lower bound δ_0 is the non-centrality parameter which depends on the given false alarm rate α_0 and the delectability β_0. If the significance level is $1 - \alpha_0 = 99.9\%$, then the gross errors ∇l_i smaller than $4.13 \cdot \sigma_{l_i}$ are not detectable with a probability larger than $\beta_0 = 80\%$ (Förstner, 1987). The redundancy number r_i of the i^{th} component of the GNSS observations is defined (Baarda, 1968; Förstner, 1983; Li, 1985) by

$$r_i = (I - A(A^{\mathrm{T}} P A)^{-1} A^{\mathrm{T}} P)_{ii}, \tag{3.47}$$

where I is the identity matrix, the definitions of matrices A and P can be found in Section 3.2.1. Hence, the smaller the redundancy number r_i of the observation, the larger a gross error has to be in order to be detectable. This is reasonable, because the residuals are smaller in this case (Förstner, 1987).

A comparison of the boundary values for heterogeneous observations is not directly possible. Thus, the controllability of the observation was written as (Li, 1985, p. 20; Förstner, 1987)

$$\delta'_{0,i} = \frac{\nabla_0 l_i}{\sigma_{l_i}} = \frac{\delta_0}{\sqrt{r_i}}, \tag{3.48}$$

Therefore, $\delta'_{0,i}$ is a factor for the standard deviation σ_{l_i} of the observation needed to obtain the boundary value $\nabla_0 l_i$. With the controllability factor $\delta'_{0,i}$ we finally get

$$\nabla_0 l_i = \delta'_{0,i} \cdot \sigma_{l_i}. \tag{3.49}$$

The controllability value $\delta'_{0,i}$ is thus the factor by which a gross error at least has to be at least larger than the standard deviation of the observation to be detectable with a probability of at least β_0 (Förstner, 1987).

External reliability of the system is characterized by the extent to which an MDB affects the estimated parameters (Baarda, 1968). Gross errors smaller than the boundary values $\nabla_0 l_i$ may stay undetected and contaminate the result. The maximum influence of undetectable gross errors on to the estimates can be determined by sensitivity or robustness factor $\bar{\delta}_{0,i}$ (Li, 1985, p. 21; Förstner, 1987; Leick, 2004, p. 169),

$$\bar{\delta}_{0,i} = \delta_0 \sqrt{\frac{u_i}{r_i}} = \delta_0 \sqrt{\frac{1-r_i}{r_i}} \ , \tag{3.50}$$

where, $u_i = 1 - r_i = (A(A^{\mathrm{T}}PA)^{-1}A^{\mathrm{T}}P)_{ii}$, the meaning of matrices A and P is same as in Eq. (3.47). These sensitivity or robustness factors $\bar{\delta}_{0,i}$ measure the external reliability according to Baarda (1968). There is one such value for each observation. If the $\bar{\delta}_{0,i}$ are same order of magnitude, the network is homogeneous with respect to external reliability. If r_i is small, the external reliability factor becomes large and the global falsification caused by a blunder can be significant. It follows that small redundancy numbers are not desirable (Leick, 2004, p. 169).

3.5 Influence of the GNSS Receiver Clock in Accuracy Evaluation

3.5.1 Receiver Clock Jump

In the application of GNSS precise positioning, most of the GNSS receivers attempt to keep their internal clocks synchronized to the system time, such as GPS time. This is done by periodically adjusting the clock by applying time jumps. The actual mechanisms of receiver clock jumps are typically proprietary (Kim and Langley, 2001).

In practice, the clock jumps are largely divided into two categories. The first method is a more or less continuous steering, where the clock drift is tuned approximately to zero, and the offset is kept constant within the level of the noise and the tracking jitter. The other method is an application of millisecond jumps which keeps the receiver clock time synchronized within 1 ms w.r.t. the GNSS system time (Kim and Lee, 2012; Zhang et al., 2013).

In order to illustrate the performance of the clock jumps, three GNSS receivers have been tested. Figure 3.4 shows for the receiver 1 (NOVATEL OEM4) how the clock of this receiver is continuous steered. The clocks of the other two receivers 2 and 3 (JAVAD DELTA G3T) are millisecond jumping, which is shown in the Figure 3.5 and Figure 3.6, respectively.

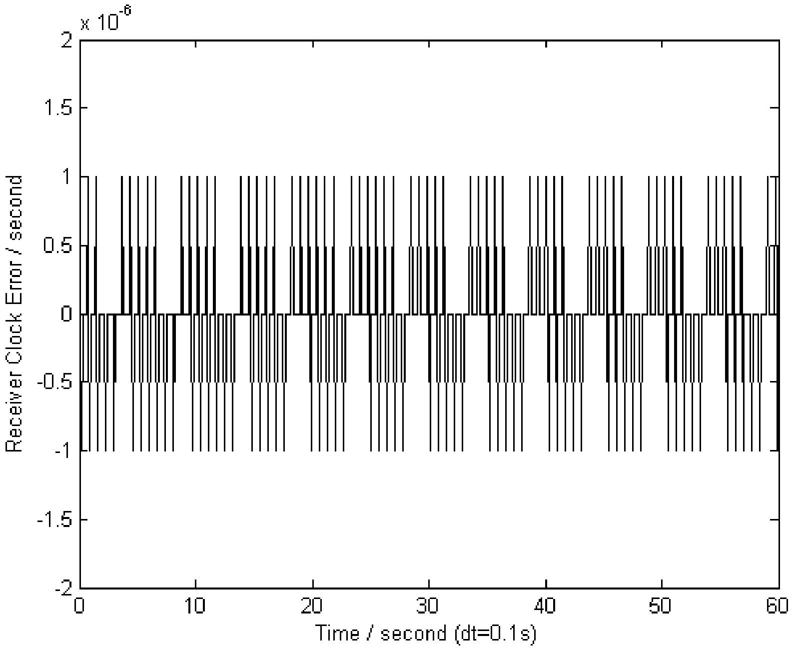

Figure 3.4: The continuous steering of GNSS receiver 1 (NOVATEL OEM4)

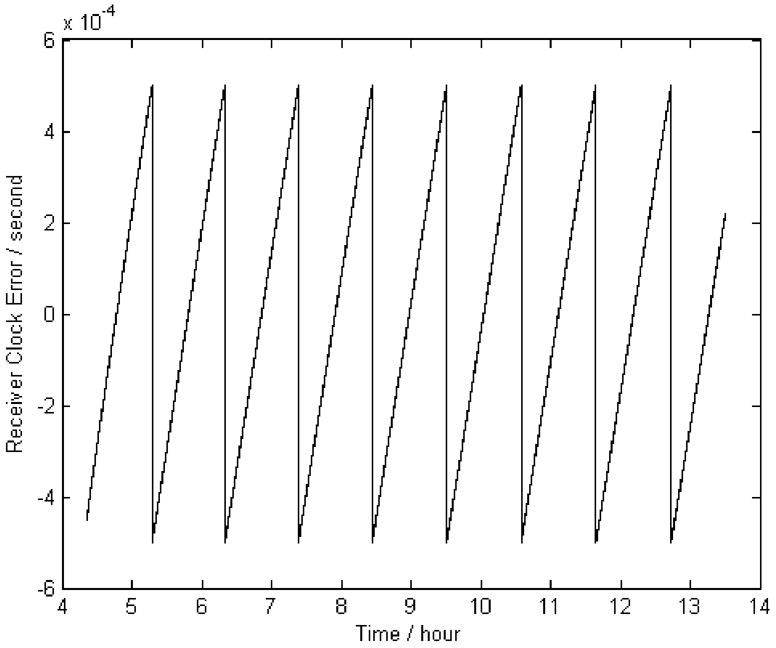

Figure 3.5: The millisecond jumping of GNSS receiver 2 (JAVAD DELTA G3T)

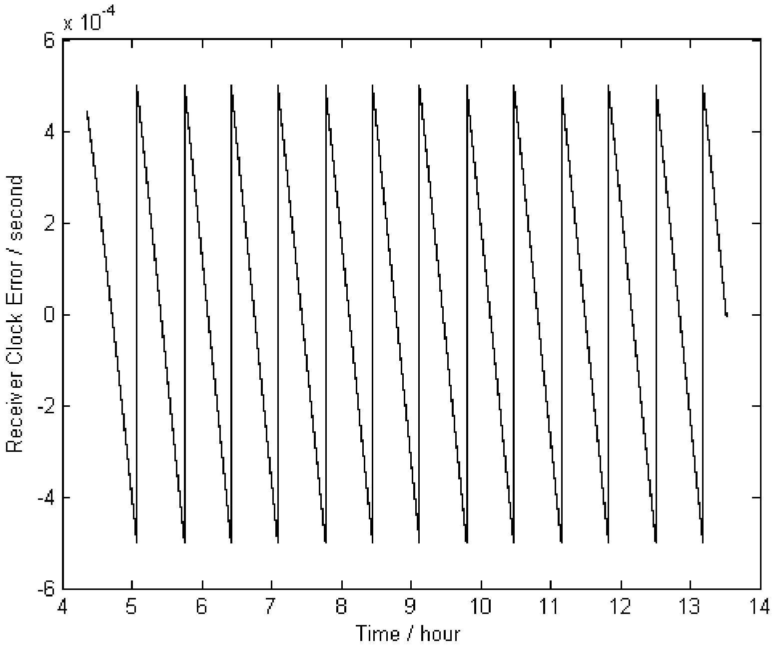

Figure 3.6: The millisecond jumping of GNSS receiver 3 (JAVAD DELTA G3T)

3.5.2 Influence of Receiver Clock in Highly Dynamic Positioning

Due to the influence of GNSS receiver clock errors, which include millisecond jumps, the final result time of the GNSS results at epoch i is different from the time tag which indicates the estimated time instant when the measurements are sampled by the receiver. The receiver clock error must be removed from the time tag of epoch i by

$$t_{\text{result}} = t_{\text{tag}} - \delta t\,, \tag{3.51}$$

where t_{result} is the final result time, t_{tag} is the time tag, δt is the receiver clock error including millisecond jumps.

But in some commercial software, the difference between the final results for the time and the time tag are not considered. Here, usually the time tag is used in the final results. That is not a problem for static and low dynamics positioning when the velocity is low or nought. But in the case of the GEOHALO airborne gravimetric project, the positions of the GNSS antennas at the final time epochs t_{result} are different from the positions at the time tags t_{tag}, since the HALO aircraft has a high velocity of about 450 km/h (corresponding to 125 m/s).

In order to illustrate this issue, highly dynamic GNSS data, coming from the measurement day June 06, 2012 of the GEOHALO project are selected for a test. Two mechanically fixed antennas mounted on the HALO aircraft and connected with JAVAD DELTA G3T receivers 2 and 3 were taken and the distance between both antennas was estimated. In this context two calculation schemata were performed and compared (both receivers were the same as those used for the test as described in Figure 3.5 and Figure 3.6).

Scheme 1: The final results for the distance between both antennas were calculated at the same time tags, without considering the clock errors, like in some commercial software. The result is shown in Figure 3.7.

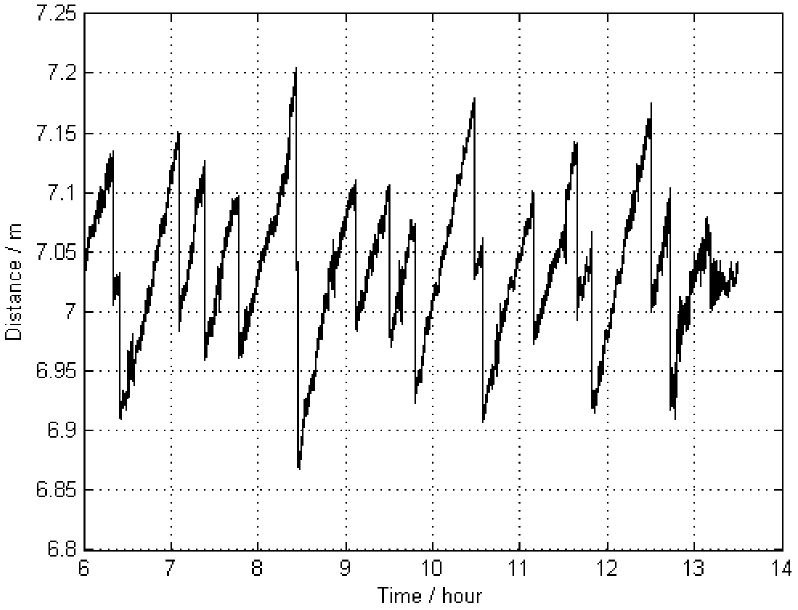

Figure 3.7: Variation of the estimated distance between two mechanically fixed antennas, computed at the same time tags

Scheme 2: The final results for the distance between both antennas were calculated at the epochs of the final results for the receiver time. If the final times of both receivers were different, the results have been interpolated to the same time epoch. The result is shown in Figure 3.8.

The above results show that the time tags should not be used for the timing of the final GNSS results. The described test of distance estimation between two mechanically fixed antennas to evaluate the accuracy of GNSS kinematic positioning shows that the antenna positions must be interpolated to the same time epochs.

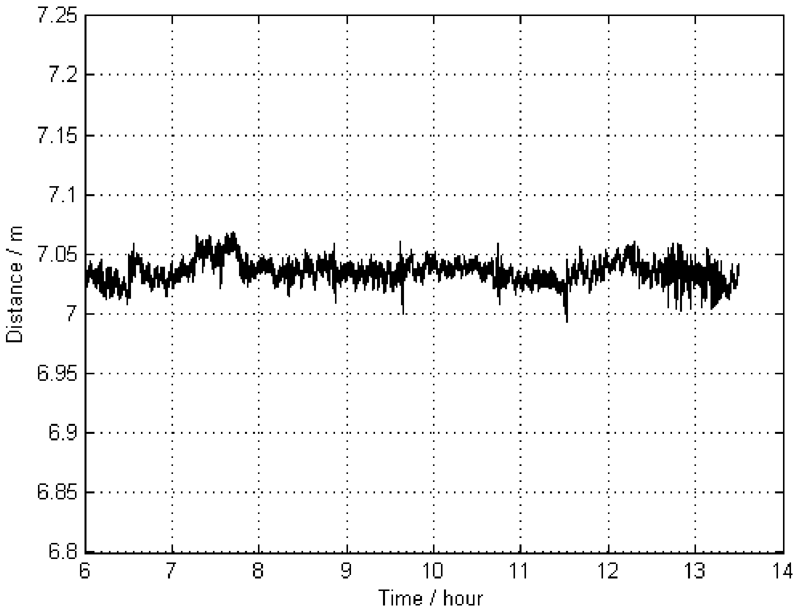

Figure 3.8: Variation of the estimated distance between two mechanically fixed antennas, computed at interpolated time epochs

3.6 Conclusions

In this chapter 3, the parameter estimation algorithms as used for this thesis and the accuracy evaluation method were described. Furthermore, GNSS receiver clock errors and their impact were exemplified.

Firstly, it has been outlined that the algorithm for the elimination of nuisance parameters in least squares adjustment shall be used for the GNSS kinematic precise positioning. This adjustment approach is based on the classic least squares adjustment. The idea of this method is to use the whole measurement data for the calculation of the global parameters in the first step. Then the local parameters are calculated based on the already estimated global parameters.

Secondly, based on the classic Kalman filter, the two-way Kalman filter was proposed for GNSS kinematic precise positioning. The two-way Kalman filter can be regarded as a weighted average of the estimated states from the forward and backward runs. By combining the forward and backward results, measurements before and after a given epoch contribute to the corresponding state estimate, which improves the accuracy of the state vector of the kinematic platform.

It should be pointed out that the outlined methods, i.e. least squares including the elimination of nuisance parameters and the two-way Kalman filter, are suitable to fulfill the high accuracy requirements for airborne gravimetry in the post-processing of GNSS precise positioning. That also means that the outlined methods are capable for an accurate integer ambiguity solution. After the global parameter estimation and an application of the forward

Kalman filter, a precise ambiguity float solution can be obtained, which is the basis for the final integer ambiguity estimation. Without a precise integer ambiguity determination, precise positioning on the centimetre level using GNSS phase observations cannot be achieved.

The explained accuracy evaluation method for GNSS kinematic precise positioning has been applied to data sets recorded in static and kinematic modes, for short as well as long baselines, and at low and high dynamic states. In this thesis, one or more evaluation methods have been used for each example depending on the characteristics of the recorded data.

Finally, the receiver clock errors including the clock jumping were analyzed for highly dynamic GNSS precise positioning. It has been shown that the receiver clock error including clock jumps must be removed from the time tag. If a kinematic estimation for the distance between two mechanically fixed kinematic antennas is used to evaluate the accuracy of GNSS kinematic precise positioning, the antenna positions must be computed for the same time epochs.

4 Kinematic Positioning Based on Multiple Reference Stations

4.1 Introduction

This chapter deals primarily with a GNSS Double Difference (DD) positioning approach based on multiple reference stations, which are used to determine the baseline vectors between simultaneously observing receivers.

This chapter begins with the discussion of GNSS DD positioning. The observation equations for Single Difference (SD) and DD are given in detail. The challenge of DD positioning in a wide region will be presented by means of ultra-short and ultra-long baseline experiments.

Furthermore, an approach of multiple reference stations kinematic positioning based on an a priori constraint is addressed for GNSS precise kinematic positioning in a wide region.

Finally, the robust Kalman filter theory is used to suppress the impact of observation outliers on the trajectory estimates for airborne gravimetry.

4.2 Double Difference Positioning

DD positioning is a classic GNSS data processing method (Blewitt et al., 1988; Blewitt, 1989; Dong and Bock, 1989; Chen, 1998; Leick, 2004, p. 261; Hofmann-Wellenhof et al., 2008, pp. 169-191; Xu, 2007, p. 107). It is regularly used to eliminate or reduce errors between the satellite and the receiver (Bossler et al., 1980; Chu and Yang, 2013). Since the carrier phase observations to GNSS satellites can be used to determine user positions even more precisely than by means of the pseudorange measurements (Roßbach, 2001) the principle of the carrier phase DD positioning is given in this section.

4.2.1 Principle of Classic Double Difference Positioning

A simple example for the DD positioning is illustrated in Figure 4.1. p and q denote the GNSS satellites, r denotes the reference station and k denotes the kinematic station. According to the carrier phase observation Eq. (2.2), the carrier phase observations of the reference station r and the kinematic station k to a common satellite p can be written as

$$\lambda_j^p \cdot \varphi_{r,j}^p = \rho_r^p + c \cdot (dt_r - dt^p) - I_{r,j}^p + T_r^p + \lambda_j^p \cdot N_{r,j}^p + d_{r,j} - d_j^p + e_{r,j}^p \tag{4.1}$$

and

$$\lambda_j^p \cdot \varphi_{k,j}^p = \rho_k^p + c \cdot (dt_k - dt^p) - I_{k,j}^p + T_k^p + \lambda_j^p \cdot N_{k,j}^p + d_{k,j} - d_j^p + e_{k,j}^p . \qquad (4.2)$$

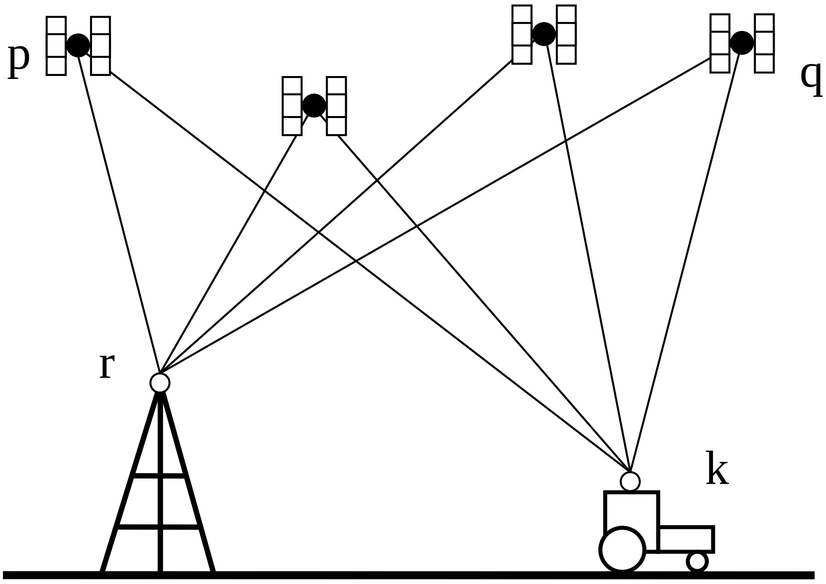

Figure 4.1: An illustration for GNSS DD positioning (Stombaugh and Clement, 1999)

Forming a single difference (Roßbach, 2001; Hofmann-Wellenhof et al., 2008, p. 174), i.e. subtracting the measurement at the reference station from that at the kinematic station, the satellite clock dt^p and the satellite phase bias d_j^p (which are common errors to both observers) are cancelled out by

$$\lambda_j^p \cdot \Delta\varphi_{k-r,j}^p = \Delta\rho_{k-r}^p + c \cdot \Delta dt_{k-r} - \Delta I_{k-r,j}^p + \Delta T_{k-r}^p + \lambda_j^p \cdot \Delta N_{k-r,j}^p + \Delta d_{k-r,j} + \Delta e_{k-r,j}^p , (4.3)$$

where the operator Δ indicates the single difference, for example $\Delta\varphi_{k-r,j}^p$ denotes $\varphi_{k,j}^p - \varphi_{r,j}^p$.

If both antennas are closely located to each other, for example less than 10 km on ground, the tropospheric delays are approximately the same, so that the difference of the tropospheric delays ΔT_{k-r}^p are small and considerably reduced in Eq. (4.3). But for medium and long baselines, the signal travel path through the troposphere is different for each station, especially if the receivers are placed at different altitudes. This may be the case, e.g., in mountainous regions or when an aircraft is approaching an airport (Roßbach, 2001). Thus the tropospheric path delay is not cancelled out in single difference positioning for medium and long baselines.

Supposed the kinematic station is sufficiently close to the reference station, the path of the GNSS satellite signal through the ionosphere will be almost identical for the reference station and the kinematic station. Hence the ionospheric delay can be considerably reduced. This assumption can be made for distances of up to approximately 1000 km (Roßbach, 2001; Dai, 2013). For long baselines, the ionospheric delay can be eliminated to a first order approximation by forming the ionospheric-free linear combination of dual-frequency observations (cf. Section 2.3.1). Thus the differential ionospheric delay $\Delta I^{p}_{k-r,j}$ can be neglected. In this case, Eq. (4.3) can be further simplified to

$$\lambda^{p}_{j} \cdot \Delta\varphi^{p}_{k-r,j} = \Delta\rho^{p}_{k-r} + c \cdot \Delta dt_{k-r} + \Delta T^{p}_{k-r} + \lambda^{p}_{j} \cdot \Delta N^{p}_{k-r,j} + \Delta d_{k-r,j} + \Delta e^{p}_{k-r,j} \,. \qquad (4.4)$$

Such a differential processing is called “single difference positioning”, namely differencing the measurements of two receivers with respect to a common satellite. The single difference positioning is applied to the satellite q with the signal frequency i, which is given as

$$\lambda^{q}_{i} \cdot \Delta\varphi^{q}_{k-r,i} = \Delta\rho^{q}_{k-r} + c \cdot \Delta dt_{k-r} + \Delta T^{q}_{k-r} + \lambda^{q}_{i} \cdot \Delta N^{q}_{k-r,i} + \Delta d_{k-r,i} + \Delta e^{q}_{k-r,i} \,. \qquad (4.5)$$

Assuming the same frequencies $j = i$ (i.e. $\lambda^{p}_{j} = \lambda^{q}_{i}$) for the satellite signals and using the denotation $\nabla\Delta *^{p-q}_{k-r} = \Delta *^{p}_{k-r} - \Delta *^{q}_{k-r}$, differencing two single difference observations, i.e. Eq. (4.4) and Eq. (4.5), at the same sites r and k to two different GNSS satellites p and q gives the DD observation as

$$\lambda^{p}_{j} \cdot \nabla\Delta\varphi^{p-q}_{k-r,j} = \nabla\Delta\rho^{p-q}_{k-r} + \nabla\Delta T^{p-q}_{k-r} + \lambda^{p}_{j} \cdot \nabla\Delta N^{p-q}_{k-r,j} + \nabla\Delta e^{p-q}_{k-r,j} \,. \qquad (4.6)$$

The receiver clock error $c \cdot \Delta dt_{k-r}$ and the carrier phase bias $\Delta d_{k-r,j}$ are common error terms in Eq. (4.4) and Eq. (4.5) and hence can be reduced by DD positioning. That is the main reason why DD are preferably used.

However, if the signal frequencies between the GNSS satellites are different (i.e. $\lambda^{p}_{j} \neq \lambda^{q}_{i}$), as in the case of the GLONASS system, the carrier phase bias $\Delta d_{k-r,j}$ and $\Delta d_{k-r,i}$ cannot be cancelled out from Eq. (4.6). Introducing a shorthand notation, symbolically $\nabla\Delta *^{p-q}_{k-r,ji} = \Delta *^{p}_{k-r,j} - \Delta *^{q}_{k-r,i}$, the DD equation for two different frequency satellites can be given as

$$\begin{gathered} \lambda^{p}_{j} \cdot \Delta\varphi^{p}_{k-r,j} - \lambda^{q}_{i} \cdot \Delta\varphi^{q}_{k-r,i} = \nabla\Delta\rho^{p-q}_{k-r} + \nabla\Delta T^{p-q}_{k-r} + \lambda^{p}_{j} \cdot \Delta N^{p}_{k-r,j} - \lambda^{q}_{i} \cdot \Delta N^{q}_{k-r,i} \\ + \nabla\Delta d_{k-r,ji} + \nabla\Delta e^{p-q}_{k-r,ji} \end{gathered} \,. \qquad (4.7)$$

It is difficult to separate the DD carrier phase bias $\nabla\Delta d_{k-r,ji}$ from the ambiguity parameter, thus the float solution for the GLONASS ambiguities is applied.

The procedure described above is called “DD positioning”, where the satellite orbit error, the satellite clock error and the receiver clock error have been reduced. In case of short baselines, the remaining ionospheric and tropospheric delay can be neglected. For medium and long baselines, the ionosphere-free combination (LC) is used to eliminate the first order ionosphere path delays. The remaining tropospheric delay is reduced by the estimation of the zenith wet delay parameters.

Depending on the principle of the DD processing and the two-way Kalman filter, an example is given in the following.

4.2.2 Experiment and Analysis

For testing the capability of the DD processing for short and long baselines, the mentioned vertical antenna movement experiment (cf. Section 3.4.2) was carried out on the roof of building A17 at GFZ on March 27, 2012. In this experiment, the IGS station POTS was taken as the reference station for the short baseline. Its antenna and receiver type are JAV_RINGANT_G3T NONE and JAVAD TRE_G3TH DELTA, respectively. The experimental station named KIN1 is treated as the moving kinematic station, which is located close to the IGS reference station POTS with a distance of about 2 m. The station KIN1 is shown in Figure 3.3. Antenna and receiver type of KIN1 are the same as those of the IGS station POTS.

The experiment was done in the following way: the antenna of KIN1 was kept at the starting point for 18 minutes. Then the antenna was uplifted by 46 cm and kept at this higher position for 10 minutes. Then the antenna was lowered down to the position of its starting point. After this, the antenna was uplifted again step by step to heights of 10 cm, 20 cm and 40 cm. From this position the antenna was lowered down to the starting point in two steps of 20 cm each. At the end, the antenna was quickly uplifted and lowered between the largest height of 46 cm and the starting position. The north, east and up components of the estimated trajectory for the antenna KIN1 w.r.t. POTS (i.e. the short baseline) are shown in Figure 4.2.

The sampling interval for the GNSS observation data was 1 second. The precision of the pseudorange and carrier phase observations is given to be 1 m and 3 mm, respectively. An elevation cut-off angle of 10 degrees was applied in this test. About 1 hour of GPS and GLONASS data were processed by the HALO_GNSS software which was developed by the author for the GEOHALO project at GFZ. The details about the GNSS integration and the HALO_GNSS software are discussed in Chapter 6 and Chapter 8, respectively.

The results of the kinematic positioning for KIN1 are compared with its initial position on the starting point. This is shown in Figure 4.2 for the north, east and up directions w.r.t. POTS (i.e. the short baseline). The RMS of the north and east directions is 2-3 mm, since the antenna was not moved in the horizontal direction (quadratic mean of north and east). The movement results of the up direction agree well with the true movement log at 3 mm accuracy. Such a high accuracy results is achieved since the common errors between the satellites and receivers are clearly eliminated or reduced by the DD processing in the case of the short baseline. These results can be treated as the true value of the antenna movement.

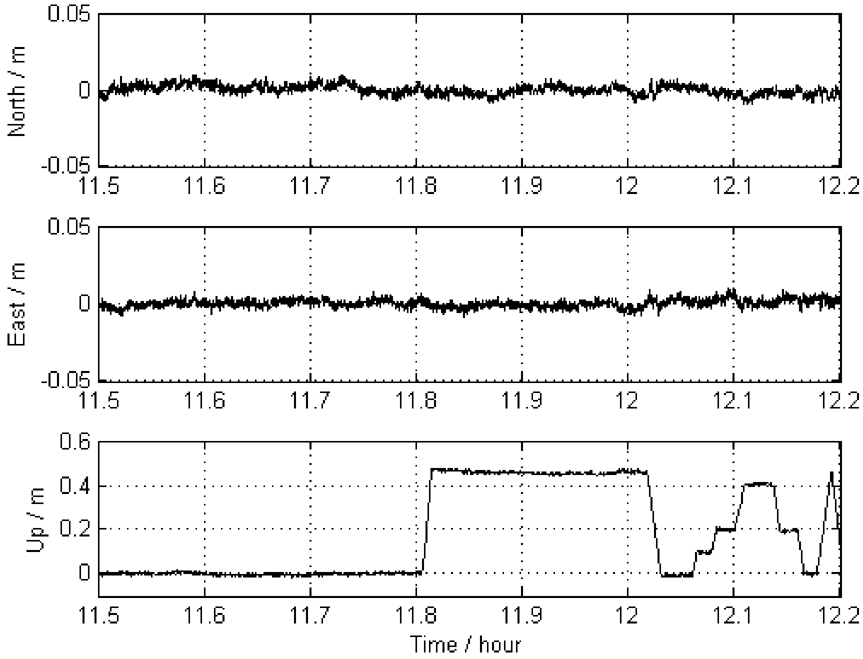

Figure 4.2: The results of the kinematic positioning for the short baseline POTS-KIN1 during the vertical antenna movement experiment

In order to show the performance of the DD positioning in the case of a long baseline, an IGS tracking station far away from Potsdam named MATE (Matera, Italy) was chosen and taken as reference station to form the long baseline together with KIN1 (cf. Figure 4.3). The antenna and receiver type of the IGS station MATE are LEIAT504GG and LEICA GRX1200GGPRO, respectively. The length of this long baseline MATE-KIN1 is 1330 km.

The GNSS observation data of the IGS station MATE on March 27, 2012, were downloaded from the IGS ftp-server (ftp://cddis.gsfc.nasa.gov/gps/data/highrate/) with 1 s sampling rate. This ftp-server is operated by the Crustal Dynamics Data Information System (CDDIS) and provides also GNSS ephemeris data, orbit information and meteorological parameters of the observation stations. The precision of the pseudorange and carrier phase observations is given to be 1 m and 3 mm respectively. An elevation cut-off angle of 10 degrees was applied in this test. The IGS rapid or final products of GNSS satellite orbits and clocks were chosen to apply corrections for satellite orbit and clock errors. The HALO_GNSS software was used for the GNSS data processing. The dual-frequency carrier phase observations were used to form the ionosphere-free linear combination. The parameters of the wet tropospheric zenith path delay for MATE and POTS were employed as well and they are assumed to be known with an uncertainty of 10 cm and a spectral density of $10^{-9}\ \mathrm{m}^2/\mathrm{s}$. The two-way Kalman filter was used for the parameter estimation.

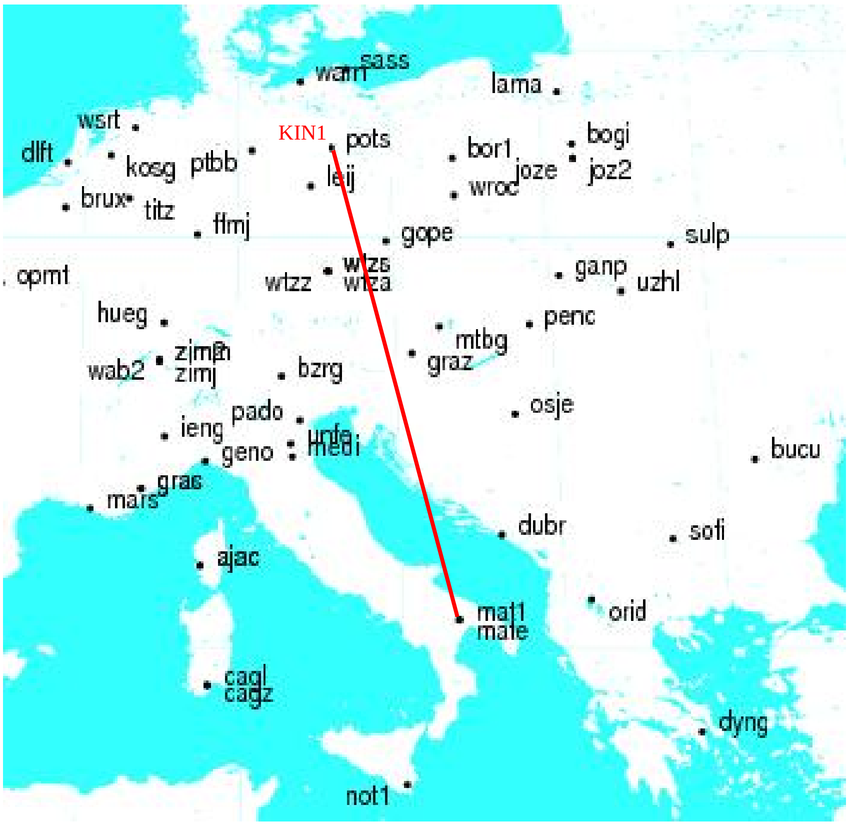

Figure 4.3: The long baseline (MATE-KIN1, 1330 km) (IGS, 2014)

The results of the kinematic DD positioning for KIN1 on the long baseline MATE-KIN1 are shown in Figure 4.4 with its north, east and up components. It shows that there are biases in the trajectory of the kinematic station KIN1.

The results of KIN1 for the long baseline MATE-KIN1 are compared with the “true values”, of the short baseline POTS-KIN1. The statistics of the comparison given in Table 4.1 shows that the achieved accuracy is 0.012 m, 0.022 m and 0.068 m for the north, east and up directions, respectively.

The reason for the lower positioning accuracy of the long baseline compared to the short baseline is the fact that errors, such as the tropospheric delay, cannot be eliminated in long baselines. Thus, to improve the accuracy and reliability of the GNSS kinematic positioning in large regions, a multiple reference stations approach should be taken into account.

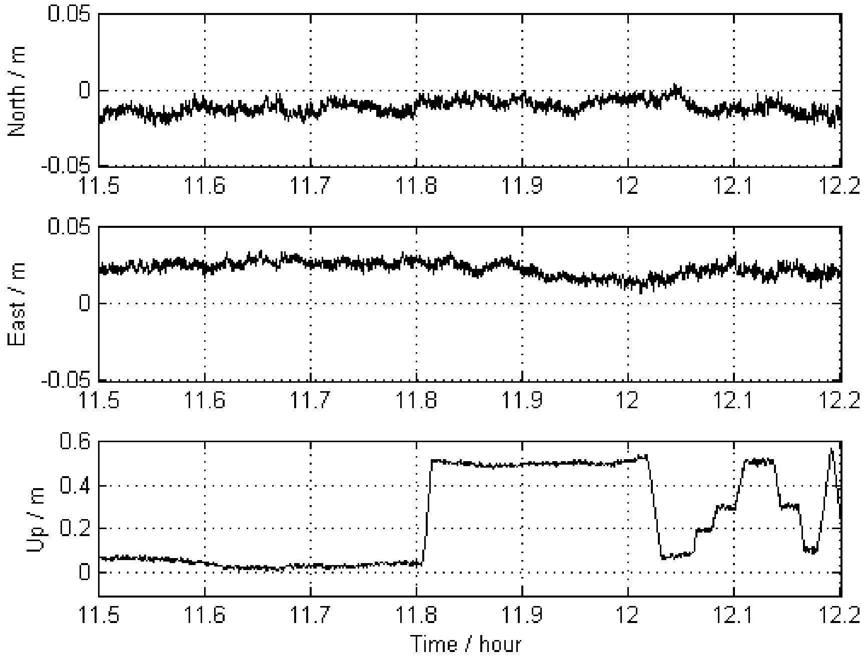

Figure 4.4: The results of the kinematic positioning for the long baseline MATE-KIN1 during the vertical antenna movement experiment

Table 4.1: The statistical results of the difference between the long and the short baseline (Unit: m)

Direction	**Min**	**Max**	**Mean**	**RMS**
North	-0.026	0.004	-0.012	0.012
East	0.009	0.034	0.022	0.022
Up	0.011	0.130	0.062	0.068

4.3 Multiple Reference Stations Kinematic Positioning Based on an A priori Constraint

The use of a single baseline for kinematic GNSS positioning can provide high positioning accuracies in small areas. But for the ultra-long-range kinematic positioning, the use of multiple reference stations should be considered (Dai et al., 2001; Lachapelle and Alves, 2009; Wang et al., 2011; Al-Shaery et al., 2011; Firuzabadì and King, 2012).

Compared to the single baseline users, one of most important advantages of multiple reference stations is the increase in reliability and availability. If one or two reference stations fail at the same time, their missed contributions can be substituted by the remaining reference stations, thus the availability of the service is retained (Fotopoulos and Cannon, 2001). Another quite important aspect is that it allows to model distance-dependent or spatially correlated errors, such as satellite orbit, tropospheric and ionospheric effects. This effect of distance-dependent errors can be reduced by combining observations from the multiple reference stations (Fotopoulos and Cannon, 2001).

4.3.1 Principle of Multiple Reference Stations Kinematic Positioning Based on an A priori Constraint

Airborne gravimetric projects, such as the GEOHALO project, are usually carried out over large areas, thus a dedicated approach of the Kalman filtering in kinematic GNSS positioning based on an a priori constraint for multiple reference stations was developed as described in this section to improve the accuracy and reliability of the kinematic GNSS positioning. The idea is the following: When the DD observation equations are formed, there is just only one station which is used as a formal reference station. The other reference stations are processed formally as kinematic stations together with the real kinematic stations. But in contrast to the real kinematic stations an a priori constraint based on the known station information is applied to the other reference stations. If they do not have those constraints, they would be real kinematic stations.

In the Kalman filter DD positioning of a single baseline between the kinematic station k and the first reference station r_1, the system state equation Eq. (3.28) and observation equation Eq. (3.29) can be re-written as

$$X_i^k = \Phi_{i,i-1}^k X_{i-1}^k + W_i^k \tag{4.8}$$

and

$$L_i^k = A_i^k X_i^k + e_i^k , \tag{4.9}$$

where the subscript i refers to the time epoch t_i. The superscript k denotes the kinematic station. X_i^k and X_{i-1}^k are $m \times 1$ unknown parameter vectors at time t_i and t_{i-1}, respectively, where the state vector of the kinematic station $\left[x_i, y_i, z_i\right]^{\mathrm{T}}$ or is included $\left[x_i, y_i, z_i, \dot{x}_i, \dot{y}_i, \dot{z}_i\right]^{\mathrm{T}}$. T is the tropospheric zenith wet delay. $X_i = [x_i, y_i, z_i, T_i^{r_1}, T_i^k, \nabla\Delta N_1, \nabla\Delta N_2, \ldots, \nabla\Delta N_n]^{\mathrm{T}}$ where $\left[\nabla\Delta N_1, \nabla\Delta N_2, \ldots, \nabla\Delta N_n\right]^{\mathrm{T}}$ are the DD ambiguity parameters. The subscript n is the number of DD observations. $\Phi_{i,i-1}^k$ is the $m \times m$ transition matrix from the time t_{i-1} to t_i, W_i^k is the $m \times 1$ error vector of the system state model with zero mean and the covariance matrix $\Sigma_{W_i^k}$. L_i^k is the $n \times 1$ DD measurement vector at the time epoch t_i. A_i^k is the $n \times m$

design matrix and e_i^k is the DD measurement error vector with zero mean and covariance matrix Σ_i^k.

When multiple kinematic stations are adopted, the system state equation and the observation equation of the Kalman filter DD positioning can be written as

$$\begin{bmatrix} X_i^{k_1} \\ X_i^{k_2} \\ \vdots \\ X_i^{k_j} \end{bmatrix} = \begin{bmatrix} \Phi_{i,i-1}^{k_1} & & & \\ & \Phi_{i,i-1}^{k_2} & & \\ & & \ddots & \\ & & & \Phi_{i,i-1}^{k_j} \end{bmatrix} \cdot \begin{bmatrix} X_{i-1}^{k_1} \\ X_{i-1}^{k_2} \\ \vdots \\ X_{i-1}^{k_j} \end{bmatrix} + \begin{bmatrix} W_i^{k_1} \\ W_i^{k_2} \\ \vdots \\ W_i^{k_j} \end{bmatrix} \tag{4.10}$$

and

$$\begin{bmatrix} L_i^{k_1} \\ L_i^{k_2} \\ \vdots \\ L_i^{k_j} \end{bmatrix} = \begin{bmatrix} A_i^{k_1} & & & \\ & A_i^{k_2} & & \\ & & \ddots & \\ & & & A_i^{k_j} \end{bmatrix} \cdot \begin{bmatrix} X_i^{k_1} \\ X_i^{k_2} \\ \vdots \\ X_i^{k_j} \end{bmatrix} + \begin{bmatrix} e_i^{k_1} \\ e_i^{k_2} \\ \vdots \\ e_i^{k_j} \end{bmatrix}, \tag{4.11}$$

where the subscript j is the number of kinematic stations. These DD observations are formed w.r.t. the first reference station r_1 for each of the kinematic stations $k_1, k_2, \dots, k_j$ respectively. The non-diagonal block matrixes of the design matrix A_i of Eq. (4.11) are zero.

When the multiple reference station method including the a priori constraint is applied, the additional reference stations are processed as kinematic station. This is similar to Eq. (4.10) and Eq. (4.11). The system state equations and the observation equations of the Kalman filter DD positioning can be written as

$$\begin{bmatrix} X_i^{r_2} \\ \vdots \\ X_i^{r_s} \\ X_i^{k} \end{bmatrix} = \begin{bmatrix} \Phi_{i,i-1}^{r_1} & & & \\ & \ddots & & \\ & & \Phi_{i,i-1}^{r_s} & \\ & & & \Phi_{i,i-1}^{k} \end{bmatrix} \cdot \begin{bmatrix} X_{i-1}^{r_2} \\ \vdots \\ X_{i-1}^{r_s} \\ X_{i-1}^{k} \end{bmatrix} + \begin{bmatrix} W_i^{r_2} \\ \vdots \\ W_i^{r_s} \\ W_i^{k} \end{bmatrix} \tag{4.12}$$

and

$$\begin{bmatrix} L_i^{r_2} \\ \vdots \\ L_i^{r_s} \\ L_i^{k} \end{bmatrix} = \begin{bmatrix} A_i^{r_2} & \dots & A_i^{r_2,r_s} & A_i^{r_2,k} \\ \vdots & \ddots & \vdots & \vdots \\ A_i^{r_s,r_2} & \dots & A_i^{r_s} & A_i^{r_s,k} \\ A_i^{k,r_2} & \dots & A_i^{k,r_s} & A_i^{k} \end{bmatrix} \cdot \begin{bmatrix} X_i^{r_2} \\ \vdots \\ X_i^{r_s} \\ X_i^{k} \end{bmatrix} + \begin{bmatrix} e_i^{r_2} \\ \vdots \\ e_i^{k_s} \\ e_i^{k} \end{bmatrix}, \tag{4.13}$$

where s is the number of the multiple reference stations, $r_2, r_3, \dots, r_s$ are the additional reference stations and k is the kinematic station. If these DD observations are formed w.r.t. the first reference station r_1 with each other station including the additional reference stations and the kinematic stations $r_2, r_3, \ldots, r_s, k$, respectively, the non-diagonal block matrixes of the design matrix A_i of Eq. (4.13) are zeros. If the DD observations are formed between the additional reference stations $r_2, r_3, \ldots, r_s$ and the kinematic station k, the non-diagonal block matrixes of the design matrix A_i of Eq. (4.13) is the design matrix of the corresponding observations.

The calculation for the additional reference stations $r_2, r_3, \ldots, r_s$ is similar as for the kinematic station k. But a kind of strong a priori constraint for the state vector is applied for the additional reference stations according to their known state information, such as $(x_0^{r_2}, y_0^{r_2}, z_0^{r_2})$ or $(x_0^{r_2}, y_0^{r_2}, z_0^{r_2}, \dot{x}_0^{r_2}, \dot{y}_0^{r_2}, \dot{z}_0^{r_2})$. Thus, a kind of highly precise a priori accuracy for the state vector and a small enough spectral densities for the Kalman filter are applied to the state vector during the Kalman filter processing. For example, the elements of a priori variance and the spectral densities of the position vector are set to $1\times10^{-6}\ \mathrm{m}^2$ and $1\times10^{-9}\ \mathrm{m}^2/\mathrm{s}$, respectively. This condition guarantees that the state vectors of the additional reference stations are not modified during the Kalman filter processing.

And then, the estimates for the kinematic station can be obtained according to the theory of the two-way Kalman filtering discussed in Section 3.3. This new approach is more flexible when running the software programs since one only needs to fix those kinematic stations which shall serve as reference stations.

4.3.2 Experiment and Analysis

In order to investigate the capability of the new approach based on multiple reference stations, highly dynamic and ultra-long-range GNSS observation data were taken from the GEOHALO project. The GNSS data were collected by GFZ on June 08. 2012 and comprise GPS and GLONASS observations. The GNSS antennas of the kinematic stations AIR5 and AIR6 were selected. These antennas were mounted on the HALO aircraft in its front and middle part, respectively (cf. Figure 4.5). The reference station REF6 was set up by GFZ beside the runway of the DLR airport Oberpfaffenhofen in Germany. The reference stations RENO and ASCE were located in central Italy and have been chosen as multiple reference stations. The types of all these receivers and antennas are given in Table 4.2.

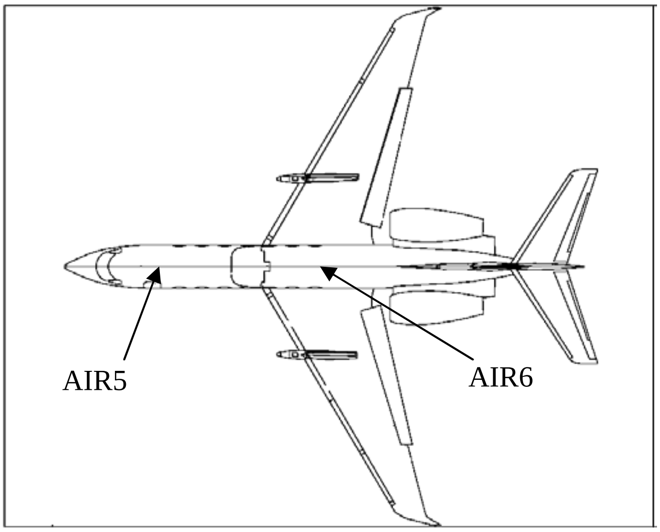

Figure 4.5: The positions of the selected GNSS antennas on the HALO aircraft

Table 4.2: Hardware list of the selected stations from the GEOHALO project

Station Name	Receiver type	Antenna type	(with dome)
AIR5	JAVAD TRE_G3TH DELTA	ACCG5ANT_42AT1	NONE
AIR6	JAVAD TRE_G3TH DELTA	ACCG5ANT_42AT1	NONE
REF6	JAVAD TRE_G3TH DELTA	JAV_RINGANT_G3T	NONE
RENO	TPS ODYSSEY_E	TPSCR3_GGD	CONE
ASCE	LEICA GRX1200+	LEIAR25	NONE

The trajectory of the HALO aircraft on June 08, 2012 and the position of the selected multiple reference stations REF6, RENO and ASCE are shown in Figure 4.6.

In order to investigate the accuracy and reliability of the algorithm as described above, firstly, the trajectories of the kinematic stations AIR5 and AIR6 were calculated separately. Then a time series of the baseline length between the two antennas of the kinematic stations AIR5 and AIR6 was calculated from the estimated trajectories. The precision and reliability of the kinematic results were analyzed by checking the temporal variations of the baseline length. For this reason, the following two computation schemes were performed and compared.

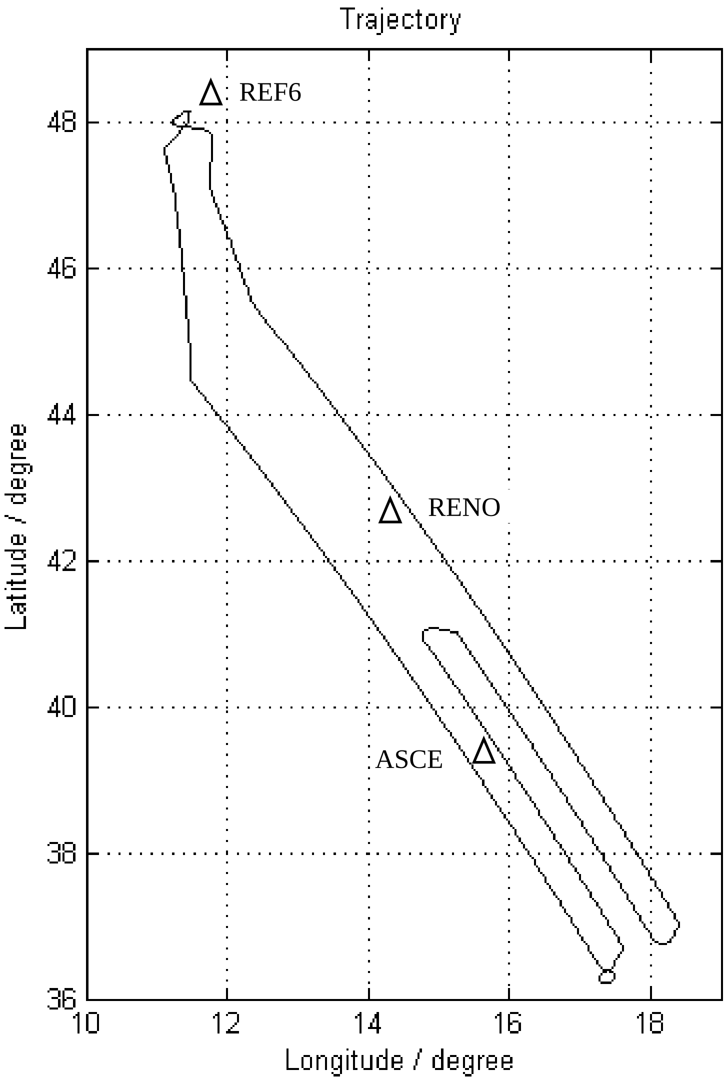

Figure 4.6: HALO aircraft flight trajectory and the position of reference stations

Scheme 1 (single baseline experiment): The GPS and GLONASS measurement data were used for the calculation of the trajectories for the kinematic stations AIR5 and AIR6 with REF6 as the only reference station. Then the distance between AIR5 and AIR6 was calculated.

Scheme 2 (multiple reference stations experiment): The GPS and GLONASS data were used for the calculation of the trajectories for the kinematic stations AIR5 and AIR6 by the new approach where REF6, RENO and ASCE served as multiple reference stations. Then the distance between AIR5 and AIR6 was calculated.

In the data processing for the mentioned calculations, the DD processing of the multiple reference stations kinematic positioning based on an a priori constraint was carried out using the HALO_GNSS software, which was developed by the author of this thesis for the GEO-HALO project. Here, the dual-frequency carrier phase observations were used to form the ionosphere-free linear combination. The tropospheric zenith wet delay was estimated as well and an uncertainty of 10 cm and a spectral density of $10^{-8}\ \mathrm{m}^2/\mathrm{s}$ for the kinematic stations were assumed. The two-way Kalman filter was used for the parameter estimation.

The results of scheme 1 and scheme 2 are given in Figure 4.7 and Figure 4.8, respectively. The statistical results of the two schemes are given in Table 4.3.

Table 4.3: The Statistical results for the distance between the two antennas AIR5 and AIR6 (Unit: m)

Reference stations	Min	Max	Mean	SDev
REF6	6.892	7.179	7.046	0.039
REF6, RENO, ASCE	6.984	7.141	7.042	0.019

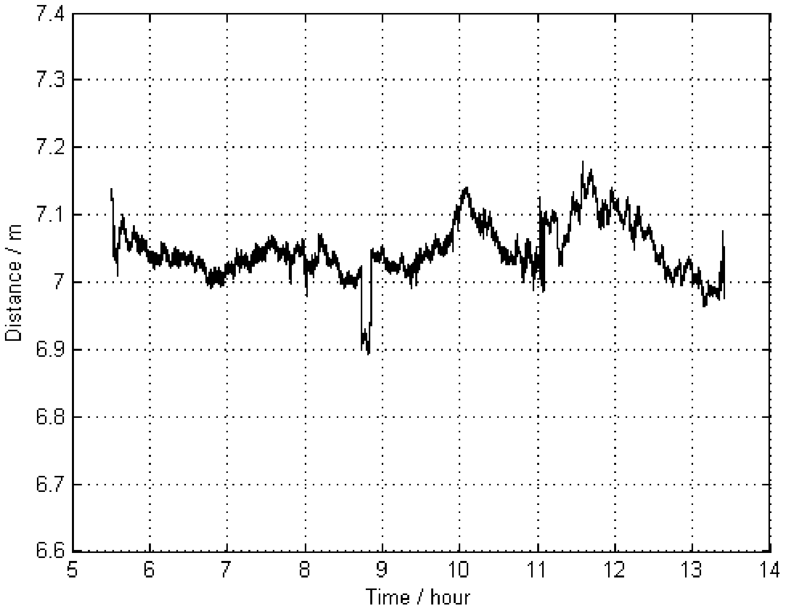

Figure 4.7: The distance between the two antennas AIR5 and AIR6, the trajectories for these antennas were estimated by using only one reference station (REF6)

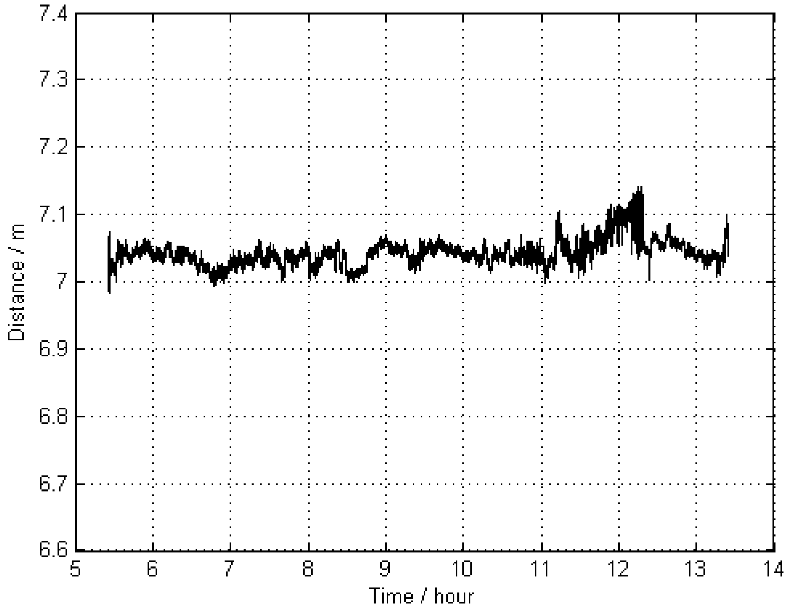

Figure 4.8: The distance between the two antennas AIR5 and AIR6, the trajectories for these antennas were estimated including the three reference stations REF6, RENO and ASCE

Figure 4.7, Figure 4.8 and Table 4.3 show clearly that the GNSS kinematic positioning is significantly improved for a large region when using the approach of multiple reference stations.

The reason for this improvement is the reduction of distance-dependent errors, such as satellite orbit, tropospheric and ionospheric effects when applying the principle of multiple reference stations.

4.4 Kinematic Positioning Based on Robust Estimation

In GNSS kinematic precise positioning, observation outliers can affect the accuracy and the reliability of results. In airborne gravimetry, the requirements on the accuracy and the reliability of the results are higher than in “usual” geometric GNSS applications. Thus, outliers should be eliminated. One method for outlier elimination is Baarda’s data snooping (Baarda, 1968). It is based on testing the occurrence of individual residuals under the assumption that only lone outliers are present in the relevant set of observations (Leick, 2004, p.173). However, such an approach is complicated to apply, if multitudinous outliers are expected. In GNSS kinematic precise positioning, it is often the case that not only individual outliers occur in the observations, and is not a good idea to eliminate each observation featuring a small outlier since this could cause too few remaining GNSS observations in certain epochs. In this context, to minimize the impact of observation outliers on the estimates, a robust estimation approach is applied by using all observations including the outliers but reducing the weights of the observations individually according to the outlier magnitude. This approach keeps the estimation algorithm stable and can reduce the impact of the outliers when more than one outlier per GNSS observations epoch exists.

4.4.1 Principle of Robust Kalman Filter

Robust estimation has been widely studied and applied in geodesy (Koch and Yang, 1998; Yang et al., 1999; Yang et al., 2001; Yang et al., 2010; Koch, 2013). For example, a Danish method (Kubik, 1982), and an IGG-I scheme (Zhou, 1989) for different weighting of observations were established. An IGG-III scheme (Yang, 1994) was proposed for the estimation of dependent observations.

Based on the classical Kalman filter (cf. Section 3.3), if searching for outliers in the GNSS observations is included, the robust Kalman filter estimation could be described as (Yang et al., 2001)

$$\hat{X}_i = \bar{X}_i + \bar{K}_i \left(L_i - A_i \bar{X}_i \right) \tag{4.14}$$

and

$$\bar{K}_i = \Sigma_{\bar{X}_i} A_i^{\mathrm{T}} \left(A_i \Sigma_{\bar{X}_i} A_i^{\mathrm{T}} + \bar{\Sigma}_i \right)^{-1}, \tag{4.15}$$

where $\bar{K}_i$ denotes the Kalman gain matrix based on the equivalent weight matrix of observations L_i at epoch i. $\bar{\Sigma}_i$ is the covariance matrix of the equivalent weight matrix of the observations L_i with

$$\bar{\Sigma}_i = \sigma_0^2 \bar{P}_i^{-1}, \tag{4.16}$$

where σ_0^2 is the variance of unit weight. $\bar{P}_i$ denotes the equivalent weight matrix of observations L_i. In the independent case, $\bar{P}_i$ is a diagonal matrix with the elements $\bar{p}_i^k$ with

$$\bar{p}_i^k = c_i^k p_i^k, \tag{4.17}$$

where $k = 1, 2, \ldots, n$, n is the number of DD observations, p_i^k is the element of the original weight matrix P_i at the observation at epoch i and c_i^k denotes the weight factor of the robust estimation (Yang, 1991; Yang et al., 1999). Based on the calculation experiments, the c_i^k can be constructed for three different cases as follows

$$c_i^k = \begin{cases} 1 & \left|\overline{v}_i^k\right| \le t_1 \\ \dfrac{t_1}{\left|\overline{v}_i^k\right|}\left(\dfrac{t_2 - \left|\overline{v}_i^k\right|}{t_2 - t_1}\right) & t_1 < \left|\overline{v}_i^k\right| < t_2 \,, \\ 0 & \left|\overline{v}_i^k\right| \ge t_2 \end{cases} \tag{4.18}$$

where t_1 and t_2 are two constants with the empirically found values $t_1 = 1.0 \sim 1.5$ and $t_2 = 3.5 \sim 6.5$, respectively. $\overline{v}_i^k$ is the standard residual with

$$\overline{v}_i^k = \frac{v_i^k}{\sigma_i}\,, \tag{4.19}$$

where v_i^k denotes the element of the residual matrix V_i (V_i can be found in Eq. (3.33)), σ_i^2 are the robust variances of the observations (Yang et al., 1999).

The weight factor c_i^k of Eq. (4.18) depending on the standard residual $\overline{v}_i^k$ is given in Figure 4.9. In this figure, the middle segment in the weight factor function given by Eq. (4.18) is the same as that of the LS case. In practice, most residuals of the GNSS observations will satisfy the condition $\left|\overline{v}_i^k\right| \le t_1$, and then $c_i^k = 1$, which is just the result of a LS estimation. Both side parts of the weight factor function are down-weighting parts, which smooth the weight factor from the LS case to a rejection point. The contribution of the corresponding measurements to the state parameter estimations will be reduced, which should make the Kalman filter more robust.

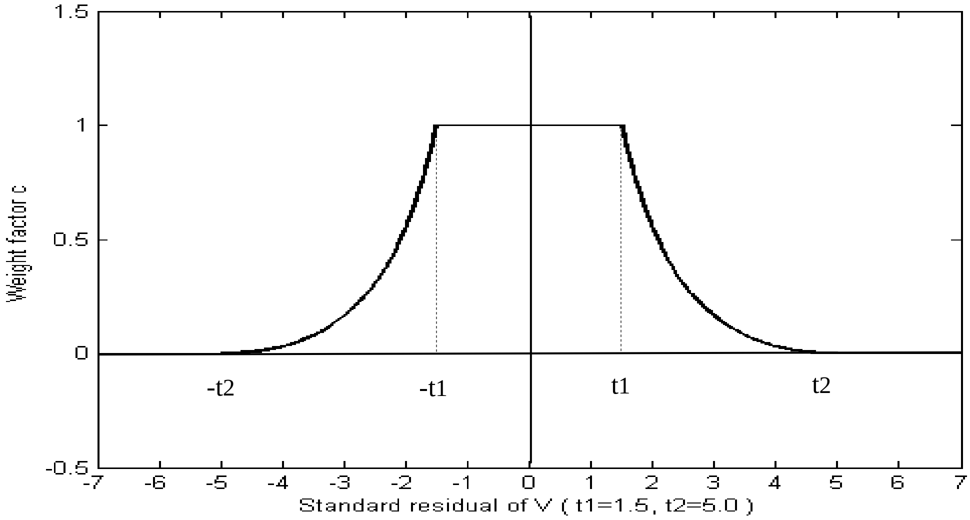

Figure 4.9: The weight factors of Kalman filter robust estimation

The robust estimation theory can be used in airborne gravimetry to control the impact of GNSS observation outliers on the estimates for the kinematic platform. In the work for this thesis the experiment as described in the following section has been carried out.

4.4.2 Experiment and Analysis

Here an experiment study has been performed using the same GNSS data as in the experiment described in Section 4.3.2. The multiple reference stations REF6, RENO and ASCE, as shown in Figure 4.6, were used to calculate the trajectories of the kinematic stations AIR5 and AIR6. The hardware types of the GNSS receivers and antennas have been listed in Table 4.2.

Two kinematic experiments have been carried out in order to show the performance of the robust estimation. To investigate the accuracy and reliability of the algorithm in this experiment, the trajectories of the kinematic stations AIR5 and AIR6 were estimated separately. Afterwards, a time series of the baseline length between these two antennas was calculated. The accuracy and reliability of the kinematic results were analyzed by checking the temporal variations of the baseline length.

4.4.2.1 GNSS Pseudorange observations Experiment

The GNSS pseudorange observations were used to calculate an initial trajectory for the kinematic stations AIR5 and AIR6. The results for the baseline length between AIR5 and AIR6 based on the calculation without using the robust estimation are given in Figure 4.10. This figure shows large spikes in the time series of the baseline length. This is caused by the fact that outliers in the GNSS observations were included when applying the non-robust estimation. The results of the baseline length from with robust estimation are given in Figure 4.11. It shows that now the large spikes have been removed by the robust estimation.

The statistical results of the GNSS pseudorange positioning without and with robust estimation are listed in Table 4.4.

Table 4.4: The statistical results of the baseline length between AIR5 and AIR6 from GNSS pseudorange positioning (Unit: m)

Estimation type	Min	Max	Mean	SDev
Non-robust estimation	3.506	84.400	7.289	1.154
Robust estimation	2.827	12.770	7.298	0.960

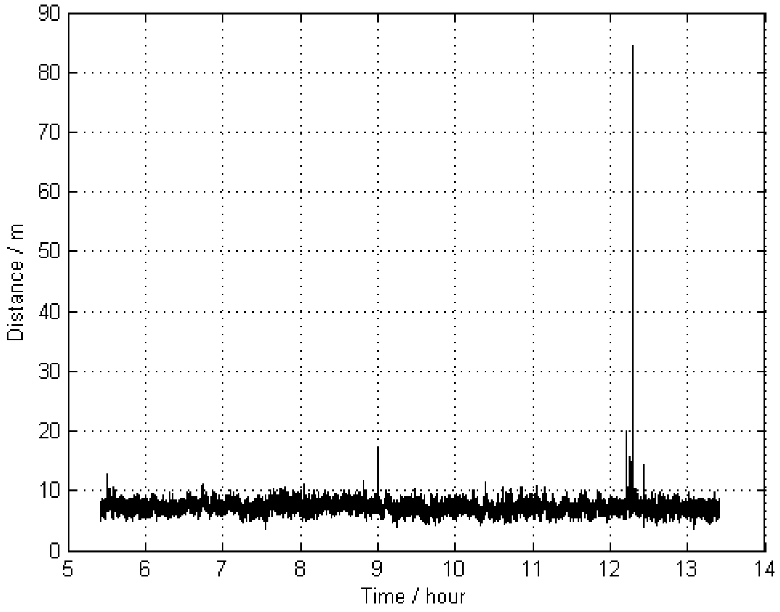

Figure 4.10: The time series for the baseline length between AIR5 and AIR6 based on pseudorange positioning results without robust estimation

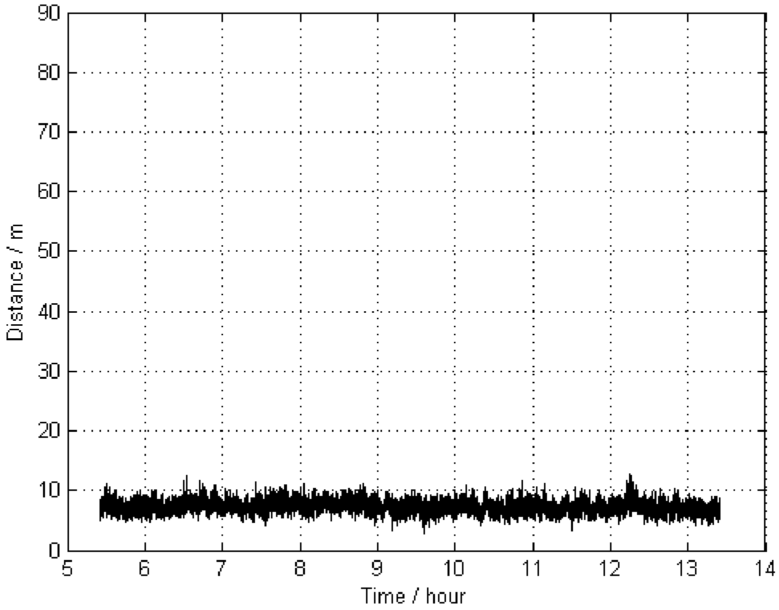

Figure 4.11: The time series for the baseline length between AIR5 and AIR6 based on pseudorange positioning results with robust estimation

Prior to the application of the robust estimation, the probability distribution of the standard residuals for the GNSS pseudorange observations was calculated as shown in Figure 4.12. When the robust estimation was applied by using the constants $t_1 = 1.5$ and $t_2 = 6.0$ (cf. Eq. (4.18)), 87.13% of the pseudorange observations were processed with the same weight as for the LS case, 12.50% of observations were processed by down-weighting w.r.t. the LS case according to Figure 4.9, and 0.37% of the observations (i.e. outliers) were processed with zero weight. That means outliers can be removed by the application of the robust estimation.

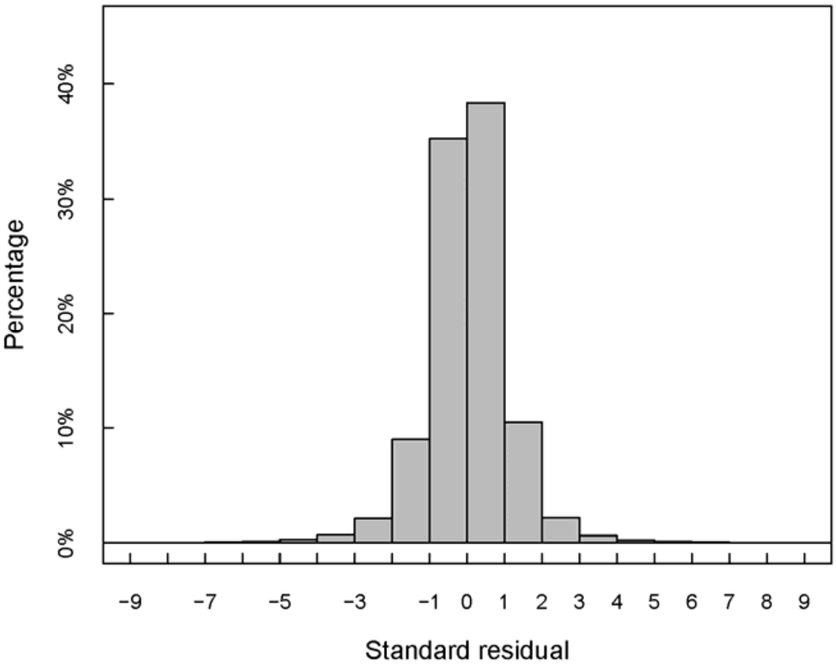

Figure 4.12: The probability distribution of standard residual for the GNSS pseudorange observations

The improvement due to the robust estimation in this experiment can be analyzed by using Baarda's reliability theory (Baarda, 1968; Baarda, 1976) (cf. Section 3.4.3). In order to typically illustrate exemplarily the typical improvement when applying the robust estimation, the GNSS observation at the time epoch 12h:10m:09s are taken to consider the extremely largest spike (84.40 m) as visible in Figure 4.10. For this epoch, the redundancy number r_i, the controllability factors $\delta'_{0,i}$ for the internal reliability, the sensitivity factors $\overline{\delta}_{0,i}$ for the external reliability and the residuals of the GNSS observations were calculated yielding the values given in Table 4.5 and Table 4.6 obtained without and with applying the robust estimation, respectively. Here, for the application of Baarda's theory the significance number $\alpha_0 = 0.1\%$ and the power $\beta_0 = 80\%$ were used. Therefore, the lower bound features $\delta_0 = 4.13$ (Baarda, 1976; Förstner, 1987).

The residuals of the GNSS pseudorange observations in Table 4.6, exhibit two significant outliers with the 9th observation of GPS and the 15th observation of GLONASS. These outliers affect the result of the GNSS positioning (cf. Figure 4.10) and the distribution of the residuals of the GNSS observations (cf. Table 4.5). The reason of this impact is plausibly explained by Baarda's reliability theory (Baarda, 1968):

Without robust estimation, the outlier of the 9th GPS observation is of about 5.193 times its standard deviation. That means, it cannot be detected by Baarda's data snooping (Baarda, 1968) with a probability greater than $\beta_0 = 80\%$ if a significance level of $1-\alpha_0 = 99.9\%$ is accepted for the test with statistic standard residual. Meanwhile, the effect of the undetected outlier on the estimated shift is less than 3.148 times its standard deviation.

Table 4.5: The statistical results for the reliability analysis without robust estimation
(for the GNSS DD observations at time epoch 12h:10m:09s)

GNSS DD observations		**The redundancy number** r_i	**The controllability factors** $\delta'_{0,i}$	**The sensitivity factors** $\bar{\delta}_{0,i}$	**The residuals of GNSS obs.** $\hat{V}$ **(Unit: m)**
GPS	1	0.896	4.363	1.408	36.687
	2	0.859	4.457	1.676	22.055
	3	0.808	4.595	2.015	4.636
	4	0.783	4.666	2.172	41.432
	5	0.957	4.222	0.877	17.105
	6	0.899	4.356	1.384	-35.324
	7	0.538	5.632	3.830	-15.863
	8	0.851	4.478	1.730	-9.445
	9	**0.632**	**5.193**	**3.148**	**126.008**
GLONASS	10	0.940	4.260	1.043	-34.554
	11	0.806	4.599	2.024	-6.285
	12	0.913	4.432	1.276	-32.567
	13	0.875	4.416	1.563	12.765
	14	0.757	4.746	2.339	-19.413
	15	**0.763**	**4.729**	**2.303**	**-25.594**
	16	0.815	4.573	1.964	-16.676
	17	0.799	4.621	2.072	-6.355

When the robust estimation is applied, the design matrix *A* (cf. Eq. (3.47)) is not changed since the observation environment or condition are not modified, but the weights of the observations *P* are adjusted. The outlier of 9th GPS observation, which is 4.130 times larger than its standard deviation can be detected by Baarda's data snooping, with a probability higher than $\beta_0 = 80\%$ if a significance level is $1-\alpha_0 = 99.9\%$ for the test with test statistic standard residual is used. The important improvement is that the effect of the outlier is removed due to the sensitivity factor $\overline{\delta}_{0,i}$ being zero. In general, very small sensitivity values $\overline{\delta}_{0,i}$ suggest checking whether the observation is really necessary, or whether it is superfluous (Förstner, 1987). Therefore, the zero weight is given by robust estimation to the 9th GPS observation.

Table 4.6: The statistical results for the reliability analysis when applying robust estimation (for the GNSS DD observations at time epoch 12:10:09)

GNSS DD observations		**The redundancy number** r_i	**The controllability factors** $\delta'_{0,i}$	**The sensitivity factors** $\overline{\delta}_{0,i}$	**The residuals of GNSS obs.** $\hat{V}$ **(Unit: m)**
GPS	1	0.853	4.472	1.714	2.630
	2	0.841	4.503	1.795	1.013
	3	0.799	4.620	2.070	-0.427
	4	0.702	4.930	2.693	0.522
	5	0.963	4.208	0.807	0.548
	6	0.902	4.349	1.362	-5.737
	7	0.480	5.964	4.302	1.340
	8	0.831	4.531	1.864	-2.221
	9	**1.000**	**4.130**	**0.000**	**187.438**
GLONASS	10	0.880	4.402	1.523	-4.640
	11	0.798	4.623	2.077	-6.059
	12	0.851	4.478	1.731	-1.924
	13	0.794	4.635	2.104	-3.000
	14	0.706	4.916	2.666	-2.195
	15	**0.889**	**4.380**	**1.460**	**-10.555**
	16	0.808	4.595	2.015	-2.125
	17	0.795	4.632	2.098	-0.339

The improvement of the reliability can be seen for the 15th observation of GLONASS as well. The controllability factor of the internal reliability $\delta'_{0,i}$ is improved from 4.729 to 4.380. This means that the gross error can be detected from 4.729 times improved to 4.380 times its standard deviation. The sensitivity factors of the external reliability $\overline{\delta}_{0,i}$ are improved from 2.303 to 1.460. This means that the effect of undetected errors in the 15th observation onto the result can be reduced from 2.303 times down to 1.460 times its standard deviation. Others residual of Table 4.6 have the same noise level as the GNSS pseudorange observations, thus they do not need to be analyzed.

Hence, the robust estimation can improve the reliability in GNSS kinematic positioning as shown here exemplary for the selected time epoch.

4.4.2.2 GNSS Carrier Phase Observations Experiment

The GNSS carrier phase observations were taken to estimate final precise trajectories for the kinematic stations AIR5 and AIR6. The results for the time series of the baseline length between both antennas without and with robust estimation are given in Figure 4.13 and Figure 4.14, respectively. The corresponding statistical results are listed in Table 4.7. The numbers in this table as well as the plots in both figures show very clearly that the accuracy of the results from the carrier phase precise positioning based on the classic Kalman filter based on multiple reference stations is improved by robust estimation.

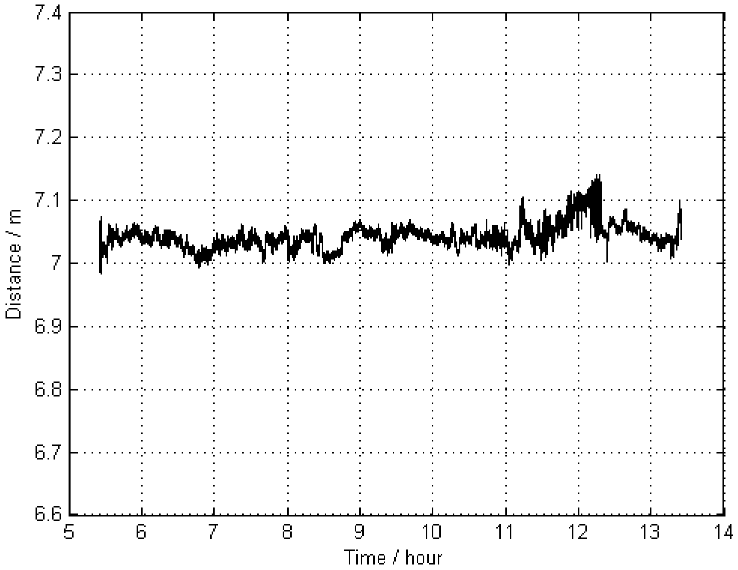

Figure 4.13: The time series for the baseline length between AIR5 and AIR6 based on carrier phase positioning results without robust estimation

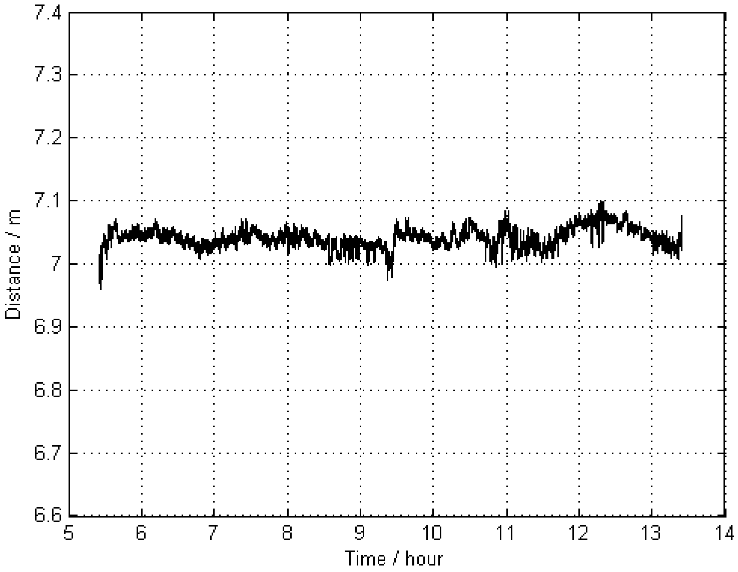

Figure 4.14: The time series for the baseline length between AIR5 and AIR6 based on carrier phase positioning results with robust estimation

Table 4.7: The statistical results of GNSS carrier phase positioning (Unit: m)

Estimation type	Min	Max	Mean	SDev
Non-robust estimation	6.984	7.142	7.043	0.019
Robust estimation	6.959	7.101	7.041	0.016

Prior to the application of the robust estimation, the probability distribution of the standard residuals for the GNSS carrier phase observations was calculated as shown in Figure 4.15. When the robust estimation was applied by using the constants $t_1 = 1.5$ and $t_2 = 6.0$ in Eq. (4.18), 86.50% of carrier phase observations were processed with the same weight as for the LS case, 12.88% of the carrier phase observations were down-weighted w.r.t. the LS case according to Figure 4.9, and 0.62% of observations (i.e. outliers) were processed with zero weight. That means outliers can be removed by the application of the robust estimation.

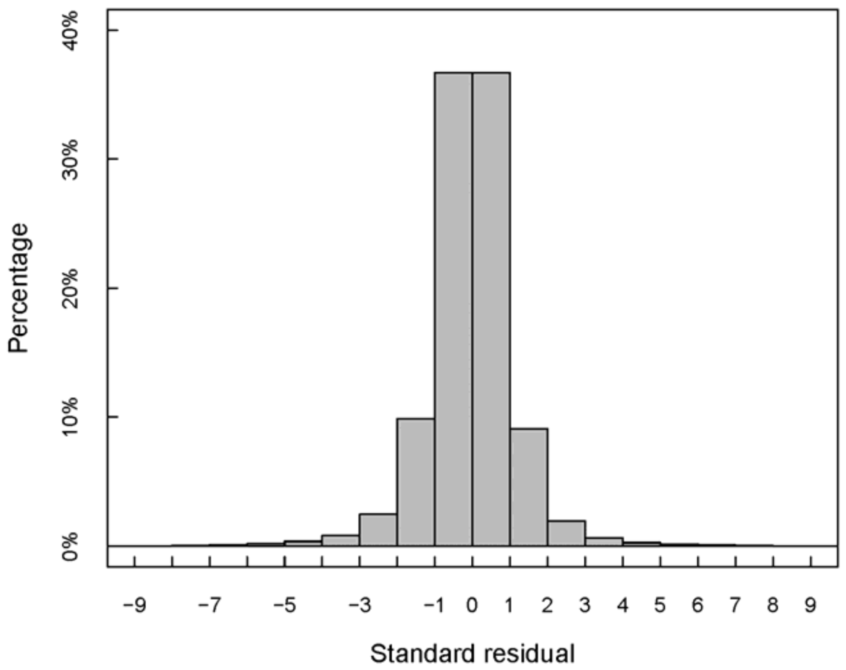

Figure 4.15: The probability distribution of the standard residuals for the GNSS Carrier phase observations

The aforementioned results show the following: If the GNSS observations have larger outliers, their impact on the errors of the non-robust Kalman filter results (cf. Figure 4.10 and Figure 4.13) is more significant for the pseudorange positioning than for the carrier phase positioning. This has the following reason: cycle slips of the carrier phase data will be introduced whenever outliers occur in the GNSS carrier phase observations. Then, the new carrier phase ambiguity is applied for the subsequent GNSS carrier phase observations. The other reason is that the initial position calculated from the pseudoranges is used to form the design matrix of the carrier phase equation, such as Eq. (4.9) and the final precise results were calculated from the carrier phase observations.

But larger outliers still have an impact on the results of the carrier phase processing as shown in Figure 4.13. This should be taken into account in highly precise positioning. Thus the robust estimation is applied for airborne gravimetry. The impact of outliers in the GNSS measurements is suppressed by the equivalent weights in the robust estimation. This can be seen from the comparison with Figure 4.14 and from the statistical results in Table 4.7. That means the robust estimation should be the preferred estimation approach for precise GNSS positioning.

4.5 Conclusions

In this Chapter 4, the observation equations of single difference (SD) and DD are described. It is shown in the studies of this thesis that the common errors between the satellites and the receivers (such as tropospheric delays, ionospheric delays, GNSS satellite orbit errors and clock errors etc) can be eliminated or reduced by DD positioning for small areas. But for large regions, these errors cannot be eliminated satisfactorily by DD positioning.

For large regions a significant improvement of the accuracy and reliability for GNSS DD positioning can be achieved by using a certain algorithm of multiple reference stations which is based on the application of an a priori constraint. This improvement has been demonstrated during the experiments as described in this chapter.

In addition, a robust Kalman filter approach is used to suppress the impact of observation outliers on the trajectory estimates for airborne gravimetry. It is helpful to apply such a robust estimation in GNSS precise positioning.

5 Kinematic Positioning Based on Multiple Kinematic Stations

5.1 Introduction

In the application of GNSS precise positioning in the airborne gravimetric project GEOHALO or any other kinematic positioning, it is often the case that multiple GNSS receiving equipments are mounted on the kinematic platform, thus known functional or theoretical relations exist among the unknown parameters of the multiple GNSS receiving equipments. For example, the distances among the multiple GNSS antennas are known and fixed and the characteristic of the tropospheric delay in a small area above the HALO aircraft is similar (see Figure 5.1). This known relations and characteristic can be and should be made use of to improve the accuracy and reliability of the state estimates and to control the divergences.

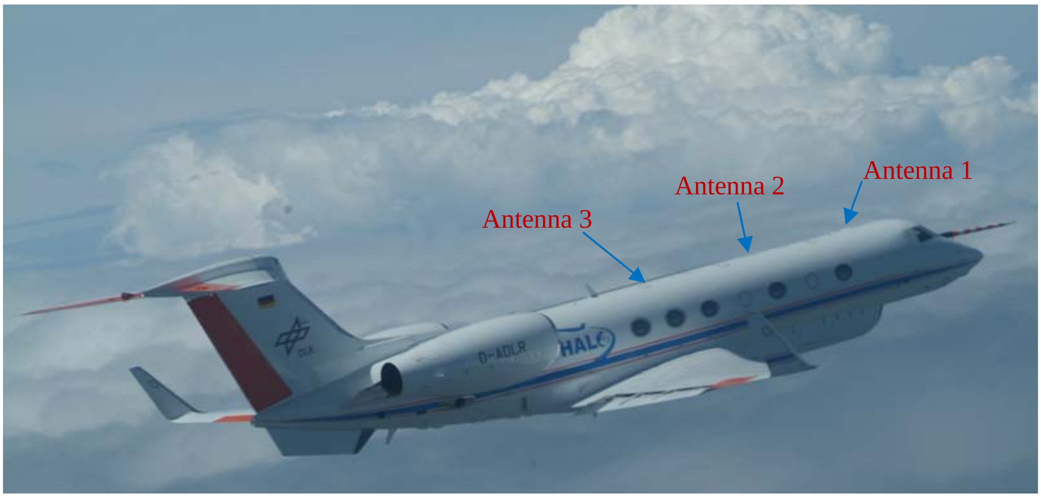

Figure 5.1: Multiple GNSS antennas mounted on the HALO aircraft (DLR, 2013a)

For this purpose, in this chapter, a method of GNSS kinematic positioning based on multiple kinematic stations with multiple reference stations is developed firstly. And then the distances among the multiple GNSS antennas are used as constraints within the state parameters. Finally, a common tropospheric zenith delay parameter is used for the multiple kinematic stations, which depends on the similar characteristic of tropospheric effects.

5.2 Kinematic Positioning Based on Multiple Kinematic Stations with Multiple Reference Stations

Following the kinematic positioning based on multiple reference stations (cf. Section 4.3), the Kalman filter system state equation and observation equation of the kinematic positioning based on multiple kinematic stations with multiple reference stations can be given as

$$\begin{bmatrix} X_i^{r_2} \\ \vdots \\ X_i^{r_s} \\ X_i^{k_1} \\ \vdots \\ X_i^{k_j} \end{bmatrix} = \begin{bmatrix} \Phi_{i,i-1}^{r_1} & & & & & \\ & \ddots & & & & \\ & & \Phi_{i,i-1}^{r_s} & & & \\ & & & \Phi_{i,i-1}^{k} & & \\ & & & & \ddots & \\ & & & & & \Phi_{i,i-1}^{k_j} \end{bmatrix} \cdot \begin{bmatrix} X_{i-1}^{r_2} \\ \vdots \\ X_{i-1}^{r_s} \\ X_{i-1}^{k_1} \\ \vdots \\ X_{i-1}^{k_j} \end{bmatrix} + \begin{bmatrix} W_i^{r_2} \\ \vdots \\ W_i^{r_s} \\ W_i^{k_1} \\ \vdots \\ W_i^{k_j} \end{bmatrix} \tag{5.1}$$

and

$$\begin{bmatrix} L_i^{r_2} \\ \vdots \\ L_i^{r_s} \\ L_i^{k_1} \\ \vdots \\ L_i^{k_j} \end{bmatrix} = \begin{bmatrix} A_i^{r_2} & \cdots & A_i^{r_2,r_s} & A_i^{r_2,k_1} & \cdots & A_i^{r_2,k_j} \\ \vdots & \ddots & \vdots & \vdots & \ddots & \vdots \\ A_i^{r_s,r_2} & \cdots & A_i^{r_s} & A_i^{r_s,k_1} & \cdots & A_i^{r_s,k_j} \\ A_i^{k_1,r_2} & \cdots & A_i^{k_1,r_s} & A_i^{k_1} & \cdots & A_i^{k_1,k_j} \\ \vdots & \ddots & \vdots & \vdots & \ddots & \vdots \\ A_i^{k_j,r_2} & \cdots & A_i^{k_j,r_s} & A_i^{k_j,k_1} & \cdots & A_i^{k_j} \end{bmatrix} \cdot \begin{bmatrix} X_i^{r_2} \\ \vdots \\ X_i^{r_s} \\ X_i^{k_1} \\ \vdots \\ X_i^{k_j} \end{bmatrix} + \begin{bmatrix} e_i^{r_2} \\ \vdots \\ e_i^{r_s} \\ e_i^{k_1} \\ \vdots \\ e_i^{k_j} \end{bmatrix}, \tag{5.2}$$

where the subscript i is the epoch time t_i. The superscript r and k denote the reference stations and kinematic stations, respectively. s and j denote the number of reference stations and kinematic stations. X_i and X_{i-1} are unknown parameter vectors at epoch i and $i-1$, respectively, in which including state vector $\left[x_i, y_i, z_i\right]^{\mathrm{T}}$ or $\left[x_i, y_i, z_i, \dot{x}_i, \dot{y}_i, \dot{z}_i\right]^{\mathrm{T}}$, tropospheric zenith wet delay $\left[T_i\right]$, which will be discussed in following section, and DD ambiguity parameters $\left[\nabla\Delta N_1, \nabla\Delta N_2, \ldots, \nabla\Delta N_n\right]^{\mathrm{T}}$, here subscript n is the number of corresponding DD observations, hereby $X_i = [x_i, y_i, z_i, T_i, \nabla\Delta N_1, \nabla\Delta N_2, \ldots, \nabla\Delta N_n]^{\mathrm{T}}$. $\Phi_{i,i-1}$ is the transition matrix from epoch $i-1$ to i and W_i is the error vector of the system state model with zero mean and covariance matrix Σ_{W_i}. L_i is the DD measurement vector of corresponding observations at epoch i. e_i is the DD measurement error vector with zero mean and covariance matrix Σ_i. A_i is the design matrix, if the DD observations are formed by the first reference station r_1 with each station including additional reference stations and kinematic stations

$r_2, r_3, \dots, r_s, k_1, k_2, \dots, k_j$ respectively, the non-diagonal block matrixes of the design matrix of Eq. (5.2) are zeroes. If the DD observations are formed between the additional reference stations $r_2, r_3, \dots, r_s$ and the kinematic stations $k_1, k_2, \dots, k_j$, the non-diagonal block matrixes of design matrix of Eq. (5.2) are the design sub-matrix of the corresponding DD observations.

According to the estimation theory of two-way Kalman filtering, which has been discussed in Section 3.3, the state estimate of multiple kinematic stations can be obtained.

5.3 Kinematic Positioning Based on an A priori Distance Constraint

When opportunities for the application of certain constraints in the GNSS kinematic state parameters of multiple GNSS sensors system are given, they should be taken into account for the improvement of the positioning accuracy and reliability. A typical example for such a constraint option is the known baseline length between two GNSS antennas mounted on the kinematic platform. This distance can be given as

$$d_i^{k_1,k_2} = \sqrt{\left(x_i^{k_1} - x_i^{k_2}\right)^2 + \left(y_i^{k_1} - y_i^{k_2}\right)^2 + \left(z_i^{k_1} - z_i^{k_2}\right)^2}\,, \tag{5.3}$$

where $d_i^{k_1,k_2}$ denotes the distance between the two antennas of the kinematic stations k_1 and k_2, (x_i, y_i, z_i) is the position vector of the respective kinematic station at epoch i.

There exist several approaches to deal with a priori constraints in Kalman filter applications, which includes linearized constraints, nonlinear constraints, time-varying constraints and so on (Tahk and Speyer, 1990; Doran, 1992; Simon and Chia, 2002; Julier and LaViola, 2007; Ko and Bitmead, 2007; Yang et al., 2010; Yang et al., 2011b). In this section, a dedicated kind of a priori distance constraints is applied for the GNSS kinematic positioning.

5.3.1 The A priori Distance Constraints

Due to the presence of the GNSS antenna phase centre offset and its variation (cf. Section 2.4.2) the precise distances between GNSS antennas are difficult to measure in a simple way (for instance by using a ruler). Therefore in this study, the DD processing on ultra-short baselines is applied to measure the distances among GNSS antennas with millimetre accuracy in a small area. These precise distances are used as a priori constraints with realistic accuracies. The way to deal with these constraints is the so-called “pseudo-observation method”, that is to express the constraints as perfect observation equations which strengthen the structure of the measurement space directly (Yang et al., 2010; Yang et al., 2011b).

When multiple kinematic stations are mounted on a kinematic platform, the linearized constraint equations can be written as

$$D = B_i X_i + \varepsilon \,, \tag{5.4}$$

where D denotes the $u \times 1$ distance constraint vector at every epoch. B_i is an $u \times m$ design matrix at epoch i. X_i is the $m \times 1$ unknown parameter vector at epoch i and ε is a distance constraint uncertainty vector with zero mean and covariance matrix Σ_d .

To express the distance constraints among the kinematic antennas as perfect observation equations, the error equation of Eq. (5.4) can be combined with the GNSS observation error equation Eq. (3.33) as

$$\begin{bmatrix} V_i \\ V_i^d \end{bmatrix} = \begin{bmatrix} A_i \\ B_i \end{bmatrix} \hat{X}_i - \begin{bmatrix} L_i \\ D \end{bmatrix}. \tag{5.5}$$

The covariance matrix of Eq. (5.5) can be written as $\begin{bmatrix} \Sigma_i & 0 \\ 0 & \Sigma_d \end{bmatrix}$.

According to the classical Kalman filter theory (Kalman, 1960; Kalman and Bucy, 1961; Huep, 1985), the parameter estimate depending on a priori distance constraints at epoch i can be expressed as (Tahk and Speyer, 1990; Yang et al., 2010)

$$\hat{X}_i = \bar{X}_i + \Sigma_{\bar{X}_i} \begin{bmatrix} A_i^{\mathrm{T}} & B_i^{\mathrm{T}} \end{bmatrix} \cdot \left\{ \begin{bmatrix} A_i \Sigma_{\bar{X}_i} A_i^{\mathrm{T}} & A_i \Sigma_{\bar{X}_i} B_i^{\mathrm{T}} \\ B_i \Sigma_{\bar{X}_i} A_i^{\mathrm{T}} & B_i \Sigma_{\bar{X}_i} B_i^{\mathrm{T}} \end{bmatrix} + \begin{bmatrix} \Sigma_i & 0 \\ 0 & \Sigma_d \end{bmatrix} \right\}^{-1} \cdot \begin{bmatrix} L_i - A_i \bar{X}_i \\ D - B_i \bar{X}_i \end{bmatrix} \tag{5.6}$$

and the a posteriori covariance matrix $\Sigma_{\hat{X}_i}$ can be expressed by

$$\Sigma_{\hat{X}_i} = \Sigma_{\bar{X}_i} - \Sigma_{\bar{X}_i} \begin{bmatrix} A_i^{\mathrm{T}} & B_i^{\mathrm{T}} \end{bmatrix} \cdot \left\{ \begin{bmatrix} A_i \Sigma_{\bar{X}_i} A_i^{\mathrm{T}} & A_i \Sigma_{\bar{X}_i} B_i^{\mathrm{T}} \\ B_i \Sigma_{\bar{X}_i} A_i^{\mathrm{T}} & B_i \Sigma_{\bar{X}_i} B_i^{\mathrm{T}} \end{bmatrix} + \begin{bmatrix} \Sigma_i & 0 \\ 0 & \Sigma_d \end{bmatrix} \right\}^{-1} \cdot \begin{bmatrix} A_i \\ B_i \end{bmatrix} \Sigma_{\bar{X}_i} \,. \tag{5.7}$$

In order to illustrate the performance of the distance constraints in GNSS precise positioning for multiple kinematic stations, a realistic shipborne gravimetric experiment is given in Section 5.5.

5.4 Kinematic Positioning Based on a Common Tropospheric Parameter

The tropospheric delay is an important error source in precise GNSS applications, which has been introduced briefly in Section 2.4.4. Generally, in GNSS data analysis three methods are used to estimate the tropospheric delay.

The first method uses the tropospheric delay model to correct the tropospheric error. This tropospheric model correction method works well for the hydrostatic or dry tropospheric delay correction (Janes et al., 1991) but not for the wet tropospheric delay, since this is difficult to be corrected completely (Mendes and Langley, 1998; Wei and Ge, 1998; Singh et al., 2014).

The second method is DD processing. If the reference station and the kinematic station are closely located to each other, for example less than 10 km on ground, the impact of the tropospheric delay can be considerably reduced, since both tropospheric delays are approximately the same. However, when applying the DD processing in large regions, where the kinematic station is too far away from the reference station (more than a few hundred kilometres) (Shi and Cannon, 1995) or the difference of their elevations is too large (from a few hundred to thousands of metres) (Tiemeyer et al., 1994; Shi and Cannon, 1995), the difference between the atmospheric delays on the kinematic station and on the reference station will cause an increase of this error impact. Thus, in the latter cases it is difficult to eliminate the tropospheric delay completely by the method of DD processing.

Thirdly, after the application of the atmospheric correction model and the DD processing, the remaining residual tropospheric delay can be corrected by estimating a zenith wet tropospheric delay parameter (Singh et al., 2014).

In order to obtain a high positioning accuracy by DD processing in large regions, the residual tropospheric delay error should be eliminated by estimating a wet tropospheric zenith delay parameter.

5.4.1 Tropospheric Delay Estimation

The Slant Total Delay (STD) between satellite and receiver can be written as (Davis et al., 1985; Chen and Herring, 1997)

$$\mathrm{STD} = M_d(e) \cdot \mathrm{ZHD} + M_w(e) \cdot \mathrm{ZWD}, \tag{5.8}$$

where ZHD and ZWD are the zenith hydrostatic and the wet delay, respectively. $M_d(e)$ and $M_w(e)$ are the associated mapping functions for the hydrostatic and the wet atmospheric delay, which depend on the elevation angle e.

Though the hydrostatic and the wet mapping function can be applied to map the tropospheric delay correction, the wet tropospheric delay component is usually hard to model. Therefore, the state vector element corresponding to the tropospheric delay correction can be considered as a correction for the wet component as well as for the total tropospheric delay when using a wet mapping function (Abdel-salam, 2005).

When the tropospheric wet delay parameter is considered, the slant total delay between the satellite and the antenna k at epoch i can be given as

$$\mathrm{STD}_i^k = M_d(e) \times \mathrm{ZHD}_i^k + M_w(e) \times \left(\mathrm{ZWD}_i^k + T_i^k\right), \tag{5.9}$$

where the T^k is the zenith wet delay parameter to be estimated at station k. For this parameter an empirical a priori constraints should be added according to the variations of the local atmosphere or the model for regional atmospheric corrections.

The nature of the tropospheric wet delay allows for modelling its components as a stochastic process. Therefore, the transition matrix and the noise matrix of the Kalman filter state equation will consist of elements as given by (Chen, 1998; Abdel-salam, 2005)

$$\Phi_{i,i-1}^{\mathrm{trop}} = \left[1\right] \tag{5.10}$$

and

$$\Sigma_{w_i^{\mathrm{trop}}} = \left[q^{\mathrm{trop}} \cdot \Delta t\right], \tag{5.11}$$

where the value of the spectral density of the tropospheric delay parameter q^{trop} is the common value used by many research works to model the stochastic properties of the tropospheric delay (Zumberge et al., 1997; Niell, 2001). The spectral density of the troposphere was chosen to be $10^{-9}\ \mathrm{m}^2/\mathrm{s}$ which was observed to perform well with many datasets (Abdel-salam, 2005).

5.4.2 A Common Tropospheric Wet Delay Parameter

It is often the case in airborne gravimetry that multiple GNSS receiving equipments are mounted on the kinematic platform. Since the tropospheric delay is uniform over such a small area like a kinematic platform, a common tropospheric delay parameter can be introduced as described below.

Assuming that all kinematic stations ($k_1, k_2, \ldots, k_j$) in Eq. (5.1) and Eq. (5.2) are mounted on the kinematic platform, the vector of the unknown parameters vector can be written as

$$\begin{aligned} X_i^{k_1} &= [x_i^{k_1}, y_i^{k_1}, z_i^{k_1}, T_i^{k_1}, \nabla\Delta N_1^{k_1}, \nabla\Delta N_2^{k_1}, \ldots, \nabla\Delta N_n^{k_1}]^{\mathrm{T}} \\ &\vdots \\ X_i^{k_j} &= [x_i^{k_j}, y_i^{k_j}, z_i^{k_j}, T_i^{k_j}, \nabla\Delta N_1^{k_j}, \nabla\Delta N_2^{k_j}, \ldots, \nabla\Delta N_n^{k_j}]^{\mathrm{T}} \end{aligned}\ . \tag{5.12}$$

The tropospheric zenith wet delay parameters out of Eq. (5.12) are

$$\left[\ldots, T_i^{k_1}, T_i^{k_2}, \ldots, T_i^{k_i}, \ldots\right]^{\mathrm{T}}, \tag{5.13}$$

where the elements of tropospheric zenith delay parameters are similar in the small area above the kinematic platform.

Thus, a common tropospheric zenith wet delay parameter is introduced for the multiple kinematic stations. The common tropospheric zenith wet delay parameter in the unknown parameter vector X_k will be changed as

$$\left[\ldots, T_i, \ldots\right]^{\mathrm{T}}. \tag{5.14}$$

This method not only reduces the amount of estimated parameters, but also harmonizes the actual conditions.

Generally, for solving the atmospheric delay parameters, there exist several usual methods such as single parameter estimation, multi-parameter estimation, piecewise linear estimation, stochastic estimation. In this study, a stochastic estimation is applied (Chen, 1998; Wei and Ge, 1998; Abdel-salam, 2005), where the tropospheric wet delay is computed on the basis of a first-order Gaussian-Markov model.

5.5 Experiment and Analysis

Since the distance constraints and a common tropospheric delay parameter were used for the study in this chapter, the accuracy evaluation method which uses the changes of the baseline length between the kinematic antennas cannot demonstrate the capability of the specific method as developed in this chapter. Thus, GNSS DD positioning results for a small region are used as “true value” for the comparison with results of the developed method applied for a large region. For this purpose, GNSS data of a shipborne gravimetry campaign on the Baltic Sea were used here.

From June 18 to 27, 2013, ten days of GNSS and gravimetric data were collected by GFZ and the Federal Agency for Cartography and Geodesy, Germany (BKG) in the Baltic Sea (Ostsee in German) near Greifswald, Germany. During this campaign, three GNSS antennas were mounted on the used ship. The positions of the GNSS antennas relative to each other are shown in Figure 5.2.

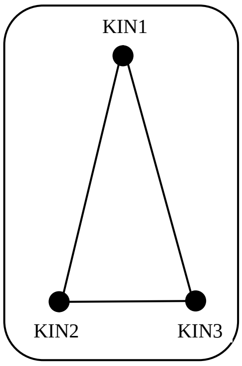

Figure 5.2: The relative positions of the kinematic GNSS antennas on the ship

In order to investigate the capability of the strategy, in this chapter the GNSS data of the first day of the Baltic Sea gravimetric experiment (June 18, 2013) were selected for testing. The GNSS stations KIN1 and KIN3 were selected as multiple kinematic stations. The baseline length of 26.342 m was used as the distance constraint in the following experiment. The stations 0801 and 0775 of the Satellite Positioning Service (SAPOS, www.sapos.de), which is organized by the Working Committee of the Surveying Agencies of the States of the Federal Republic of Germany (AdV), were taken as small regional reference stations (i.e. distances < 30 km) (cf. Figure 5.3). The IGS stations WARN and POTS were chosen as large regional reference stations (distance ~50-200 km). The tracks of the ship and the positions of the reference stations are shown in Figure 5.4. The hardware types of all GNSS receivers and antennas are given in Table 5.1.

Figure 5.3: The track of the ship (green curve) and the positions of the reference stations in a small region (yellow triangles) during the Baltic Sea shipborne gravimetric campaign on June 18. 2013

For the GNSS data processing, the HALO_GNSS software was used based on the methods described in this chapter. Here, the dual-frequency carrier phase observations were used to form the ionosphere-free linear combination. The tropospheric zenith wet delay was estimated as a random walk process, the initial uncertainty of which was assumed to be 10 cm and its spectral density $10^{-12}\ \mathrm{m}^2/\mathrm{s}$. The reasons for the selection of these values are the slow motion of the ship and the small changes in the height profile (Abdel-salam, 2005). The two-way Kalman filter was used for the parameter estimation and the GPS and GLONASS observation data were used for the calculation of the trajectories for the multiple kinematic stations KIN1 and KIN3.

Figure 5.4: The track of the ship (green curve) and the positions of reference stations (yellow triangles) for the Baltic Sea shipborne gravimetric experiment on June 18. 2013

Table 5.1: Hardware list of the selected stations from Baltic Sea gravimetric experiment

Station Name	Receiver type	Antenna type	(with dome)
KIN1	JAVAD TRE_G3TH DELTA	LEIAS10	NONE
KIN3	JAVAD TRE_G3TH DELTA	ACCG5ANT_42AT1	NONE
0801	TPS NET-G3A	TPSCR.G3	TPSH
0775	TPS NET-G3A	TPSCR.G3	TPSH
WARN	JPS LEGACY	LEIAR25.R3	LEIT
POTS	JAVAD TRE_G3TH DELTA	JAV_RINGANT_G3T	NONE

Experimental studies were performed with five computational schemes:

Scheme 1 (small region experiment): The trajectories of the multiple kinematic stations KIN1 and KIN3 were calculated by a single adjustment for the same time with a common tropospheric delay parameter, where 0801 and 0775 served as multiple reference stations in small region.

The baseline length between the two kinematic stations KIN1 and KIN3 was calculated for each epoch. The apparent changes of this baseline length are shown in Figure 5.5 and the statistical results are given in Table 5.2. These results can be treated as the “true value” (with the standard deviations of 1.5 cm in the related distance) of the antenna movement. Since the results of KIN1 and KIN3 are nearly the same, only the KIN1 is used for comparisons with the following schemes.

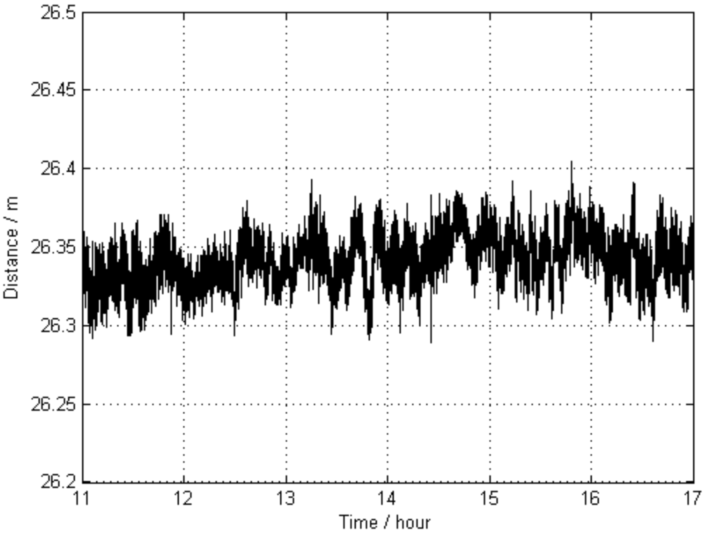

Figure 5.5: The distance between two antennas, KIN1 and KIN3; the trajectories of these antennas were estimated by using two reference stations, 0801 and 0775

Scheme 2 (large region experiment): The trajectories of the multiple kinematic stations KIN1 and KIN3 were calculated by a single adjustment for the same time with two independent tropospheric delay parameters, where WARN and POTS served as multiple reference stations located in the large region.

The baseline length between two kinematic stations KIN1 and KIN3 was calculated for each epoch. The apparent changes of this baseline length are shown in Figure 5.6 and the statistical results are given in Table 5.2. The results showed that the precision of scheme 2 is lower than that of scheme 1. The tracks of KIN1 for the large region were compared with the “true value” of scheme 1. The comparison results are shown in Figure 5.7 and the statistics of the comparison as given in Table 5.3 show that the achieved accuracy is 5.8 mm, 4.4 mm and 36.7 mm for the north, east and up directions, respectively.

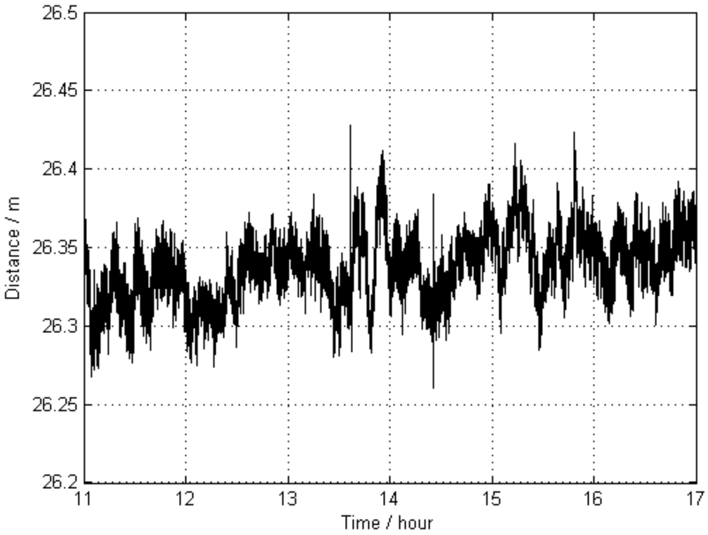

Figure 5.6: The distance between two antennas, KIN1 and KIN3; the tracks of these antennas were estimated by using two reference stations, WARN and POTS

Table 5.2: The statistical results for the baseline length between KIN1 and KIN3 (Unit: m)

Scheme	Region type	Min	Max	Mean	SDev
1	**Small region**	26.282	26.406	26.342	0.015
2	**Large region**	26.261	26.428	26.338	0.022

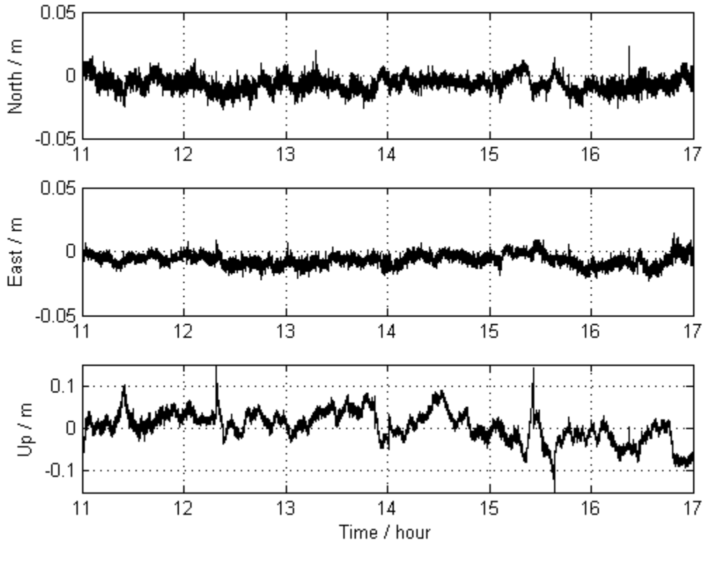

Figure 5.7: The results for KIN1 for the large region with two independent tropospheric delay parameters compared with scheme 1 (differences)

Scheme 3: Based on the scheme 2, the a priori distance constraints were used to calculate the tracks of KIN1 and KIN3.

Scheme 4: Based on the scheme 2, a common tropospheric delay parameter between the kinematic stations was used to calculate the tracks of KIN1 and KIN3.

Scheme 5: Based on the scheme 2, a common tropospheric delay parameter and the distance constraints were used to calculate the tracks of KIN1 and KIN3.

The trajectories of KIN1 for the schemata 3, 4 and 5 were compared with the "true value" of scheme 1, respectively. The comparisons of the results are shown in Figure 5.8, Figure 5.9 and Figure 5.10, respectively. And the statistics results of the comparisons are given in Table 5.3.

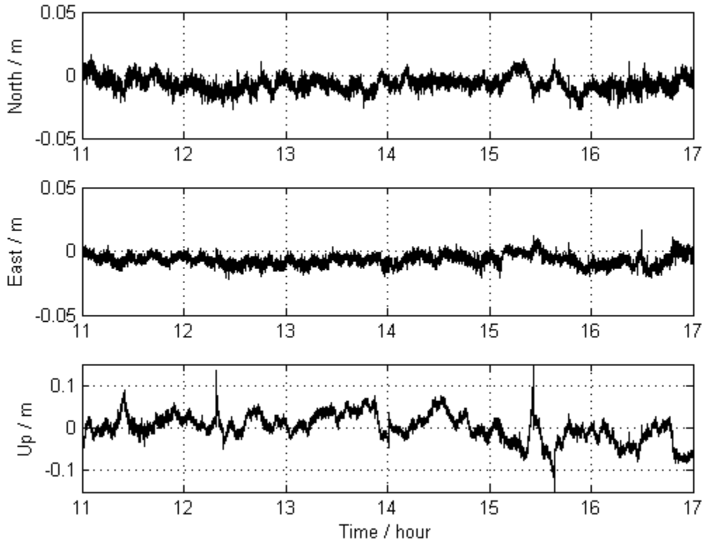

Figure 5.8: The results for scheme 3 for KIN1 for the large region with two independent tropospheric delay parameters and distance constraints compared with scheme 1 (differences)

From the above computational results, the following conclusions can be drawn:

(1) The precision of the kinematic state estimates provided by the DD processing using reference stations in the large region is lower than those provided in the small region.

(2) The accuracies of the estimated kinematic state parameters can be improved by the distance constraints, because of the relationships or known information between states parameters are used in GNSS precise kinematic positioning.

(3) The method which calculates multiple kinematic stations together and uses a common tropospheric delay parameter for these kinematic stations, can improve the kinematic

positioning accuracy as well, since it can reduce the amount of unknown parameters and represents the reality better.

(4) By integration of distance constraints and using a common tropospheric delay parameter in GNSS precise kinematic positioning, the accuracies for the Up direction (cf. the corresponding mean and RMS values of Table 5.3) can be further improved.

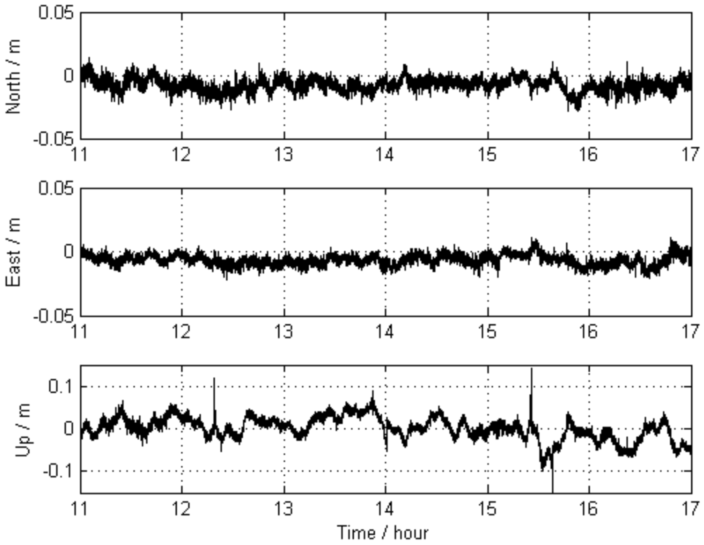

Figure 5.9: The results of scheme 4 for KIN1 with reference stations in the large region with a common tropospheric delay parameter for KIN1 and KIN3 compared with scheme 1 (differences)

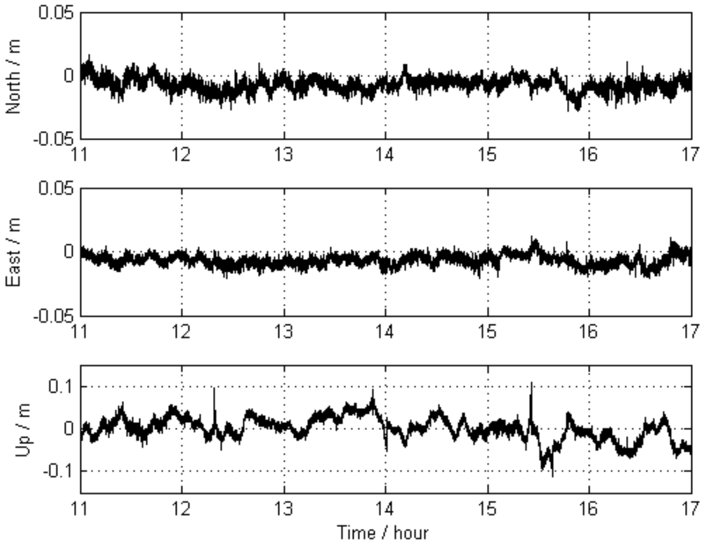

Figure 5.10: The results of scheme 5 for KIN1 with reference stations in the large region with a common tropospheric delay parameter and distance constraints compared with scheme 1 (differences)

Table 5.3: Statistical results of each scheme compared with scheme 1 (Unit: mm)

Scheme		**Direction**	**Min**	**Max**	**Mean**	**RMS**
2	Two independent tropospheric parameters	North	-27.0	23.0	-6.4	5.8
		East	-23.5	14.8	-6.4	4.5
		Up	-165.7	165.9	3.5	36.8
3	A priori Distance constraints	North	-27.7	15.8	-6.4	5.8
		East	-21.6	16.4	-6.6	4.2
		Up	-161.6	145.4	0.0	33.1
4	A common tropospheric parameter	North	-28.5	14.2	-7.2	5.2
		East	-21.5	11.5	-6.4	4.1
		Up	-151.4	142.1	0.6	27.8
5	A priori Distance constraints and a common tropospheric parameter	North	-28.6	15.9	-6.8	5.4
		East	-21.4	11.6	-6.6	4.1
		Up	-112.5	108.4	0.0	27.3

5.6 Conclusions

In this chapter a method of GNSS kinematic positioning based on multiple kinematic stations with multiple reference stations was described. It can be used to provide a basis for the research when multiple kinematic stations exist.

It is often the case that multiple GNSS receiving equipments are mounted on the kinematic platform, so that known functionals or theoretical relations exist among the unknown parameters of the individual GNSS receiving equipments. The distance among the multiple GNSS antennas is known and fixed, which has been used as a priori distance constraint to improve the RMS accuracy of the state estimates. The characteristics of the tropospheric delay in a small area are similar. Therefore, a common tropospheric delay parameter was used for the multiple kinematic stations, which can enhance the accuracy and reliability of the state estimates as well, because it can reduce the amount of unknown parameters and represents the reality better.

Finally, a shipborne gravimetric experiment is used to test above methods since its results with reference stations in the small region can be used as “true value” to compare with those based on the reference stations in the large region. Through integration of distance constraints and a common tropospheric delay parameter accuracies can be further improved.

6 Kinematic Positioning Based on GNSS Integration

6.1 Introduction

The integration of multiple GNSS satellite systems may be considered as a major milestone in GNSS precise positioning, because it can dramatically improve the reliability and productivity of GNSS positioning (Wang et al., 2001).

It is well known that, for GNSS based precise positioning systems, the accuracy, availability and reliability of the positioning results are strongly dependent on the number of satellites being tracked, especially in kinematic positioning. However, in some situations, GNSS signals are blocked or essentially degraded by natural or artificial obstacles, such as in urban canyons (shown in Figure 6.1), mountainous areas and in deep open-cut mines, so that the number of visible satellites may not be sufficient for the positioning function (Wang et al., 2001; Angrisano et al., 2013). In case of a single satellite system, when there are not enough observations or even no observation, kinematic positioning results are of poor accuracy, unreliable, or even fail.

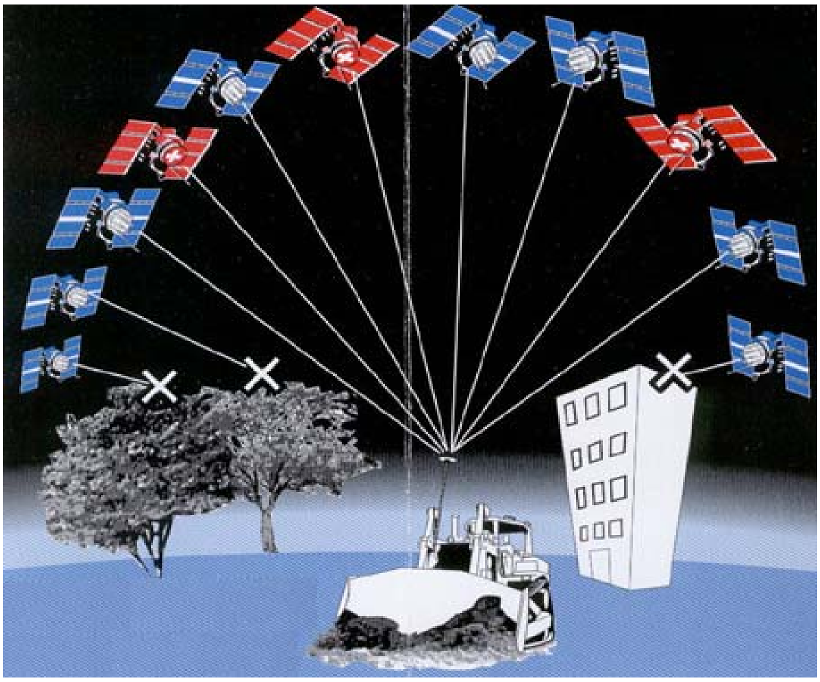

Figure 6.1: GNSS integration (OpeNaviGate, 2012)

In applications of long baseline GNSS differential positioning (such as the GEOHALO project), the number of simultaneously visible satellites will be reduced with the increase of the baseline length. A possible way to fill this gap is using a GNSS multi-constellation receiver, considering the combined use of GPS with the signals of other GNSS systems such as GLONASS, Galileo, the BeiDou navigation Satellite System (BDS) etc. In general, the usage of multiple GNSS systems will increase the number of simultaneously visible satellites and improve the reliability.

Furthermore, in this chapter, a GNSS integration algorithm based on Helmert's variance components estimation is used to reasonably adjust the weights and the contributions among multiple GNSS systems.

Currently Galileo has only four satellites in orbit, in the In-Orbit Validation (IOV) phase (ESA, 2014), while BDS is in the development phase and only the regional phase (Asia-Pacific area) has been completed at the end of 2012 (Zhao et al., 2013; BDS, 2014). The enhancement of the Russian space program has made GLONASS an ideal candidate to form a multi-constellation with GPS (Angrisano et al., 2013). In the following section, GPS and GLONASS are considered because they are the only GNSS systems which are declared to be fully operational.

6.2 GPS and GLONASS Integration

There is a strong interest in including GLONASS satellites in any GPS positioning solution. It is well known that additional satellites strengthen the solution and increase its reliability (Leick 1998). Unlike GPS, GLONASS satellites transmit signals at different frequencies, which causes a significant complexity in terms of the modelling and ambiguity resolution for an integrated GPS and GLONASS data processing system (Wang et al., 2001).

Referring to the coordinates on the Earth's surface, the terrestrial reference system of GPS is the World Geodetic System 1984 (WGS-84) and for GLONASS it is the Parametry Zemli 1990 (PZ-90). GPS time (GPST) is connected to the Coordinated Universal Time (UTC) which is maintained by the US Naval Observatory (USNO). The GLONASS time (GLOT) scale is connected to TUC (RU) which is a kind of UTC maintained by Russia. The transformation formula between GPST and GLOT is

$$\mathrm{GPST} = \mathrm{GLOT} + \tau_r + \tau_u + \tau_g , \tag{6.1}$$

where τ_r is the time offset between GLOT and UTC(RU). τ_u is the time offset between UTC(RU) and UTC(USNO). τ_g denotes the time offset between GPST and UTC(USNO) (Hofmann-Wellenhof et al., 2008, p. 315; Angrisano et al., 2013). In this study, WGS84 and

GPST were used as reference systems. More details about the reference systems and their transformations into one another can be found in Roßbach (2001), Habrich (2000), Xu (2007) and Hofmann-Wellenhof et al. (2008).

As well known, carrier phase measurements are much more precise than pseudorange observations. Hence, they are the primary measurements for precise positioning. The DD carrier phase observation equations for GPS and GLONASS (Roßbach, 2001; Wang et al., 2001) at epoch i are given as

$$\lambda^{GPS}\nabla\Delta\varphi_{k-r}^{p-q^{GPS}} = \nabla\Delta\rho_{k-r}^{p-q^{GPS}} + \lambda^{GPS}\nabla\Delta N_{k-r}^{p-q^{GPS}} + \nabla\Delta T_{k-r}^{p-q} + \lambda^{GPS}\nabla\Delta e_{k-r}^{p-q^{GPS}} \qquad (6.2)$$

and

$$\begin{aligned}\lambda^{p^{GLO}}\Delta\varphi_{k-r}^{p^{GLO}} - \lambda^{q^{GLO}}\Delta\varphi_{k-r}^{q^{GLO}} &= \nabla\Delta\rho_{k-r}^{p-q^{GLO}} + \lambda^{p^{GLO}}\Delta N_{k-r}^{p^{GLO}} - \lambda^{q^{GLO}}\Delta N_{k-r}^{q^{GLO}} \\ &\quad + \nabla\Delta\mathrm{ICB}_{k-r}^{p-q^{GLO}} + \nabla\Delta T_{k-r}^{p-q} + \lambda^{p^{GLO}}\Delta e_{k-r}^{p^{GLO}} - \lambda^{q^{GLO}}\Delta e_{k-r}^{q^{GLO}},\end{aligned} \qquad (6.3)$$

where the superscripts p and q indicate the reference satellite and the other satellite, respectively. The subscripts r and k mean the reference station and the kinematic station, respectively. Δ denotes the single difference operator between the reference station and the kinematic station, for example $\Delta\varphi_{k-r}^{p}$ denotes $\varphi_k^p - \varphi_r^p$. $\nabla\Delta$ is the DD operator among two satellites and two stations, for example $\nabla\Delta\rho_{k-r}^{p-q} = \Delta\rho_{k-r}^{p} - \Delta\rho_{k-r}^{q}$. λ is the wavelength of the carrier phase of the satellite signal, φ is the carrier phase observation between a satellite and a receiver. ρ is the geometrical distance between a satellite and a receiver with

$$\rho_r^p = \sqrt{\left(x_r - x^p\right)^2 + \left(y_r - y^p\right)^2 + \left(z_r - z^p\right)^2}\,. \qquad (6.4)$$

N is the carrier phase ambiguity and T is the atmospheric delay along the path. e is the measurement noise of the carrier phase and ICB is the inter-channel bias for measurements on different carrier frequencies for different satellites. It is difficult to separate the DD carrier phase bias $\nabla\Delta\mathrm{ICB}_{k-r}^{p-q^{GLO}}$ from the ambiguity parameter. Thus, the float solution for the GLONASS DD ambiguity is used in this study.

From Eq. (6.2) and (6.3), the error equations of GPS and GLONASS integration can be written as

$$\begin{bmatrix} V_1 \\ V_2 \end{bmatrix} = \begin{bmatrix} A_1 \\ A_2 \end{bmatrix} \cdot \begin{bmatrix} x \\ y \\ z \end{bmatrix} + \begin{bmatrix} B_1 \\ B_2 \end{bmatrix} \cdot \left[T\right] + \begin{bmatrix} I & 0 \\ 0 & I \end{bmatrix} \cdot \begin{bmatrix} \nabla\Delta N_1 \\ \nabla\Delta N_2 \end{bmatrix} - \begin{bmatrix} L_1 \\ L_2 \end{bmatrix}, \qquad (6.5)$$

where V_i ($i = 1, 2$) denotes the $n_i \times 1$ residual vector. A_i is the $n_i \times 3$ design matrix of state parameters $[x, y, z]^{\mathrm{T}}$ of the kinematic station. B_i is the $n_i \times 1$ coefficient matrix of the tropospheric delay parameter $[T]$. The state parameters $[x, y, z]^{\mathrm{T}}$ and the tropospheric delay parameter $[T]$ are common parameters of the kinematic station between two GNSS systems at the same epoch. The DD ambiguity parameters $[\nabla\Delta N_1 \quad \nabla\Delta N_2]^{\mathrm{T}}$ between the two systems are uncorrelated. The observation vectors L_1 and L_2 are independent of each other.

The estimates for the kinematic station can be calculated using the estimation theory (cf. Chapter 3). The accuracy of the multiple GNSS measurement vectors is usually different. In order to balance the contributions of the various GNSS measurements, the final result is obtained by using the principle of Helmert's variance component estimation.

6.3 GNSS Integration Based on Helmert's Variance Components Estimation

The variance component estimation (VCE) was developed by Friedrich Robert Helmert in 1907 (Helmert, 1907) as cited by (Xu et al., 2007) and it has been adopted for a variety of approaches (Sahin et al., 1992; Crocetto et al., 2000; Koch and Kusche, 2002; Kusche, 2003; Yang et al., 2005; Vennebusch et al., 2007; Xu et al., 2007; Teunissen and Amiri-Simkooei, 2008; Wang et al., 2009a). The purpose of VCE is to find the realistic and reliable variance components for the observations in order to construct correctly the a priori covariance matrix of the observations (Sahin et al., 1992).

In the GNSS kinematic positioning, let us consider k types of GNSS measurements as $n_i \times 1$ vectors L_i for $i = 1, 2, \ldots, k$. The GNSS observation equations can be written as

$$\begin{bmatrix} L_1 \\ L_2 \\ \vdots \\ L_k \end{bmatrix} = \begin{bmatrix} A_1 \\ A_2 \\ \vdots \\ A_k \end{bmatrix} \cdot X + \begin{bmatrix} e_1 \\ e_2 \\ \vdots \\ e_k \end{bmatrix}. \tag{6.6}$$

The matrix A_i is the $n_i \times m$ design matrix. X denotes a $m \times 1$ vector of the unknown parameters. e_i is the theoretical measurement error vector with zero mean and the covariance matrix is Σ_i with $\Sigma_i = \sigma_{0,i}^2 P_i^{-1}$. The value $\sigma_{0,i}^2$ is the variance of unit weight and P_i denotes the weight matrix of the observations.

The observation vectors may be internally correlated (the noise may be coloured) but we assume them to be uncorrelated between groups. Moreover, we assume that the covariance matrices of these observation groups are known a priori up to some scaling factors, the k noise levels or variance components $\sigma_{0,i}^2$,

$$\Sigma = \begin{bmatrix} \Sigma_1 & 0 & \dots & 0 \\ 0 & \Sigma_2 & \dots & 0 \\ \vdots & \vdots & \ddots & \vdots \\ 0 & 0 & \dots & \Sigma_k \end{bmatrix} = \begin{bmatrix} \sigma_{0,1}^2 P_1^{-1} & 0 & \dots & 0 \\ 0 & \sigma_{0,2}^2 P_2^{-1} & \dots & 0 \\ \vdots & \vdots & \ddots & \vdots \\ 0 & 0 & \dots & \sigma_{0,k}^2 P_k^{-1} \end{bmatrix}. \tag{6.7}$$

Eq (6.7) indicates that $L_1, L_2, \dots, L_k$ do not have the same variance of unit weight σ_0^2. Fortunately, the variances for individual measurements or the variance components for the grouped measurements can a posteriory be estimated based on the measurement residuals from Least squares solution for the parameters.

The purpose of VCE is to estimate the variance factors $\sigma_{0,i}^2$ $(i = 1, 2, \dots, k)$ and iteratively or adaptively adjust the measurement weights or variances using the available measurements (Wang et al., 2009a).

Based on Helmert's most popular VCE method (Helmert, 1907; Förstner, 1979; Koch, 1986; Kusche, 2003; Bähr et al., 2007), the variance components can be estimated from the following equation:

$$\begin{bmatrix} U_{11} & U_{12} & \dots & U_{1k} \\ U_{21} & U_{22} & \dots & U_{2k} \\ \vdots & \vdots & \ddots & \vdots \\ U_{k1} & U_{k2} & \dots & U_{kk} \end{bmatrix} \cdot \begin{bmatrix} \hat{\sigma}_{0,1}^2 \\ \hat{\sigma}_{0,2}^2 \\ \vdots \\ \hat{\sigma}_{0,k}^2 \end{bmatrix} = \begin{bmatrix} V_1^{\mathrm{T}} P_1 V_1 \\ V_2^{\mathrm{T}} P_2 V_2 \\ \vdots \\ V_k^{\mathrm{T}} P_k V_k \end{bmatrix}, \tag{6.8}$$

where

$$U_{ii} = n_i - 2tr(N^{-1}N_i) + tr(N^{-1}N_i)^2, \tag{6.9}$$

and

$$U_{ij} = U_{ji} = tr(N^{-1}N_i N^{-1}N_j), \tag{6.10}$$

with $i, j = 1, 2, \dots, k$ and $i \neq j$,

$$N = \sum_{i=1}^{k} N_i, \tag{6.11}$$

$$N_i = A_i^{\mathrm{T}} P_i A_i \tag{6.12}$$

and

$$V_i = A_i \hat{X} - L_i \,, \tag{6.13}$$

where V_i is the estimated error vector and $\hat{X}$ is the estimated parameter vector.

The inverse of the coefficient matrix in Eq. (6.8) makes the method inconvenient. It is the most time-consuming computation step. Correspondingly, a number of simplified formulas have been developed (Förstner, 1979; Grafarend et al., 1980; Grodecki, 1997; Bähr et al., 2007). Starting from the Helmert estimator, Förstner (1979) derived a simplified estimator with some considerable advantages. The name “Förstner method” has been given by Persson (1980), and the simplified estimator is obtained by

$$\hat{\sigma}_{0,i}^2 = \frac{V_i^{\mathrm{T}} P_i V_i}{r_i} \tag{6.14}$$

with

$$r_i = n_i - tr(N^{-1} N_i) \,. \tag{6.15}$$

Obviously, Eq. (6.14) can be applied easily because it does not need any extra calculations. This advantage is caused by the fact that the redundant contribution of the measurements is always required in the data processing for the purpose of outlier detection or reliability analysis (Wang et al., 2009a). It should be pointed out that outliers must be removed prior to the application of VCE.

6.4 Experiment and Analysis

In order to investigate the capability of the strategy as described in this chapter, the kinematic GNSS data of the GEOHALO mission and the static GNSS data of the IGS network were used.

6.4.1 Kinematic Experiment

The kinematic GNSS data of the GEOHALO flight on June 6, 2012 were selected for the test. The selected kinematic stations are AIR5 and AIR6 in the front and back part of the HALO aircraft, respectively (cf. Figure 4.5). The station REF6, installed by GFZ next to the runway of the DLR airport in Oberpfaffenhofen, and the station ASCE located in the central region of Italy were selected as reference stations. The hardware types of all receivers and antennas are the same as in the experiment described in Section 4.3.2 (cf. Table 4.2). The trajectory of the HALO aircraft on June 6, 2012 and the positions of the selected reference stations are shown in Figure 6.2. The selected data contain GPS and GLONASS observations with a sampling rate of 20 Hz.

For the data processing, the HALO_GNSS software was used. This software for precise kinematic positioning and velocity determination was developed at GFZ in the frame of this thesis. The IGS precise ephemeris (Kouba, 2009b) were chosen and the GPS and GLONASS satellite elevation angle was limited to 10°. The number of GPS, GLONASS and GPS + GLONASS satellites is shown in Figure 6.3 as blue, green and red line, respectively. As observations we used the ionospheric-free linear combination (Hofmann-Wellenhof et al., 2008, p. 111; Xu, 2007, p. 97) of pseudorange and carrier phase observations, respectively. The two-way Kalman filtering method was used for the parameter estimation.

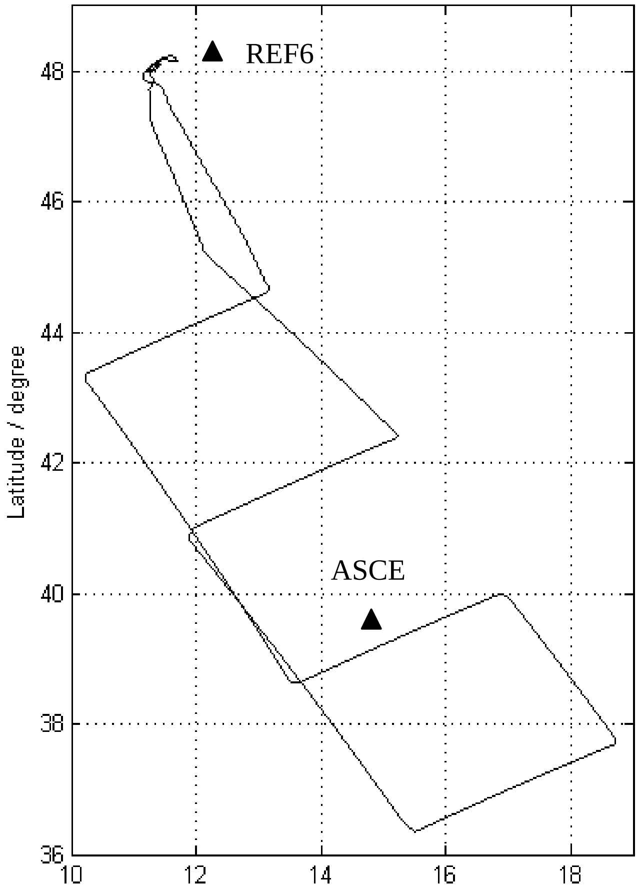

Figure 6.2: The HALO aircraft flight trajectory on June 6, 2012 and the location of the selected reference stations

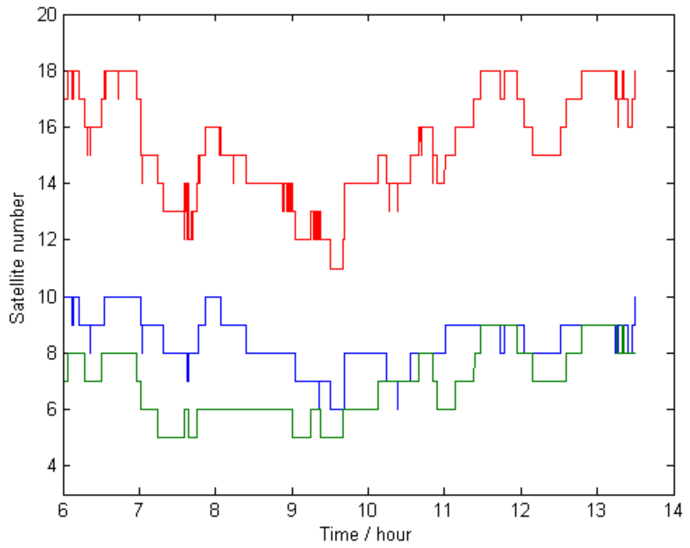

Figure 6.3: Number of the selected satellites of GPS (blue line), GLONASS (green line) and GPS+GLONASS (red line) for the kinematic experiment (GEOHALO flight on June 6, 2012)

In order to investigate the accuracy and reliability of the developed algorithm and software, firstly the positions of the kinematic stations AIR5 and AIR6 were calculated with REF6 and ASCE as multiple reference stations, and secondly the baseline length between two kinematic stations AIR5 and AIR6 was calculated for every epoch. The accuracy and reliability of the kinematic results were then validated based on the apparent variations of the baseline length. The following four schemes were compared.

Scheme 1 (GPS as a single GNSS system): GPS as a single system was used and the positions of the kinematic stations AIR5 and AIR6 were calculated together with REF6 and ASCE. The result for the baseline is shown in Figure 6.4 as a time series and its statistical characteristics are listed in Table 6.1.

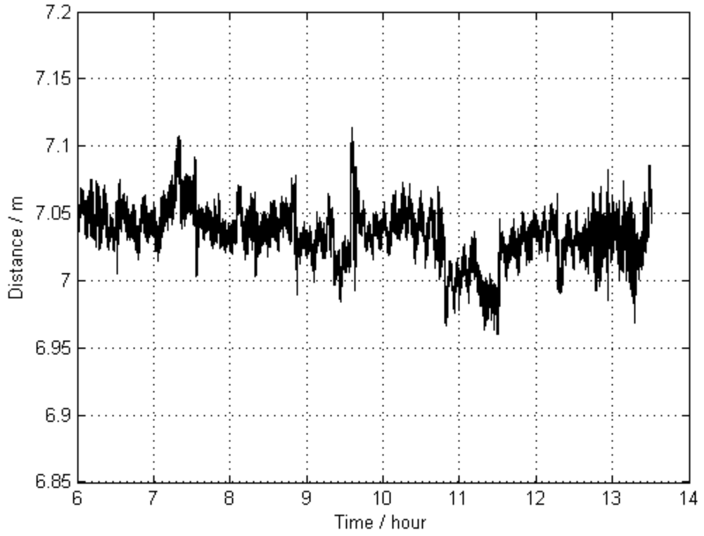

Figure 6.4: The time series for the apparent baseline length variation between AIR5 and AIR6 based on GPS as a single GNSS system

Scheme 2 (GLONASS as a single GNSS system): GLONASS as a single system was used and the positions of the kinematic stations AIR5 and AIR6 were calculated together with REF6 and ASCE. The result for the baseline is shown in Figure 6.5 as a time series and its statistical characteristics are listed in Table 6.1.

Scheme 3 (GPS and GLONASS as an integrated GNSS system with 1:1 weights): GPS and GLONASS were used together and the positions of the kinematic stations AIR5 and AIR6 were calculated together with REF6 and ASCE. The ratio of the a priori observation accuracy between GPS and GLONASS systems is set to 1:1. The result for the baseline is shown in Figure 6.6 as a time series and its statistical characteristics are listed in Table 6.1.

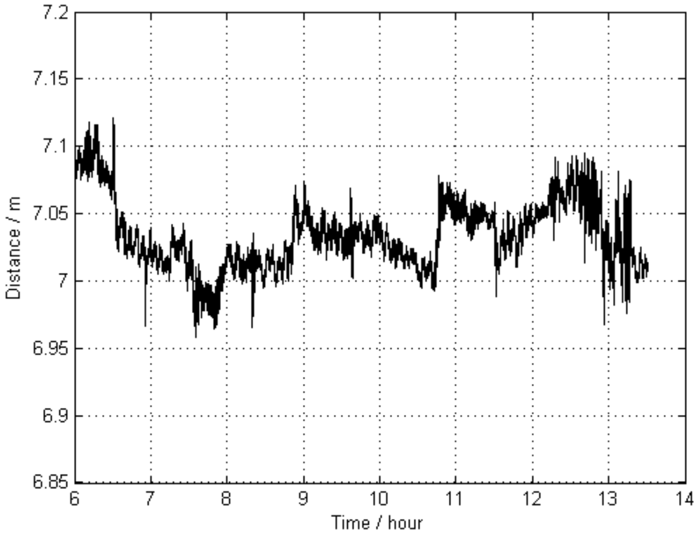

Figure 6.5: The time series for the apparent baseline length variation between AIR5 and AIR6 based on GLONASS as a single GNSS system

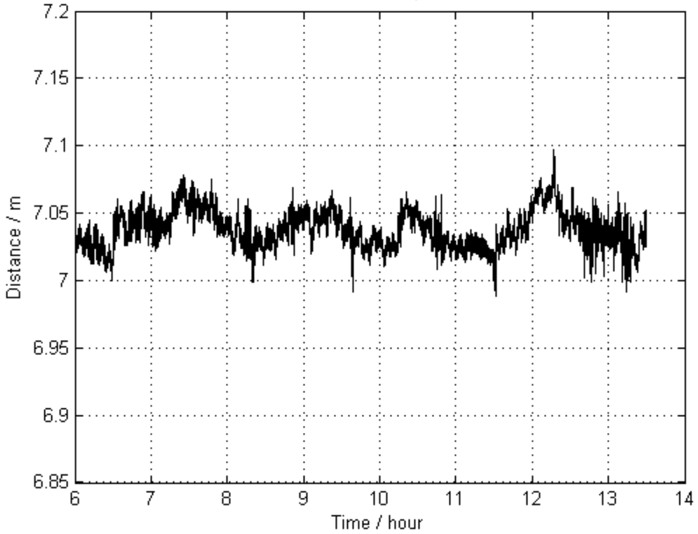

Figure 6.6: The time series for the apparent baseline length variation between AIR5 and AIR6 based on GPS and GLONASS as an integrated system with 1:1 weights

Scheme 4 (GPS and GLONASS as an integrated system with Helmert's VCE): GPS and GLONASS were used together and the positions of the kinematic stations AIR5 and AIR6 were calculated together with REF6 and ASCE. The relation of the observations accuracies between GPS and GLONASS was determined by Helmert's VCE. Outliers must be removed prior to the application of VCE. The ratios between the weights for the GPS and GLONASS observations are shown in Figure 6.7. The apparent changes of the baseline length are shown in Figure 6.8 as a time series and their statistical features are listed in Table 6.1.

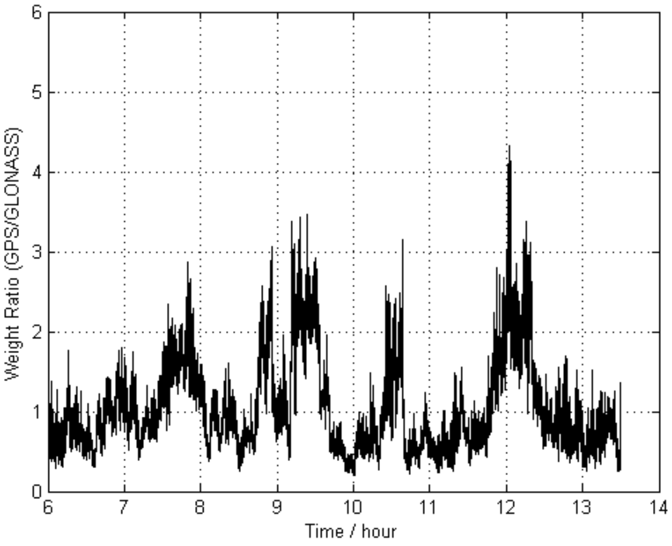

Figure 6.7: The ratios between the weights for the GPS and GLONASS observations

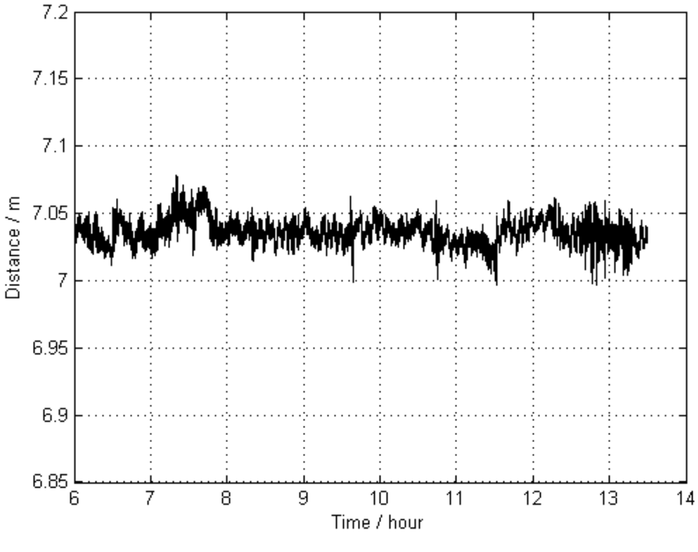

Figure 6.8: The time series for the apparent baseline length variation between AIR5 and AIR6 based on GPS and GLONASS as an integrated system with Helmert's VCE

Table 6.1: The statistical results of schemata 1-4

Scheme		Apparent distance between AIR5 and AIR6 (Unit: m)			
		Min	**Max**	**Mean**	**SDev**
1	G (GPS)	6.960	7.114	7.034	0.019
2	R (GLONASS)	6.958	7.121	7.034	0.026
3	G+R (1:1 weights)	6.989	7.097	7.038	0.014
4	G+R (Helmert weights)	6.997	7.078	7.036	0.009

These results show the following:

(1) By the comparison of scheme 1 and 2, it can be concluded that the kinematic positioning accuracy based on GLONASS as a single system is a little bit lower than the GPS-only accuracy.

(2) The results for scheme 3 show that the method of GPS and GLONASS integration can improve the accuracy of GNSS kinematic positioning. This is caused by an increased number of observations as well as by more available GNSS satellites and improves the stability and reliability (as an increase in redundancy numbers) of the parameter estimation.

(3) By the comparison of schemes 3 and 4 it can be found that the method which is based on of Helmert's VCE can further improve the accuracy of the integrated GNSS kinematic positioning, because it can reasonably adjust the weights and the contributions of the different GNSS systems.

6.4.2 Static Experiment

In order to test the accuracy and reliability of the algorithm and software in a static data experiment, the static GNSS observation data of the IGS sites TITZ and FFMJ (both in Germany) on January 1, 2013 were randomly selected for testing. The length of this baseline is about 190 km. The hardware types of the receivers and antennas are given in Table 6.2. The number of GPS, GLONASS and GPS+GLONASS satellites is shown in Figure 6.9 as blue, green and red line, respectively. FFMJ was selected as the reference station. The station TITZ was processed by the HALO_GNSS software using kinematic processing. The results were compared with the coordinates taken from the IGS website (http://www.igs.org), which were regarded as "truth". The following four schemes were compared.

Table 6.2: Hardware list of the selected IGS sites

Station Name	Receiver type	Antenna type (with dome)
TITZ	JPS LEGACY	LEIAR25.R4 LEIT
FFMJ	JPS LEGACY	LEIAR25.R4 LEIT

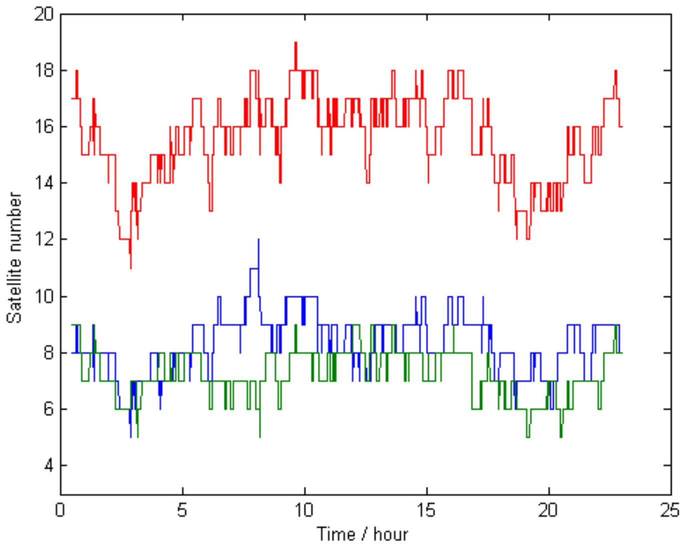

Figure 6.9: The number of selected satellites of GPS (blue line), GLONASS (green line) and GPS+GLONASS (red line) for the static experiment (IGS station TITZ and FFMJ on January 1, 2013)

Scheme 1: The GPS system was used alone to calculate the position of TITZ.

Scheme 2: The GLONASS system alone was used to calculate the position of TITZ.

Scheme 3: The GPS and GLONASS integrated system was used to calculate the position of TITZ with 1:1 weights.

Scheme 4: The GPS and GLONASS integrated system was used to calculate the position of TITZ with Helmert’s VCE.

The differences between the “true values” and the results of the schemes 1-4 are shown in Figures 6.10, 6.11, 6.12 and 6.13 as a time series, respectively. The statistics of comparisons are given in Table 6.3.

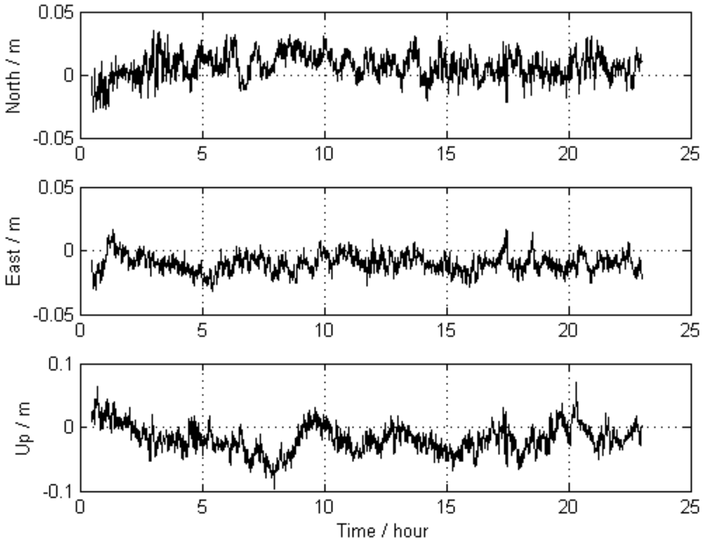

Figure 6.10: The differences between the IGS result and the GPS kinematic positioning results for the baseline TITZ – FFMJ (scheme 1)

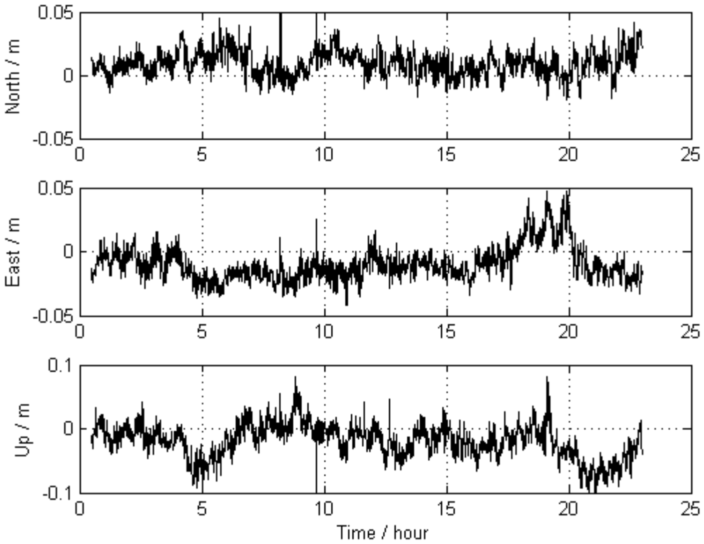

Figure 6.11: The differences between the IGS result and the GLONASS kinematic positioning results for the baseline TITZ – FFMJ (scheme 2)

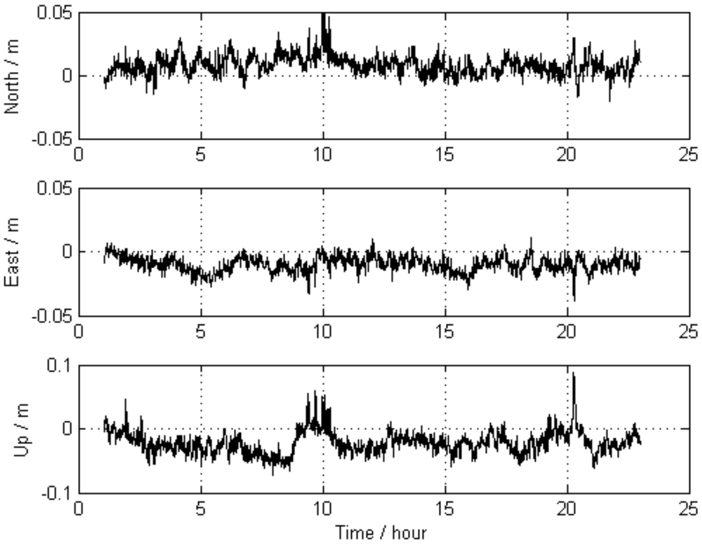

Figure 6.12: The differences between the IGS result and the GPS+GLONASS (with 1:1 weights) kinematic positioning results for the baseline TITZ – FFMJ (scheme 3)

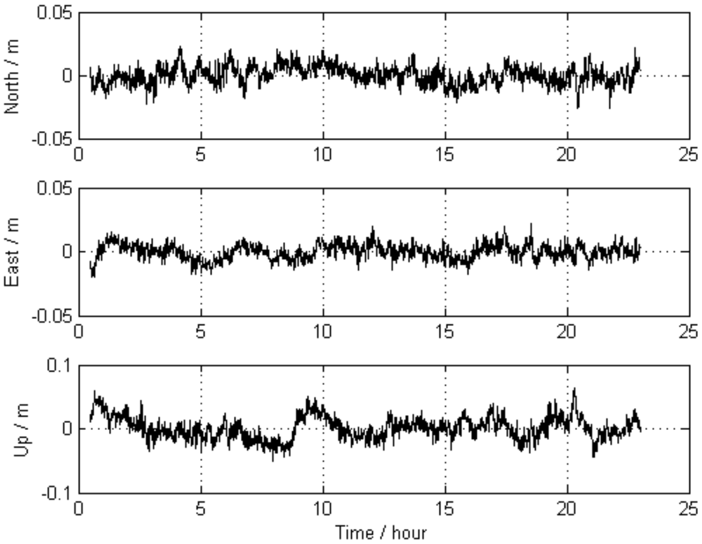

Figure 6.13: The differences between the IGS result and the GPS+GLONASS (with Helmert weights) kinematic positioning results for the baseline TITZ – FFMJ (scheme 4)

These experiments based on kinematic processing of static data illustrate the effectiveness, repeatability and stability of the proposed method in static data. The accuracy of GNSS kinematic positioning based on GLONASS alone is a little bit lower than the GPS-only accuracy. The combination of both GPS and GLONASS is better than their use as single systems, and improves both the accuracy and reliability. The method based on Helmert's VCE can further improve the accuracy of the integrated GNSS kinematic positioning. The ratios between the weights for the GPS and GLONASS observations are shown in Figure 6.14.

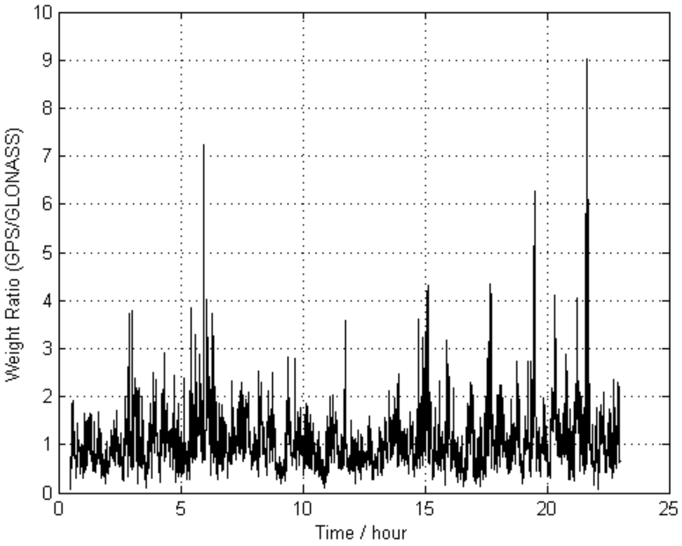

Figure 6.14: The ratios between the weights for the GPS and GLONASS observations (scheme 4)

Table 6.3: Statistical results for the IGS station TITZ (Unit: mm)

Scheme		**Directions**	**Min**	**Max**	**Mean**	**RMS**
1	G(GPS)	North	-29.8	34.8	6.6	10.0
		East	-32.3	17.0	-9.8	7.1
		Up	-97.4	71.7	-18.3	21.6
2	R(GLONASS)	North	-19.6	92.0	9.4	10.1
		East	-41.8	47.6	9.7	13.3
		Up	-111.5	82.2	-19.2	26.8
3	G+R (1:1 weights)	North	-20.1	55.8	8.0	7.7
		East	-39.0	11.0	9.8	6.1
		Up	-73.5	87.3	-21.6	17.9
4	G+R (Helmert weights)	North	-25.9	23.0	0.0	7.2
		East	-20.2	21.9	0.1	6.0
		Up	-51.5	62.8	0.9	17.6

6.5 Conclusions

In this chapter it has been shown that the application of the GNSS integration can improve the accuracy and reliability of GNSS positioning. Since the Galileo system and the BeiDou Navigation Satellite System (BDS) are currently still under construction, only the GPS and GLONASS systems are used in this study for a multi-system combination. The exercise of mathematical models and processing methodologies for integrated systems is a valuable topic as it identifies crucial issues concerning the combination of two or more GNSS positioning systems. Hence these are experiences that can be applied to the other GNSS systems that might integrate GPS with Galileo, GLONASS, BDS, or all four. Here it has been shown that the accuracy of GNSS kinematic positioning based only on GLONASS as a single system is a little bit worse than for GPS-only. But the combination of GPS and GLONASS is better than using them as single systems and improves the accuracy and reliability. Finally it has been shown that Helmert's VCE method can be applied to estimate the weights of the multiple GNSS observation data and can further improve the accuracy of integrated GNSS kinematic positioning.

7 GNSS Velocity Determination Based on the Doppler Effect

7.1 Introduction

Accurate estimates of the velocity of a platform are often needed in high dynamics positioning, airborne gravimetry, GNSS/Inertial navigation System (INS) integration and geophysical exploration, etc (Szarmes et al., 1997; Bruton et al., 1999). GNSS is a cost-effective means to obtain reliable and highly accurate velocities by exploiting the receiver raw and carrier phase derived Doppler measurements (Szarmes et al., 1997). GNSS velocity determination can be based on the Doppler effect. Its principle was first proposed by the Austrian mathematician and physicist Christian Andreas Doppler (1842).

In the present chapter, firstly the principle of GNSS raw Doppler velocity determination is discussed, and subsequently the velocity determination by carrier phase derived Doppler observations is described as well. In order to improve the accuracy and the reliability of the velocity determination, the algorithms of GNSS integration and robust estimation are applied as well. Finally, the actually measured GNSS data of the kinematic and static experiments are applied to validate the presented methods and the importance of precise velocity determination for airborne gravimetry is discussed.

7.2 Principle of Doppler-Based Velocity Determination

When a wave source is moving relative to an observer the perceived wave frequency is different from the emitted frequency (Jonkman, 1980). This effect is named Doppler effect and has been widely used in velocity determination.

The estimation of the velocity from discrete time signals in GNSS is based on the receiver generated raw Doppler measurements and Doppler observations derived from the carrier phase measurements (Cannon et al., 1997; Bruton et al., 1999). The receiver generated raw Doppler measurement is a measure of near instantaneous velocity, whereas the carrier phase derived Doppler observation is a measure of the mean velocity between observation epochs. The raw measurements are usually noisier than the carrier phase derived Doppler measurement, because they are determined over a very small time interval (Serrano et al., 2004a). Since the carrier phase derived Doppler shift is computed over a longer time span than the raw one, the random noise is averaged and suppressed. Therefore, the very smooth velocity estimates in low dynamic environments can be obtained from carrier phase derived Doppler measurements if there are no undetected cycle slips (Serrano et al., 2004b).

In this section, the principle of GNSS Doppler velocity determination will be described based on raw Doppler measurements generated by the GNSS receiver and Doppler measurements derived from the GNSS carrier phase measurements.

7.2.1 Velocity Determination Based on GNSS Raw Doppler Observations

The GNSS raw Doppler shift, which is caused by the relative motion between the receiver and the satellite, is the measurement of the phase rate (Cannon et al., 1997) directly estimated from the Phase Lock Loop (PLL) output (Szarmes et al., 1997; Borio et al., 2009). In a first approximation, the Doppler shift D between the GNSS satellite s and receiver r at the frequency channel j can be written as (cf. Eq. (2.3))

$$D_{r,j}^{s} = f_j^s - f_{r,j}^s = \frac{V_{\rho_r^s}}{c} f_j^s = \frac{V_{\rho_r^s}}{\lambda_j^s}, \tag{7.1}$$

where f denotes the frequency of the GNSS carrier phase observation. $V_{\rho_r^s}$ is the radial velocity of the range between the satellite s and the receiver r. c denotes the speed of light in vacuum and λ is the wavelength. $D_{r,j}^s$ has a positive sign when the receiver and the transmitter approach each other and a negative sign when they move away from each other. Eq. (7.1) for the observed Doppler shift scaled to range rate is given by

$$V_{\rho_r^s} = \lambda_j^s \cdot D_{r,j}^s = \dot{\rho}_r^s + c \cdot (d\dot{t}_r - d\dot{t}^s) + \varepsilon, \tag{7.2}$$

where the derivatives with respect to time are indicated by a dot. $\dot{\rho}$ stands for the geometric range rate between the satellite and receiver. $d\dot{t}_r$ and $d\dot{t}^s$ denote the receiver clock drift and satellite clock drift, respectively. ε is the effect of the observational noise and all non-modeled error sources, such as errors in multipath.

Most reference books suggest that the effects with low frequency properties such as ionosphere, troposphere, tide and multipath effects are so small that they can be neglected. However, according to Simsky and Boon (2003) and Zhang (2007), these errors should be taken into account in the precise velocity determination. It is well known that the GNSS observables have errors and biases that are spatially and temporally correlated. Differential GNSS techniques provide an efficient solution to account for the correlated errors and biases, since many un-modelled errors may be significantly reduced by the differencing process (Zhang et al., 2006). Therefore, similarly to the Double Difference (DD) GNSS positioning (cf.

Section 4.2), the DD GNSS velocity determination is applied in this study for precise velocity estimation.

Assuming the radial velocity equation of the range of the reference station r and the kinematic station k to a common satellite q can be written as

$$e_r^q V_r^q = \lambda_j D_{r,j}^q - c \cdot (d\dot{t}_r - d\dot{t}^q) + \varepsilon_r^q \tag{7.3}$$

and

$$e_k^q V_k^q = \lambda_j D_{k,j}^q - c \cdot (d\dot{t}_k - d\dot{t}^q) + \varepsilon_k^q \, , \tag{7.4}$$

where e is the direction cosine of the satellite and receiver. V_r^q denotes the radial velocity of the range between the satellite q and the reference station r with

$$V_r^q = V^q - V_r = \sqrt{(\dot{x}^q - \dot{x}_r)^2 + (\dot{y}^q - \dot{y}_r)^2 + (\dot{z}^q - \dot{z}_r)^2} \, , \tag{7.5}$$

where $\left(\dot{x}^q, \dot{y}^q, \dot{z}^q\right)$ denotes the velocity vector of the satellite q and $\left(\dot{x}_r, \dot{y}_r, \dot{z}_r\right)$ denotes the velocity vector of the reference station r.

Forming a single difference, the satellite clock drift $d\dot{t}^q$ can be cancelled out by

$$e_k^q V_k^q - e_r^q V_r^q = \lambda_j (D_{k,j}^q - D_{r,j}^q) - c(d\dot{t}_k - d\dot{t}_r) + \Delta\varepsilon_{k,r}^q \, . \tag{7.6}$$

The single difference for another satellite p at the signal frequency i is

$$e_k^p V_k^p - e_r^p V_r^p = \lambda_i (D_{k,i}^p - D_{r,i}^p) - c(d\dot{t}_k - d\dot{t}_r) + \Delta\varepsilon_{k,r}^p \, . \tag{7.7}$$

The DD equation for two single difference equations of the satellites p and q can be written as

$$e_k^p V_k^p - e_r^p V_r^p - e_k^q V_k^q + e_r^q V_r^q = \lambda_i (D_{k,i}^p - D_{r,i}^p) - \lambda_j (D_{k,j}^q - D_{r,j}^q) + \nabla\Delta\varepsilon_{k,r}^{p,q} \, , \tag{7.8}$$

where the differential receiver clock drift cancels. Since $V_k^p = V^p - V_k$, $V_r^p = V^p - V_r$, $V_k^q = V^q - V_k$ and $V_r^q = V^q - V_r$, Eq. (7.8) can be rewritten as done by Wang and Xu (2011) by

$$-e_k^{p,q} V_k + e_r^{p,q} V_r + e_{k,r}^p V^p - e_{k,r}^q V^q = \nabla\Delta D_{k,r}^{p,q} + \nabla\Delta\varepsilon_{k,r}^{p,q} \, , \tag{7.9}$$

where $\nabla\Delta D_{k,r}^{p,q} = \lambda_i (D_{k,i}^p - D_{r,i}^p) - \lambda_j (D_{k,j}^q - D_{r,j}^q)$ and $e_k^{p,q} = e_k^p - e_k^q$ etc. The velocity of the reference station V_r is zero, the velocity of the satellites V^p and V^q can be obtained from the GNSS precise ephemerides or broadcast ephemerides with an analytical differentiation of the position parameter equations. In order to achieve a solution at the mm/s level, satellite positions have to be known better than 10 m (Serrano et al., 2004a). Therefore, the velocity DD observation equation for the kinematic station k can be given as

$$-e_k^{p,q} V_k = \nabla\Delta D_{k,r}^{p,q} - e_{k,r}^{p} V^{p} + e_{k,r}^{q} V^{q} + \nabla\Delta\varepsilon_{k,r}^{p,q} . \tag{7.10}$$

The precise velocity estimation of the kinematic station can be directly obtained by the classic LS adjustment if Doppler observations from more than four GNSS satellites have been measured (cf. Section 3.2.1).

7.2.2 Velocity Determination Based on Doppler Observations Derived from GNSS Carrier Phase Measurements

Every GNSS receiver measures Doppler shifts. However, this is primarily used as an intermediate process to obtain accurate carrier phase measurements. Thus, some receivers output raw Doppler shift measurements and some do not output any at all. In the absence of raw Doppler shift, the carrier phase derived Doppler shift can be used (Zhang et al., 2005). It can be obtained either by differencing carrier phase observations in the time domain, normalizing them with the time interval of the differenced observations or by fitting a curve to successive phase measurements, using polynomials of various orders (Serrano et al., 2004a).

At present, the first order central difference is one of the most popular methods for obtaining the virtual Doppler observation (Cannon et al., 1997; Bruton et al., 1999; Serrano et al., 2004a; Wang and Xu, 2011). Based on the fundamental GNSS carrier phase observation equation, cf. Eq. (2.2), the carrier phase derived Doppler observation is obtained by

$$\dot{\varphi}_t = \frac{1}{2}\left(\frac{\varphi_{t+\delta t} - \varphi_t}{\delta t} + \frac{\varphi_t - \varphi_{t-\delta t}}{\delta t} \right) = \frac{\varphi_{t+\delta t} - \varphi_{t-\delta t}}{2\delta t} , \tag{7.11}$$

where t is the observation time and δt is the data sample interval. $\dot{\varphi}_t$ is the variation rate of the original carrier phase observation φ_t, namely the carrier phase derived Doppler observation.

The resulting observation equation for the velocity determination is

$$\lambda_j \dot{\varphi}_{r,j}^{q} = e_r^q V_r^q + c \cdot (d\dot{t}_r - d\dot{t}^q) + \dot{T}_r^q - \dot{I}_{r,j}^q + \dot{\varepsilon}_{r.j}^q , \tag{7.12}$$

where $\dot{T}$ and $\dot{I}$ denote the tropospheric and the ionospheric delay rate, respectively. $\dot{\varepsilon}$ represents un-modeled effects, modeling error and measurement error rate for carrier phase observations. Since the DD velocity determination is used, the error rates of $\dot{T}$, $\dot{I}$ and $\dot{e}$ can be summarised as $u_r^q = \dot{T}_r^q - \dot{I}_{r,j}^q + \dot{\varepsilon}_{r.j}^q$ (Serrano et al., 2004b).

The raw Doppler velocity DD observation equation Eq. (7.10) can be replaced by the carrier phase derived Doppler observation equation

$$-e_k^{p,q}V_k = \nabla\Delta\dot{\varphi}_{k,r}^{p,q} - e_{k,r}^{p}V^{p} + e_{k,r}^{q}V^{q} + \nabla\Delta u_{k,r}^{p,q}\,. \tag{7.13}$$

The precise velocity estimation of the kinematic station can be directly obtained by the classic LS adjustment if the carrier phase derived Doppler observations from more than four GNSS satellites are available (cf. Section 3.2.1).

The carrier phase derived Doppler observation is an average variation rate of the carrier phase observation φ during a time interval of $2\delta t$, rather than the instantaneous variation rate of φ at the epoch time t. However, the functional model for the raw Doppler observation is stricter than that of the carrier phase derived Doppler measurement. Therefore, the velocity results of the raw Doppler observations are more reliable than those of carrier phase derived Doppler observations in the high dynamic environments.

7.3 Velocity Determination Based on GNSS Integration and Robust Estimation

In order to improve the accuracy and the reliability of the velocity determination, the algorithms of GNSS integration based on Helmert's variance component estimation (VCE) and robust estimation are applied in GNSS Doppler velocity determination as well.

The accuracy, availability and reliability of GNSS Doppler velocity determination are very dependent on the number of GNSS Doppler observations, especially in high dynamic environments. A possible way to increase the number of observations is to use GNSS multi-constellation observations. Therefore the GNSS integration is applied in GNSS Doppler velocity determination as well. The principle of GNSS integration based on Helmert's VCE has been discussed in Chapter 6. The performance and the comparison of the application of this principle in GNSS Doppler velocity determination will be given in detail here.

The carrier phase derived Doppler observation is a measurement of the mean velocity between observation epochs which means that their random noise is averaged and lowered. However, the performance of such Doppler data is strongly dependent on the quality of the carrier phase observation. Cycle slips and gaps are unavoidable in GNSS processing. Usually, cycle slips can be detected and edited, but sometimes the undetected cycle slips still exist. Cycle slip detection in kinematic applications is difficult because of the increased dynamics induced by the platform motion of the remote antenna (Cannon et al., 1997). In particular, the occurrences of carrier cycle slips and gaps cause a significant degradation of the accuracy of the GNSS application. When undetected cycle slips exist in GNSS observations, outliers will appear in carrier phase derived Doppler observations, resulting in incorrect velocity determination. Therefore, the outliers must be eliminated. To minimize the impact of observation outliers on the estimates, the robust estimation approach is applied here for the GNSS velocity determination. The principle of robust estimation is discussed in Section 4.4. The performance and the comparison of the application of robust estimation in GNSS carrier phase derived Doppler velocity determination will be given in detail.

7.4 Experiment and Analysis

After the implementation of the algorithms for GNSS Doppler velocity determination, some practical tests were given carried out for a static as well as a kinematic case. Thereby, actually measured GNSS data of the GEOHALO project were used to validate the developed method in this study and the importance of a precise velocity determination for airborne gravimetry is discussed.

7.4.1 Static Experiment

In order to test the accuracy and reliability of the algorithms and software in a static data experiment, the static GNSS observation data of the reference stations REF6 and RENO from the GEOHALO flight on June 6, 2012 were randomly selected for testing. The distance of this baseline is about 605 km. The hardware types of all receivers and antennas are the same as in the experiment of Section 4.3.2 (cf. Table 4.2). The selected data contain GPS and GLONASS observations with a sampling rate of 1 Hz. REF6 was selected as the reference station. The station RENO was processed by the HALO_GNSS software as in a low dynamic environment. Since this test was carried out for a static station, the velocity results were compared with the expected zero velocity as the truth. The following five schemes were compared.

Scheme 1: The raw Doppler observations of GPS single system were used.

Scheme 2: The raw Doppler observations of GLONASS single system were used.

Scheme 3: The raw Doppler observations of GPS and GLONASS integration were used. The robust estimation is applied to remove outliers.

Scheme 4: The carrier phase derived Doppler observations of GPS and GLONASS integration were used.

Scheme 5: The carrier phase derived Doppler observations of the integrated GPS and GLONASS were used. The robust estimation is applied to remove outliers.

The comparative results are given in Figures 1-5 and Table 7.1.

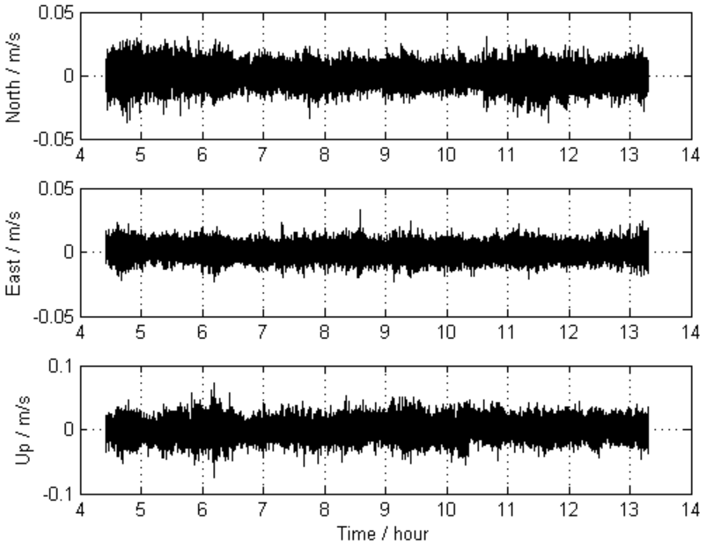

Figure 7.1: The velocity from raw GPS Doppler observations at the static station RENO on June 6, 2012 (scheme 1)

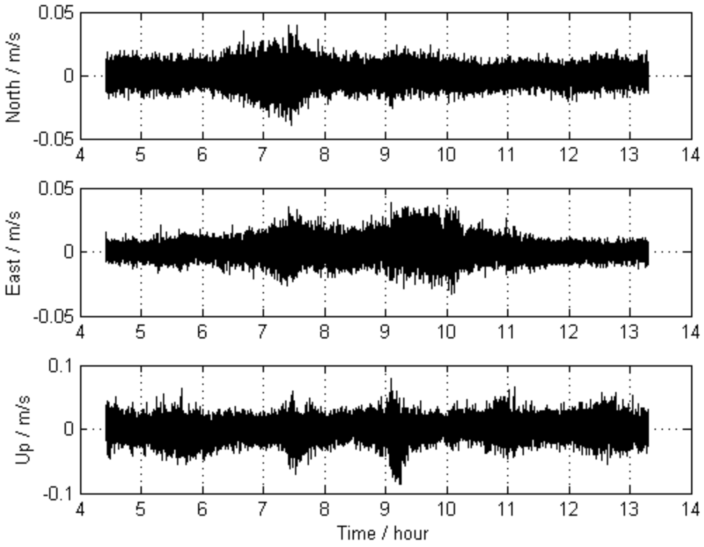

Figure 7.2: The velocity from raw GLONASS Doppler observations at the static station RENO on June 6, 2012 (scheme 2)

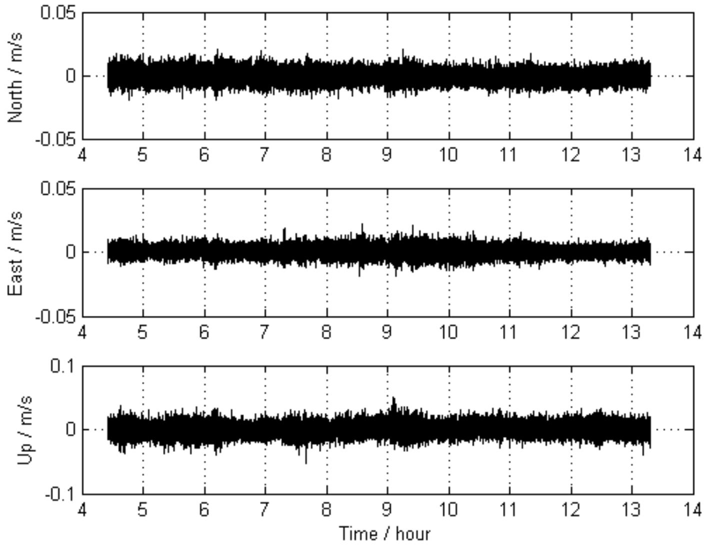

Figure 7.3: The velocity from the integrated raw GPS and GLONASS Doppler observations at the static station RENO on June 6, 2012 (scheme 3)

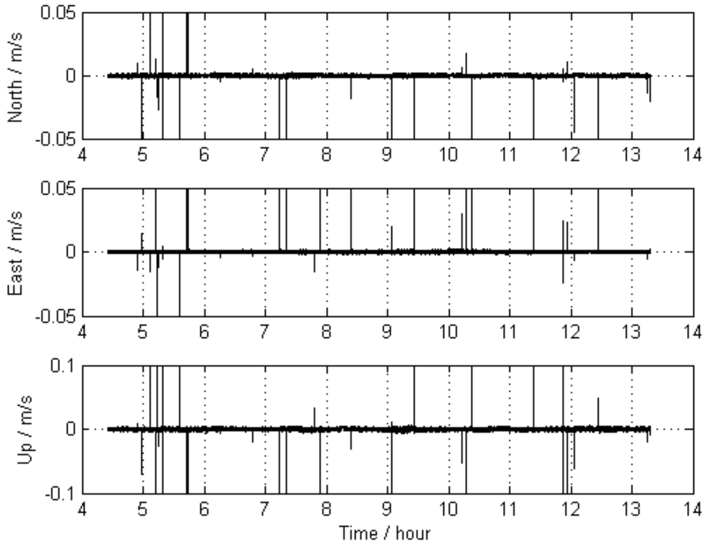

Figure 7.4: The velocity from the integrated GPS and GLONASS carrier phase derived Doppler observations on June 6, 2012 for the static station RENO, without the usage of the robust estimation (scheme 4)

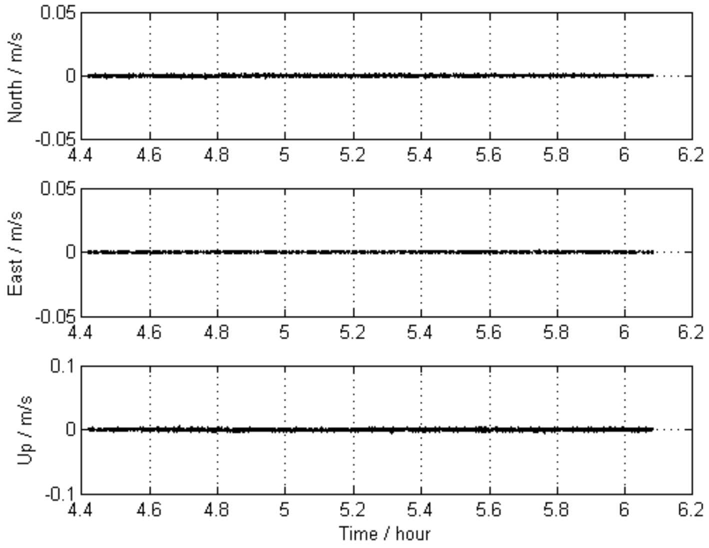

Figure 7.5: The velocity from GPS and GLONASS integrated carrier phase derived Doppler observations on June 6, 2012 for the static station RENO, with the usage of the robust estimation (scheme 5)

Table 7.1: The statistical results of the velocity determination (static experiment) for the station RENO in the schemata 1-5 (Unit: mm/s)

Scheme		**Directions**	**Min**	**Max**	**Mean**	**RMS**
1	Raw Doppler G (GPS)	North	-37.3	30.3	0.3	7.1
		East	-22.7	32.8	0.6	5.2
		Up	-74.1	72.3	0.7	12.7
2	Raw Doppler R (GLONASS)	North	-39.1	40.0	-0.1	6.6
		East	-33.1	33.8	1.6	6.7
		Up	-86.6	78.3	0.3	14.1
3	Raw Doppler Robust estimation G+R (Helmert weights)	North	-19.7	21.0	0.3	4.6
		East	-18.6	21.7	-0.6	3.7
		Up	-52.1	50.0	0.8	9.1
4	Carrier Phase G+R (1:1 weights)	North	-276.3	171.0	-0.3	3.7
		East	-83.6	360.5	0.1	5.0
		Up	-485.0	328.5	0.0	6.7
5	Carrier Phase Robust estimation G+R (Helmert weights)	North	-3.1	2.7	0.2	0.6
		East	-2.7	2.5	0.0	0.5
		Up	-7.6	6.3	0.0	1.5

The described static experiment illustrates the effectiveness, repeatability and stability of the proposed method using static data. The obtained results show the following:

(1) In the case of GPS-only, the accuracy of the velocity determination using the raw Doppler data can achieve about 1 cm/s in the low dynamic environment.

(2) The accuracy of the velocity determination based on raw GLONASS-only Doppler data is a little bit lower than the GPS-only accuracy. The combination of GPS and GLONASS based on Helmert's VCE is better than their respective use as single systems and improves the accuracy and reliability.

(3) In the case of the velocity determination using the carrier phase derived Doppler data, the undetected cycle slips influence considerably the velocity results. After the application of the robust estimation, the velocity outliers caused by the undetected cycle slips can be controlled as well.

(4) The highly accurate and very smooth velocity results in low dynamic environments can be obtained by the carrier phase derived Doppler measurements if there are no undetected cycle slips. The accuracy of the velocity determination for the carrier phase derived Doppler data can achieve about 1 mm/s in low dynamic environments.

7.4.2 Kinematic Experiment

The kinematic GNSS data of the GEOHALO flight on June 6, 2012 were selected for this test. These are the same data as used in Section 6.4. The same kinematic stations are selected. AIR5 and AIR6 are mounted on the front and back parts of the HALO aircraft, respectively (cf. Figure 4.5). The reference station REF6 was installed by GFZ next to the runway of the DLR airport in Oberpfaffenhofen. The station RENO located in the Italy region was selected as the second reference station because it includes raw Doppler observations. The hardware types of all receivers and antennas are the same as in the experiment in Section 4.3.2 (cf. Table 4.2). The selected data contain GPS and GLONASS observations, and the sampling rate is 1 Hz.

Figure 7.6 shows the HALO aircraft trajectory as latitude, longitude and height components on June 6, 2012. The two significant humps on the height curve correspond to crossing the Alps.

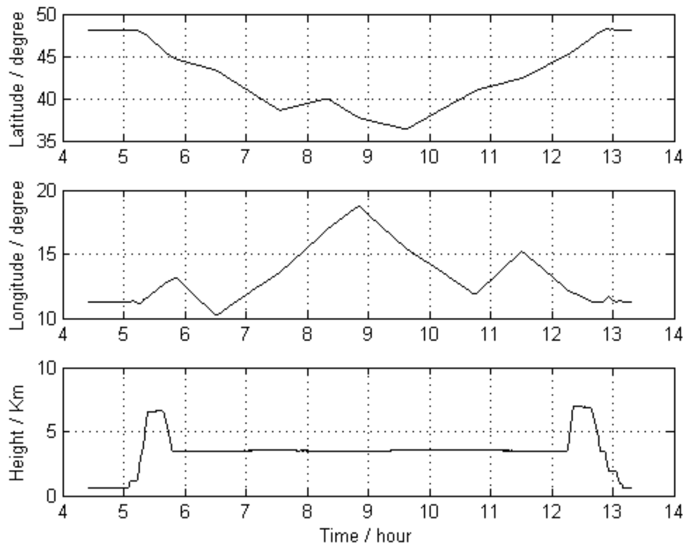

Figure 7.6: The components for the flight trajectory of the HALO aircraft on June 6, 2012

The velocity and the acceleration of this HALO aircraft flight are shown in Figure 7.7 and Figure 7.8, respectively.

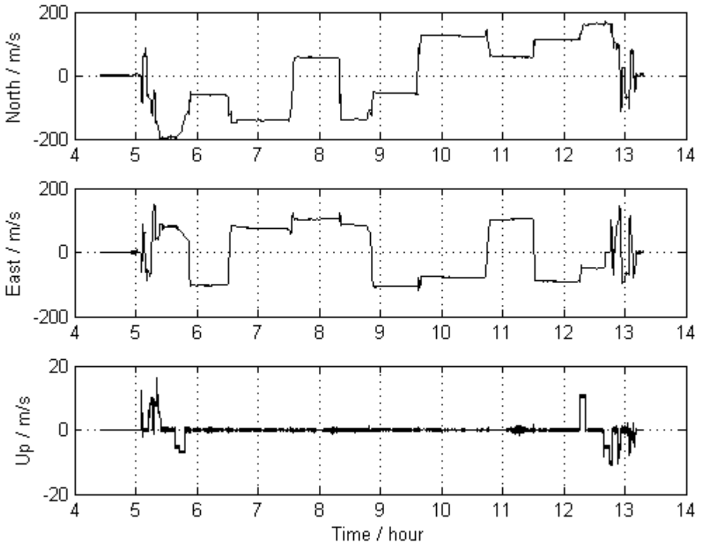

Figure 7.7: The velocity components for the flight of the HALO aircraft on June 6, 2012

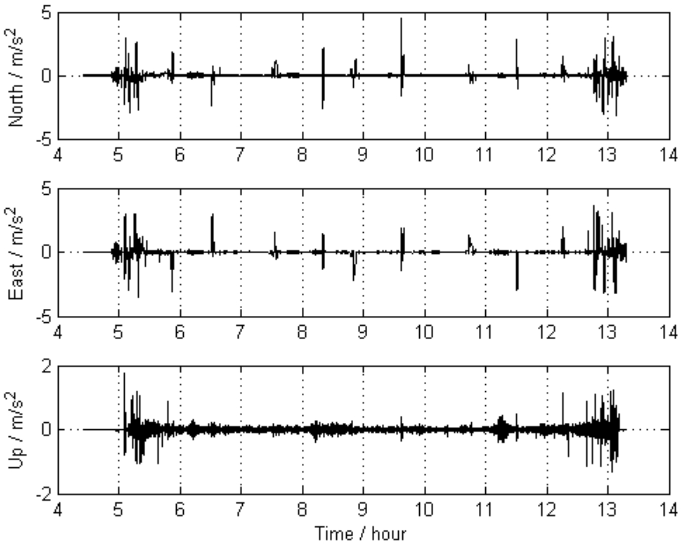

Figure 7.8: The acceleration components for the flight of the HALO aircraft on June 6, 2012

The GNSS Doppler velocity determination was done using the HALO_GNSS software which was developed at GFZ in the frame of this thesis. The IGS precise ephemeris (Kouba, 2009b) were chosen and the GPS and GLONASS satellite elevation angle was limited to 10°. The number of GPS, GLONASS and GPS+GLONASS satellites is shown in Figure 7.9 as blue, green and red line, respectively.

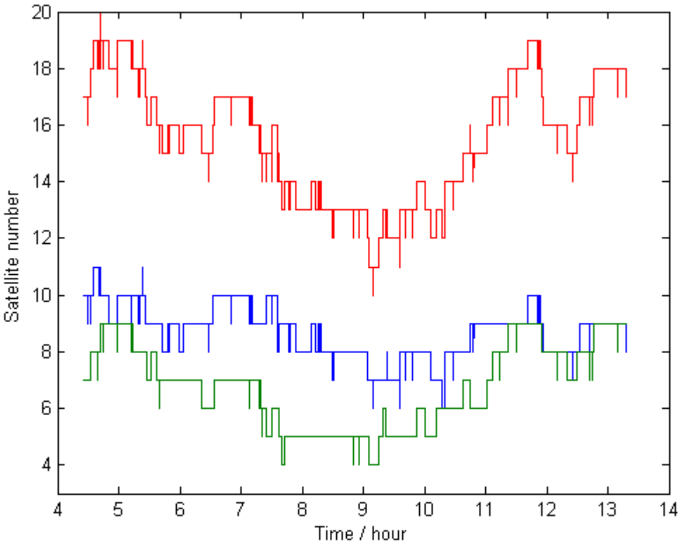

Figure 7.9: The number of selected satellites of GPS (blue line), GLONASS (green line) and GPS+GLONASS (red line)

In order to investigate the capability of the elaborated approach based on the Doppler velocity determination, the velocity results of the kinematic stations AIR5 and AIR6 were obtained by the HALO_GNSS software using the multiple reference stations REF6 and RENO. Therefore, five experimental schemes are designed.

Scheme 1: The raw Doppler observations of GPS single system were used.

Scheme 2: The raw Doppler observations of GLONASS single system were used.

Scheme 3: The raw Doppler observations of GPS and GLONASS integration were used. The robust estimation is applied to remove outliers.

Scheme 4: The carrier phase derived Doppler observations of GPS and GLONASS integration were used.

Scheme 5: The carrier phase derived Doppler observations of GPS and GLONASS integration were used. The robust estimation is applied to remove outliers.

Since it is very difficult to obtain an absolutely true velocity value of the moving highly dynamic platform, an internal comparison and a cross-validation are performed. The differences of the velocity estimates between two kinematic stations AIR5 and AIR6 are shown in Figure 7.10. The jumps in Figure 7.10 are caused by the velocity and acceleration changes (cf. Figure 7.7 and Figure 7.8) when a sudden change of the aircraft's status occurred, such as takeoff, landing, braking, turning and accelerating, etc.

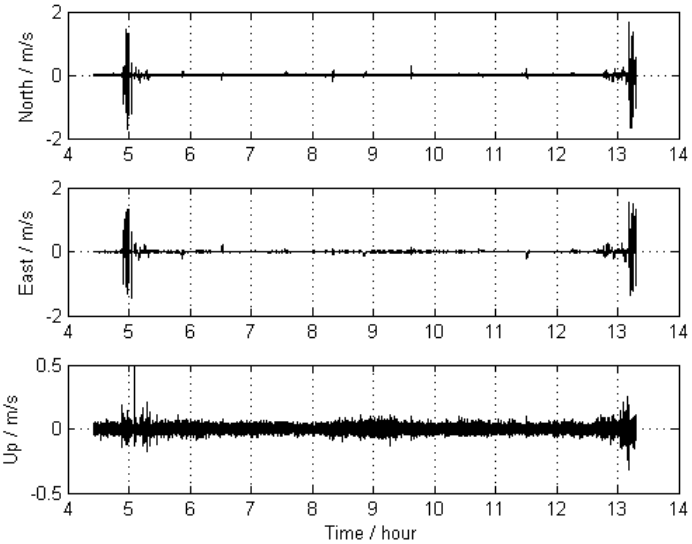

Figure 7.10: The differences of the velocity estimates between AIR5 and AIR6

However, when the aircraft is flying straight and smoothly, the difference of the velocity results between AIR5 and AIR6 should be theoretically zero. This assumption can be used to check the internal precision of the velocity determination. Therefore, the velocity results for the second straight and smoothly period of this flight from 6:40:00 am to 7:24:00 am (cf. Figure 7.7 and Figure 7.8) were selected for this evaluation. The comparison of the results between AIR5 and AIR6 for the GPS-only scheme 1, the GLONASS-only scheme 2 and the scheme 3 of the GPS and GLONASS integration are shown in Figure 7.11, Figure 7.12 and Figure 7.13, respectively. The statistical results of these cases are given in Table 7.2.

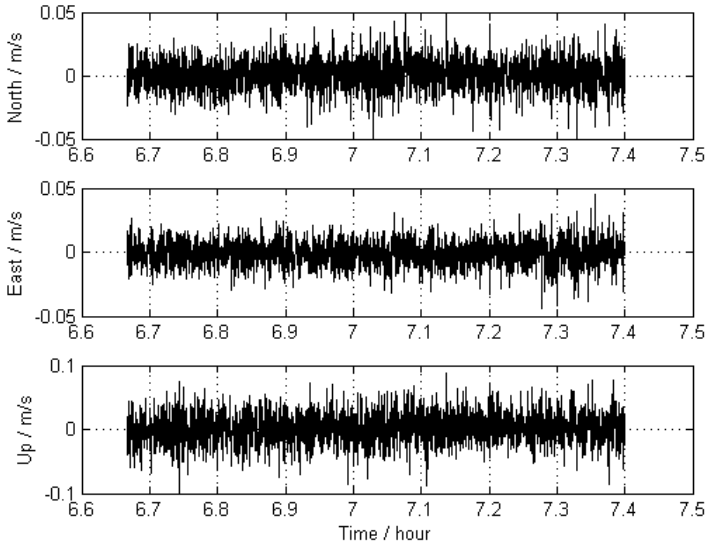

Figure 7.11: The difference of the GPS-only velocity results between AIR5 and AIR6 in the period of a straight smooth flight (scheme 1)

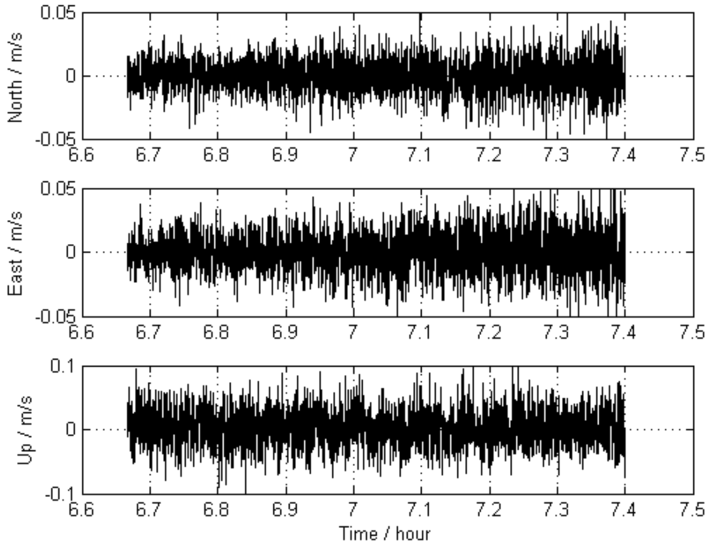

Figure 7.12: The difference of the GLONASS-only velocity results between AIR5 and AIR6 in the period of a straight smooth flight (scheme 2)

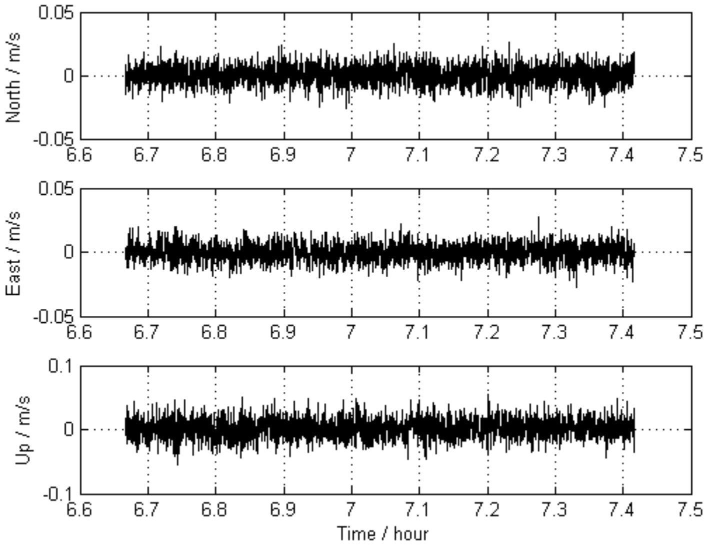

Figure 7.13: The difference of the velocity results using the integrated GPS and GLONASS between AIR5 and AIR6 in the period of a straight smooth flight (scheme 3)

Table 7.2: Statistical results for the velocity determination in the kinematic experiment for schemata 1-3 (Unit: mm/s)

Scheme		Directions	Min	Max	Mean	RMS
1	Raw Doppler G(GPS)	North	-61.4	74.2	0. 9	12.2
		East	-44.3	44.7	-1.1	9.8
		Up	-113.2	87.6	1.6	23.5
2	Raw Doppler R(GLONASS)	North	-50.3	49.8	0.3	13.5
		East	-81.1	62.6	-0. 3	15.9
		Up	-136.0	110.3	2.9	29.4
3	Raw Doppler Robust estimation G+R (Helmert weights)	North	-26.6	25.9	0. 3	7.6
		East	-27.2	28.0	0.4	6.9
		Up	-55.6	54.7	1.8	15.3

The aforementioned results show the following: The raw GNSS Doppler observations can be used to estimate the precise velocity of a highly dynamic aircraft and the conclusion is the same as in the recent literature. The precision of the velocity determination based only on the GLONASS is a little bit worse than for GPS-only. The precision of the velocity determination using the integrated GPS and GLONASS data based on Helmert's VCE is better than taking a single GNSS system.

Theoretically, the difference between different velocity solutions for the same kinematic station should be zero as well. This assumption can be used to check the internal precision of the velocity determination. For the kinematic station AIR5, the velocity results for the carrier phase derived Doppler observations for scheme 4 and 5 were compared with its velocity results based on the raw Doppler data of scheme 3 (integrated GPS and GLONASS data). The comparative results are shown in Figure 7.14 and Figure 7.15, respectively. The related statistic results are given in Table 7.3.

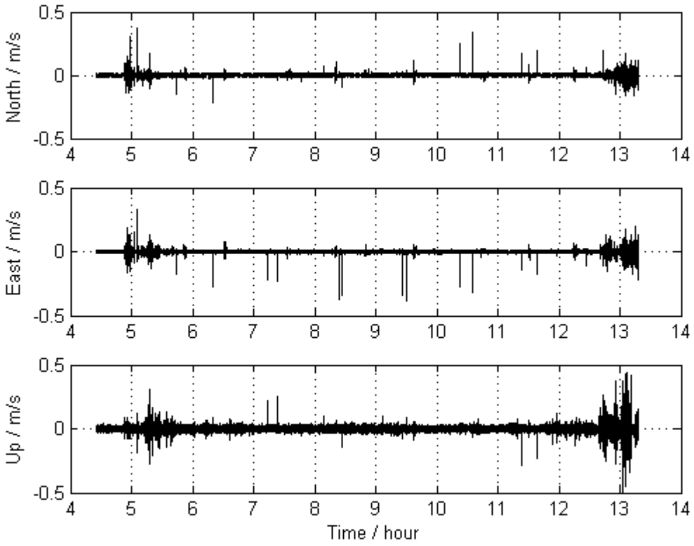

Figure 7.14: The differences between the estimated velocities for the raw Doppler observations and for the carrier phase derived Doppler at station AIR5 without the usage of the robust estimation (integrated GPS and GLONASS data)

The comparison results show clearly the inability of the carrier phase derived Doppler velocity determination in a high dynamic environment: There are many remaining jumps in Figure 7.14 which might be caused by undetected cycle slips and high dynamic environments. After the application of the robust estimation, the number of outliers due to undetected cycle slips can be obviously reduced (cf. Figure 7.15). But the impact of the highly dynamic motion still exists in the velocity determination of the carrier phase derived Doppler observations, because these data are average variation rates of the carrier phase observations φ during a time interval of $2\delta t$ which are more disturbed than the instantaneous variation rate of the raw Doppler data of φ at the epoch time t (cf. Section 7.2.2). The large spikes in Figure 7.15 correspond to the sudden changes of the state of the aircraft (cf. Figure 7.7 and Figure 7.8).

Therefore, the velocity results for a high dynamic environment based on the raw Doppler observations are more suitable than those based on carrier phase derived Doppler observations.

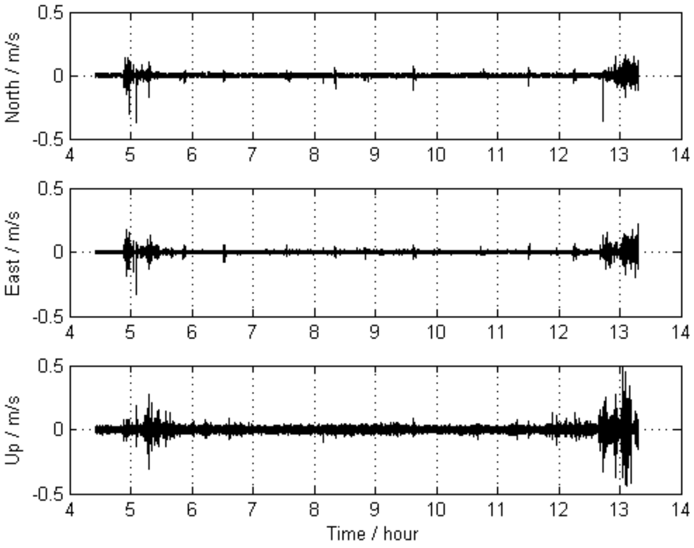

Figure 7.15: The differences between the estimated velocities for the raw Doppler observations and for the carrier phase derived Doppler at station AIR5 by applying the robust estimation (integrated GPS and GLONASS data)

Table 7.3: The statistical results of scheme 4 and 5 as plotted in figures 7.14 and 7.15 (Unit: mm/s)

Scheme		**Directions**	**Min**	**Max**	**Mean**	**RMS**
4	Carrier Phase G+R (1:1 weights)	North	-212.1	367.2	0. 4	13.2
		East	-381.4	330.9	-0. 6	14.9
		Up	-606.9	438.2	0. 1	26.6
5	Carrier Phase Robust estimation G+R (Helmert weights)	North	-367.0	156.4	-0. 4	12.7
		East	-330.7	216.0	0. 4	12.8
		Up	-439.3	605.9	-0. 1	26.2

7.4.3 Importance of Precise Velocity Determination for Airborne Gravimetry

The precise velocity information is one of the most critical issues in the application of GNSS results in airborne gravimetry. It is necessary for deriving the vertical component of the kinematic acceleration of the platform. This acceleration is used to separate the gravitational signal from the disturbing kinematic vertical accelerations affecting the airborne platform (cf. Section 1.2.1).

As seen from Table 7.2 and Table 7.3 the accuracy of the determined vertical velocity is about 2 cm/s. In order to investigate whether this accuracy is sufficient for the above purpose, the vertical accelerations should be computed from these velocity values. In order to illustrate the problem, one track flown on the first day (June 6, 2012) of the GEOHALO mission was chosen and the vertical acceleration was computed by numerical differentiation. The velocity was calculated from raw Doppler observations (cf. Section 7.4.2). A part of the used velocity data (second track of the named flight day) is given in the bottom plot in Figure 7.8. The resulting kinematic vertical acceleration of the HALO aircraft is shown in Figure 7.16. The result is given in units as usual in gravimetry $1\,\mathrm{mGal} = 10^{-5}\ \mathrm{m/s^2}$, and seems to have a strong noise component. Taking into account 1) that the resolution of the airborne gravity measurements lies in the order of magnitude of 1 mGal, and 2) that the expected gravity signal along such a track of 300-400 km length might vary maximally only in the range of several hundred mGal, the oscillations between -15000 and +15000 mGal as seen in Figure 7.16 seem to imply that such a result for the kinematic accelerations cannot be used at all. However, this conclusion is overhasty. The accelerations measured by an airborne gravimeter itself show also such strong oscillations. But when using a low-pass filter, these oscillations can be decomposed into a feasible signal and a disturbing high-frequency noise.

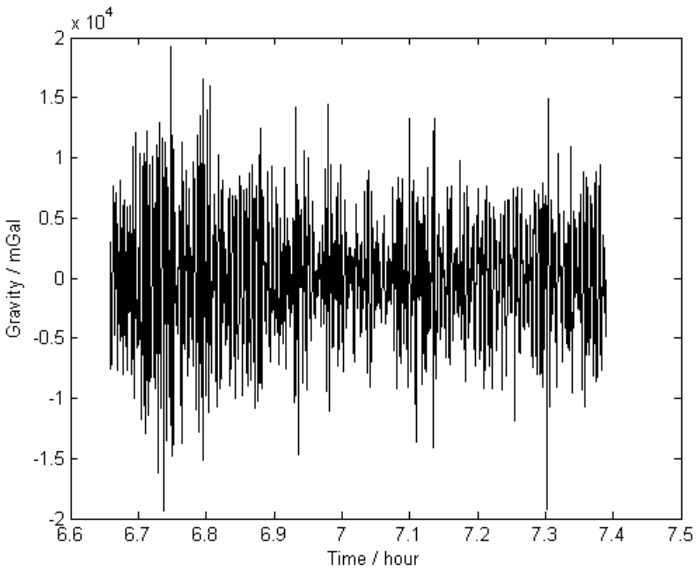

Figure 7.16: Vertical kinematic acceleration of the HALO aircraft as calculated directly from GNSS observations

Therefore, in order to obtain a feasible signal for the disturbing kinematic vertical acceleration (Brozena et al., 1989; Bruton et al., 1999; Kreye and Hein, 2003), the same low-pass filter should be applied to the vertical accelerations derived from the GNSS based vertical velocities. For this a low-pass filter with a cut-off wavelength of 300 seconds has been applied in the frequency domain (using Fast Fourier Transform). This cut-off wavelength corresponds to what is typically used in aerogravimetry. The resulting filtered kinematic accelerations for the respective GEOHALO track (produced by Dr. Franz Barthelmes, GFZ) are shown in Figure 7.17 as the black curve. The values are of an expected realistic order of magnitude (several mGal) and are usable to separate the huge disturbing kinematic accelerations affecting the airborne platform.

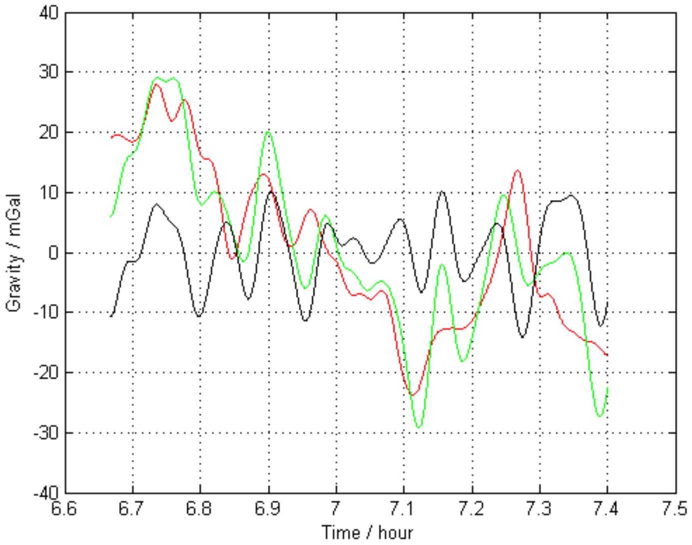

Figure 7.17: The black curve is the GNSS-based disturbing vertical kinematic accelerations of the HALO aircraft after the application of a low-pass filter to the noisy result as displayed in Figure 7.16. The red curve is a reference gravity signal computed from the global gravity field mode EIGEN-6C4 minus normal-gravity. The green curve is the CHEKAN measure vertical acceleration with all corrections except of that from GNSS.

In Figure 7.17, the black curve is the GNSS-based signal of the disturbing vertical kinematic accelerations of the HALO aircraft after the application of a low-pass filter to the noisy result displayed in Figure 7.16. The green curve is the gravity signal of the CHEKAN gravimeter including all corrections but without that from GNSS. The red curve denotes the gravity signal of the global gravity field model EIGN-6C4 minus normal-gravity, which is here used to check the gravity results. The statistical results of the comparison between the CHEKAN signal (green curve) and that of the reference gravity field model (red curve) are given in Table 7.4.

The final gravity signal at the HALO trajectory can be obtained by separating the GNSS-based disturbing kinematic accelerations of the HALO aircraft from the CHEKAN measured vertical acceleration. This is shown in Figure 7.18 as blue curve. The statistical results of the comparison between final gravity signal and the reference gravity field model is given in Table 7.3. The comparison of Figure 7.17, Figure 7.18 and Table 7.4 shows the need and the importance of GNSS for airborne gravimetry very significantly. This verification has been done by the colleagues from GFZ who are dealing with airborne gravitmetry since the processing of the CHEKAN airborne gravity data itself and the computation of the final gravity signal by separation of the GNSS-based disturbing kinematic accelerations are not subject of this thesis.

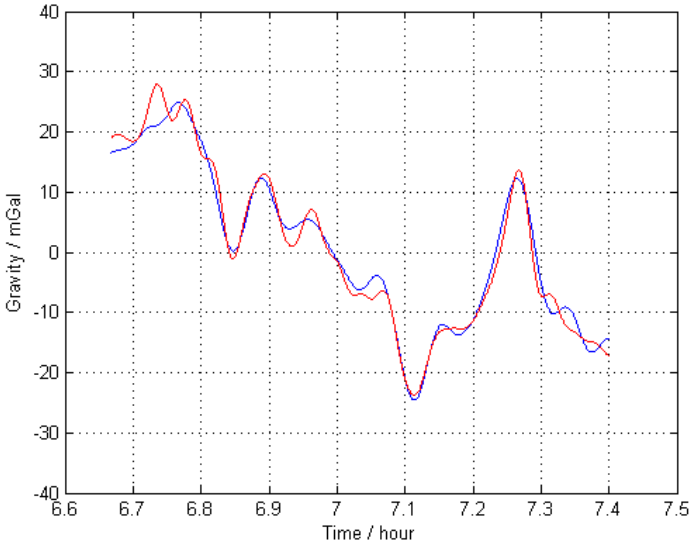

Figure 7.18: The final gravity signal (blue curve) compared with the reference gravity field model EIGEN-6C4 (red curve)

Table 7.4: The statistic results of the comparison between the calculated airborne gravity signal and the reference gravity field mode EIGEN-6C4 (unit: mGal)

Gravity signal type	Min	Max	Mean	RMS
CHEKAN measurements gravity (without GNSS modify)	-15.20	12.54	0.07	6.35
Final gravity (with GNSS modify)	-6.88	4.11	0.08	1.93

7.5 Conclusions

This chapter describes the principles of a series of options for the differential GNSS high accuracy velocity determination. Velocity was determined using Doppler observations obtained either by using the receiver generated raw Doppler shifts or by taking the carrier phase derived Doppler observations.

The best velocity results for low dynamic environments were obtained by applying the carrier phase derived Doppler observations. The velocity results for the raw Doppler observations are more reliable than those of the carrier phase derived Doppler measurements in high dynamic environments, since the carrier phase derived Doppler observation is a measure of the mean velocity between observation epochs. But they are usually noisier than the velocity results of the carrier phase derived Doppler observations because they are determined over a very short time interval.

The accuracy, availability and reliability of GNSS Doppler velocity determination are strongly dependent on the number of GNSS Doppler observations as well, especially in high dynamic environments. Therefore, the GNSS integration based on Helmert's VCE is applied in GNSS Doppler velocity determination. The accuracies obtained from both the kinematic and the static experiments have been improved in this way.

Cycle slips and gaps are unavoidable in any application of GNSS. Undetected cycle slips usually exist in GNSS observations and cause outliers in the carrier phase derived Doppler observations. This gives incorrect results for the GNSS velocity determination. Applying the robust estimation, the outliers can be removed.

8 Software Development and Application

8.1 Introduction

In order to fulfill the actual requirements of airborne as well as shipborne gravimetry on GNSS precise position and velocity determination, a software system (HALO_GNSS) for precise kinematic GNSS trajectory and velocity determination for kinematic platforms has been developed. In this software, the algorithms as proposed in this thesis were implemented. In order to evaluate the effectiveness of the proposed algorithms and the HALO_GNSS software, this software was applied both in airborne and shipborne gravimetry projects of GFZ Potsdam.

In this chapter, the characteristics, the overall design and the structure of the HALO_GNSS software are outlined. The applications of the kinematic GNSS algorithm and software are introduced briefly.

8.2 HALO_GNSS Software Development

The HALO_GNSS software is a high-precision GNSS kinematic position and velocity determination software for scientific research, developed by the author at GFZ during his study on this thesis. The purpose of this software is to test and evaluate the algorithms as introduced in the previous chapters and to process the GNSS data for airborne and shipborne gravimetry projects. All results presented in this thesis were obtained by using this HALO_GNSS software.

The HALO_GNSS software has been developed in the programming language FORTRAN under a Linux operating system by applying the algorithms as described in this thesis and by learning a lot from the previous HALO_GPS software, which is a GPS single system positioning software for single baselines, developed by Wang et al. (2010) at GFZ too. Furthermore, the development of HALO_GNSS was inspired by the famous software MFGsoft (Xu, 2004) and some subroutines were adopted from the GAMIT software (Herring et al., 2010).

8.2.1 Characteristics of the HALO_GNSS Software

The most important characteristics of the HALO_GNSS software are:

(1) Multiple GNSS data can be processed. Currently, the GPS-only, GLONASS-only and GPS/GLONASS integration are available.

(2) Precise position information of a kinematic platform can be obtained. It allows the kinematic positioning with an accuracy of 1-2 cm.

(3) Precise velocity information of a kinematic platform can be obtained as well. It allows the velocity determination with the accuracy of about 1 cm/s using raw and about 1 mm/s using carrier phase derived Doppler observations. This accuracy seems to be far too low for the direct application in airborne gravimetry. However, the major error component is the high-frequency noise, so that a useful signal can be recovered by low-pass filtering.

(4) Multiple reference stations and multiple kinematic stations can be processed together.

(5) Robust estimation is applied to control the influence of outliers in GNSS position and velocity determination.

(6) An a priori distance constraint among multiple kinematic stations on the same platform is used to improve the accuracy and reliability of GNSS kinematic positioning.

(7) A common troposphere zenith delay parameter for multiple kinematic stations mounted on the same platform is employed to improve the accuracy and reliability of GNSS kinematic positioning as well.

(8) Helmert's variance components estimation is used to reasonably adjust the weights and the contributions among multiple GNSS systems.

(9) This software can be applied in many fields, such as static and kinematic environments, airborne and shipborne platforms, small and large regions, and in particular in ultra-high-altitude, ultra-long-range and high dynamic environments.

8.2.2 Structure Design of Software

Most of GPS software systems consist generally of three basic components (e.g. Xu (2004); Herring et al. (2010); Wang et al. (2010)): Firstly, the functional library provides all possibly needed physical models, algorithms and tools for use. Secondly, the data platform prepares all possibly needed data for use. Finally, the data processing core forms the observation equations, accumulates them and solves the problem (Xu, 2007, p. 219).

The HALO_GNSS software developed as part of this study was designed in accordance with this general structure. The specific structure design of the HALO_GNSS software is given in Figure 8.1.

The main steps outlined in Figure 8.1 are:

(1) **Start**: Running the command "./HALO_GNSS".

(2) **Reading user command file**: The most important parameters for controlling the running of the software are set.

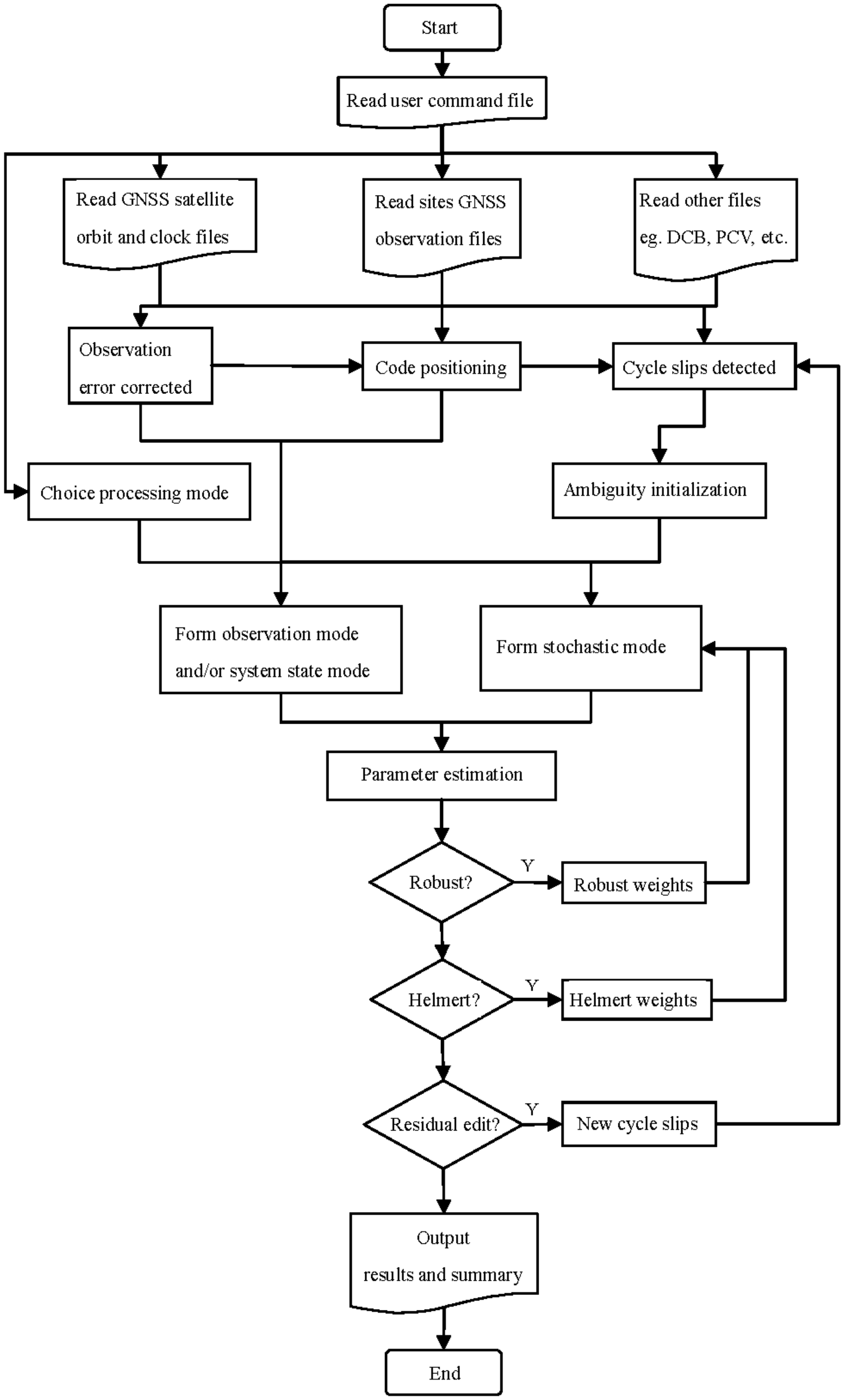

Figure 8.1: The GNSS data processing flowchart of HALO_GNSS software

(3) **Reading GNSS satellite orbit and clock files**, e.g. for the GPS and GLONASS (cf. Section 1.2.3).

(4) **Read sites GNSS observation files**, which include the GNSS data of reference stations and kinematic stations, GPS and GLONASS, code, carrier phase and Doppler observations, etc. (cf. Section 2.2).

(5) **Read other files** if necessary, such as the Differential Code Biases (DCB) corrections, antenna Phase Centre Offsets (PCO) and Phase Centre Variations (PCV), etc. (cf. Section 2.4).

(6) **Observation error corrected,** reduce the errors resp. disturbances contained in the GNSS measurements if possible, e.g. antenna offset, atmospheric delay and DCB corrections, etc. (cf. Section2.4).

(7) **Code positioning**: Data pre-processing for the elevation angles of the satellites, detection of bad data and initial position of sites (cf. Section 4.2).

(8) **Cycle slips detection** and **Ambiguity initialization** which is necessary only for the carrier phase data processing.

(9) **Choice processing mode**: Depended on the user command file, the processing mode will be chosen, such as position or velocity determination, initialization of matrix and all unknown parameters (cf. Chapter 3-7).

(10) **Form the observation mode and/or system state mode**, e.g. the DD observation equations of carrier phase, pseudorange or Doppler observations; system state mode (needed in Kalman filter only) (cf. Section 4.2, 4.3, 5.2, 5.3, 5.4, 6.2, 7.2 and 7.3).

(11) **Form stochastic mode**. e.g. the covariance matrix of observations, the covariance matrix of Kalman filter system noise, and the covariance matrix of predicted state vector (cf. Section 4.4, 6.3 and 7.3).

(12) **Parameter estimation** (cf. Section 3.2 and 3.3).

(13) **Robust** estimation to control the outliers if necessary (cf. Section 4.4 and 7.3).

(14) **Helmert**'s variance components estimation for multiple GNSS systems if necessary (cf. Section 6.3 and 7.3).

(15) **Residual edit**. If necessary, set **New cycle slips** for the carrier phase observation depend on the value of observation residuals.

(16) **Output results and summary** files.

(17) **End** of program.

The Operation instructions and the detailed description of the major functional modules of the HALO_GNSS software will be given in a separate technical report "HALO_GNSS software user manual", which is not included in this thesis.

8.3 HALO_GNSS Software Applications

The HALO_GNSS software can be applied in different fields, such as static and kinematic environments, airborne and shipborne platforms, small and large regions, in particular in ultra-high-altitude, ultra-long-range and high dynamic environments. The applications for the GNSS kinematic position and velocity determination using the HALO_GNSS software are introduced briefly in this section; some of them have been already presented in the former chapters.

8.3.1 Lake Müritz Shipborne Gravimetry

This experiment was performed by GFZ section 1.2 from October 25 to 27, 2011 at Lake Müritz in Mecklenburg-Vorpommern, northern Germany (cf. Figure 8.2). One of the main purposes of this survey was testing the newly purchased gravimeter CHEKAN. The other purpose was to study the precise GNSS kinematic positioning for gravimetry.

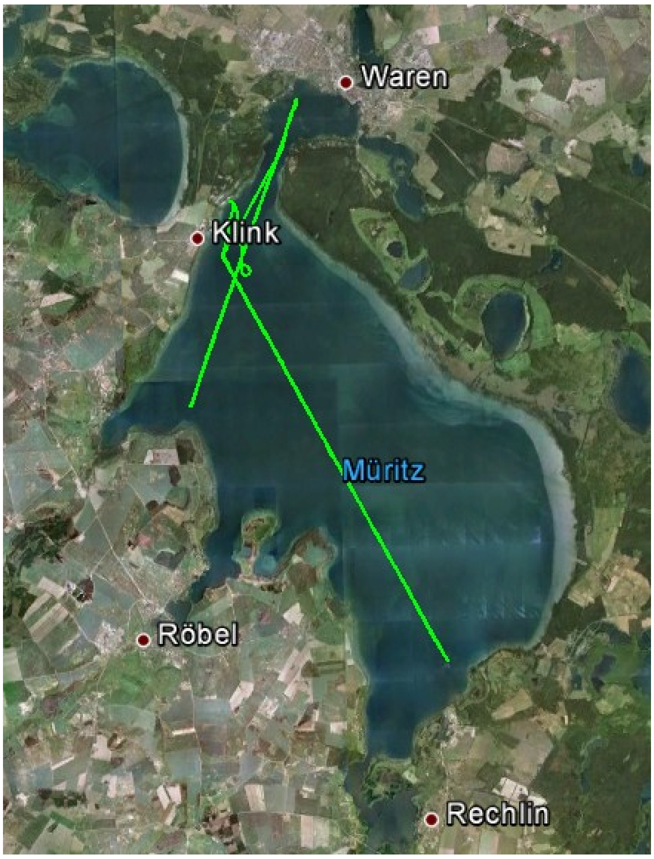

Figure 8.2: The Lake Müritz location and the tracks of the ship

During the experiment, three days of measurements were performed on this lake. Seven dual-frequency GNSS receivers were used, two of them were set up on the shore as reference stations and another five were mounted on the ship, see Figure 8.3. The HALO_GNSS software has been applied for GNSS data processing. The tracks of the ship on Lake Müritz are shown in Figure 8.2 as green lines.

Figure 8.3: The ship used and the position of GNSS receiving equipments

8.3.2 The GEOHALO Italy Mission

On June 6, 8, 11 and 12, 2012, the GEOHALO mission was carried out over the Italian area and adjacent regions of the Mediterranean, starting and ending at the DLR in Oberpfaffenhofen Germany (cf. Figure 8.4).

More details about the GEOHALO aircraft flight mission are given in Section 1.2.2. The main goals of the GEOHALO mission were: GNSS reflectometry (Semmling et al., 2013; Semmling et al., 2014), airborne gravimetry (Petrovic et al., 2013), magnetometry and laser altimetry (Scheinert et al., 2013). GNSS precise position and velocity determination plays an important role in the whole mission, since all remote sensing instruments and measuring devices are fixed on the same kinematic platform. Therefore, the accurate state information of the kinematic platform is a key factor of the successful implementation of the entire mission.

The HALO_GNSS software was used to provide the precise position and velocity information of the HALO aircraft (cf. Figure 5.1) for the whole mission. The flown HALO tracks (red lines) are shown in Figure 8.4. Some of GNSS data of the GEOHALO-flight have been compared and analyzed in detail in sections 4.3.2, 4.4.2, 6.4.1 and 7.4.1 in order to demonstrate the approach proposed in this thesis.

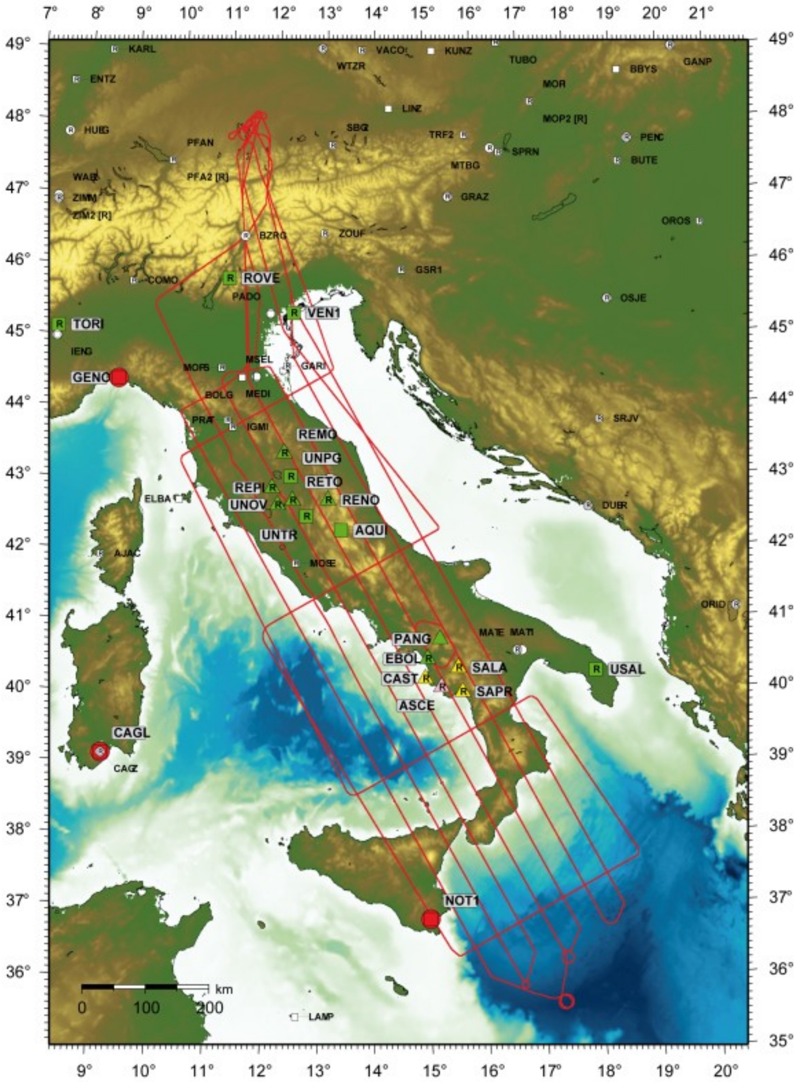

Figure 8.4: The GEOHALO mission tracks (red lines) and GNSS reference stations (red and green dots) in Italy

8.3.3 Lake Constance Shipborne Gravimetry

The Lake Constance (Bodensee in German) campaign was performed by GFZ and BKG from October 23 to 26, 2012. This lake is located in Germany, Switzerland and Austria near the Alps (Figure 8.5). One of the main purposes of this survey was to obtain gravity information of the Lake Constance area. The other purpose was to study the precise GNSS kinematic positioning for gravimetry.

During this campaign, four days of measurements were accomplished on the lake and the HALO_GNSS software has been applied for the GNSS data processing. The tracks of the ship run on Lake Constance are shown in Figure 8.5 as green lines.

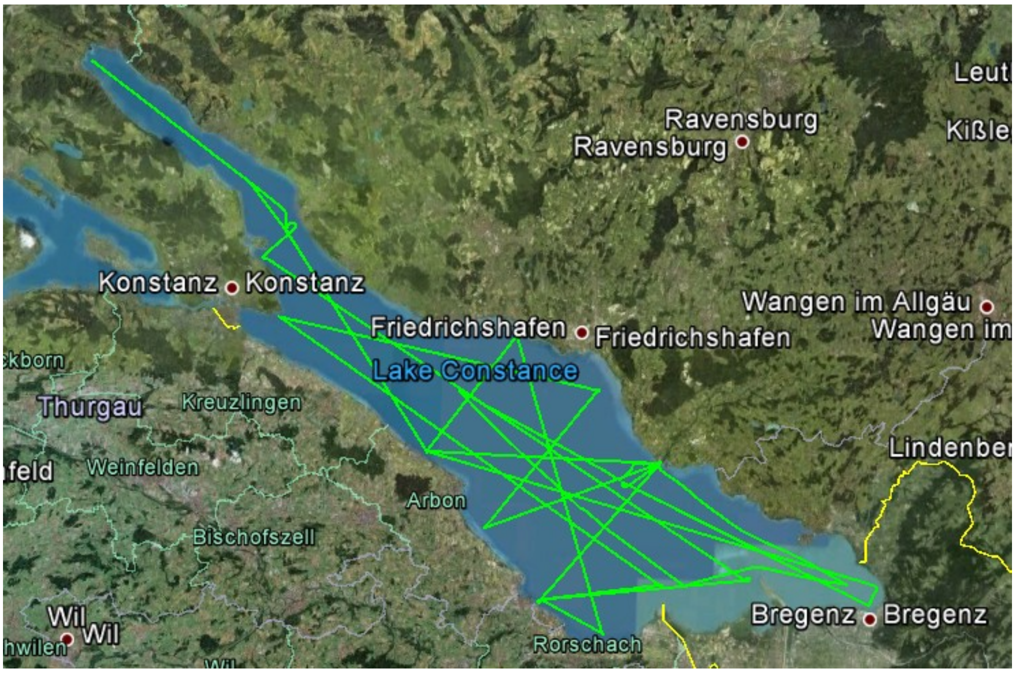

Figure 8.5: All tracks of the ship in the Constance Lake in October 2012

8.3.4 Baltic Sea Shipborne Gravimetry

From June 18 to 27, 2013, ten days of GNSS and gravimetric data of a shipborne gravimetric campaign were collected by GFZ and BKG in Baltic Sea (Ostsee in German) near Greifswald, Germany (cf. Figure 8.6). The main purpose of this survey was to obtain gravity information of the Baltic Sea near Greifswald, Germany and to study the precise GNSS kinematic positioning for gravimetry.

The HALO_GNSS software was used to provide the precise position information of the ship for the whole campaign. The tracks of the ship during this campaign are shown in Figure 8.6 (green lines). The GNSS data of the first day of the Baltic Sea gravimetric campaign have been compared and analyzed in detail in Section 5.5 to demonstrate the approach proposed in chapter 5.

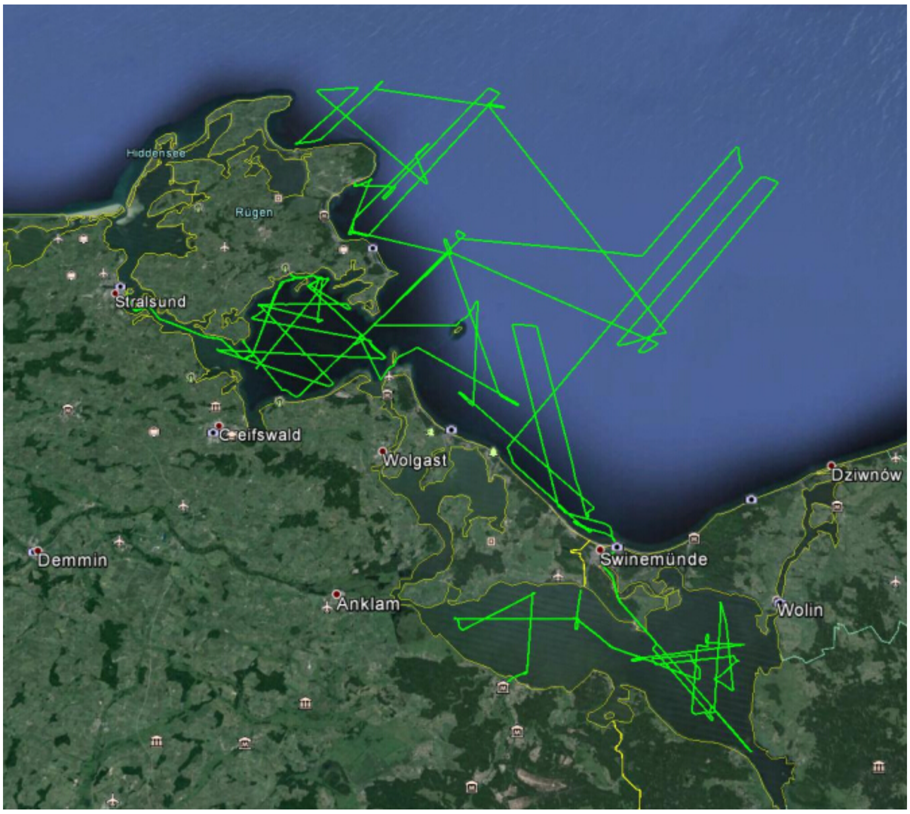

Figure 8.6: All tracks of the ship in the Baltic Sea gravimetric campaign in June 2013

8.4 Conclusions

A high-precision kinematic GNSS position and velocity determination software HALO_GNSS has been developed based on algorithms proposed in this thesis, to meet the actual requirements of airborne as well as shipborne gravimetry. The characteristics, overall design and the structure of the HALO_GNSS software were outlined firstly. In order to evaluate the effectiveness of the proposed algorithms and the HALO_GNSS software, this software has been applied in several airborne and shipborne gravimetry projects of GFZ Potsdam. The applications of the kinematic GNSS algorithm and software are introduced briefly.

9 Summary and Future Work

9.1 Summary

The GNSS kinematic position and velocity determination plays an important role in airborne gravimetry. Development, analysis and investigation of a reliable GNSS algorithms and software for kinematic highly precise GNSS data analysis for airborne gravimetry are the major goals of this research. It includes investigation of the estimation algorithms, accuracy evaluation analysis, the development of the new methods of integrated GNSS kinematic position and velocity determination based on multiple reference stations and multiple kinematic stations, robust estimation, a priori distance constraints, a common tropospheric delay parameter, Helmert's variance components estimation, and software development and application. The core results and the specific contributions of this research can be summarized as follows.

The parameter estimation algorithms of least squares including the elimination of nuisance parameters as well as the two-way Kalman filter were applied in kinematic GNSS data post-processing to fulfill the high accuracy requirements of airborne gravimetry.

A specific accuracy and the reliability evaluation method for GNSS kinematic precise position determination has been applied in static and kinematic modes, for short as well as long baselines, and for low and high dynamics states. The receiver clock errors including the clock jumps were analyzed for highly dynamic GNSS precise positioning. It has been shown that the receiver clock error including clock jumps must be corrected for each measurement epoch.

A new approach using multiple reference stations based on an a priori constraint is addressed to increase the accuracy and reliability of GNSS precise kinematic positioning for the widely arranged GNSS stations. A robust estimation algorithm is used to suppress the impact of observation outliers on the trajectory estimates.

A new method of GNSS kinematic positioning based on multiple kinematic stations on the same platform with a priori distance constraints and the estimation of a common tropospheric delay parameter is developed. In this new method, the distances among the multiple GNSS antennas are known and used as a priori distance constraints to improve the accuracy and the reliability of the state estimates. Since the characteristics of the tropospheric delays in a small area are similar, a common tropospheric delay parameter has been set up for such multiple kinematic stations, which can enhance the accuracy and reliability of the state estimates.

A kinematic positioning method using the integration of multiple GNSS systems based on Helmert's variance components estimation is addressed to adjust the weights in a reasonable way in order to balance the contributions of multiple GNSS systems, and to improve the reliability and accuracy of GNSS kinematic positioning.

Velocities were determined using Doppler observations. For this purpose two kinds of Doppler data were used: 1) Receiver generated raw Doppler shift measurements or 2) Doppler data derived from the carrier phase measurements. The best velocity results for low dynamics were obtained by applying carrier phase derived Doppler observations. For high dynamic environments, the velocity results based on the raw Doppler shift measurements are more reliable than those derived from carrier phase data. A new approach for velocity determination based on the integration of multiple GNSS systems using Helmert's variance components estimation and the robust adjustment has been developed, which can significantly improve the accuracy of the results and control the influence of the outliers.

In order to fulfill the actual requirements of airborne and shipborne gravimetry on kinematic GNSS data analysis, a reliable and precise kinematic GNSS position and velocity determination software system (HALO_GNSS) has been developed based on the algorithms proposed in this thesis. This software can be applied for different purposes, such as static and kinematic processing, airborne and shipborne platforms, small and large regions, in particular in ultra-high-altitude, ultra-long-range and high dynamic environments. It allows the GNSS kinematic positioning with an accuracy of 1-2 cm and GNSS velocity determination with the accuracy of about 1 cm/s using raw and about 1 mm/s using carrier phase derived Doppler observations. The accuracy of these results for velocity is high enough in GNSS field, but it cannot be used directly in airborne gravimetry. Because of the high-frequency characters of the noise, a sufficiently accurate vertical acceleration results can be obtained by applying a low-pass filter.

These contributions have been supported by numerical results and tested under different conditions. All results presented in this thesis were obtained by using the HALO_GNSS software.

9.2 Future Work

As a continuation of this research, a variety of points can be suggested. Among them are those described in the following.

The integration of the raw Doppler velocity into the Kalman filter for an improved position determination should be investigated. The precise instantaneous velocity of a kinematic platform can be obtained by raw Doppler observation. This velocity information should be used to improve the classic application of the Kalman filter. The observation mode, system mode and a priori covariance of classic Kalman filter will be improved and enhanced, and will be more reliable and accurate.

The methodology presented in this study can be in principle applied to any GNSS system, such as GPS, GLONASS, BDS and Galileo, etc. However, here in this study resp. in the developed HALO_GNSS software only the two GNSS systems GPS, GLONASS and their integration/combination were adopted. The exercise of mathematical models and processing methodologies for integrated systems is valuable since it is capable to identify crucial issues concerning the combination of any two or more GNSS positioning systems. Hence these experiences can be applied to other GNSS systems in order to integrate GPS with Galileo, GLONASS, BDS, or all the four together. This interesting topic requires further investigation and will probably improve the performance of GNSS position and velocity determination.

Since real-time methods play a more and more important role in GNSS applications, the precise GNSS kinematic position and velocity determination methods for large regions as studied in this thesis should be adopted in the future for real-time applications.

The attitude determination of a kinematic platform is an important issue for many scientific applications, like remote sensing and airborne gravimetry. The method of precise GNSS kinematic positioning based on multiple stations on the same platform as used in this thesis can be further developed and used for attitude determination.

In the algorithm of multiple reference stations, the weights of the observations from each reference station can be introduced depending on the lengths of the distance between the kinematic aircraft and the reference stations.

For the future, it is planned to use the HALO aircraft for airborne gravimetry in central Antarctica to close the “polar gap” of dedicated satellite gravity field missions (due to their non-polar orbit inclinations). But for the polar region Antarctica it’s expected that the specific constellation of the GNSS satellites and the sparse density of reference ground stations will cause significant erroneous biases in the altitude determination. Therefore, the development of new related algorithms is urgently needed to fulfill the requirements of HALO in the expected situation. Furthermore, the HALO data of laser altimetry could be used to compare and combine with the GNSS data.

References

Abdel-salam, M. A. 2005. *Precise point positioning using un-differenced code and carrier phase observations.* Ph.D Thesis, University of Calgary.

Al-Shaery, A., Lim, S. & Rizos, C. 2011. Investigation of different interpolation models used in Network-RTK for the virtual reference station technique. *Journal of Global Positioning Syetems,* 10**,** 136-148

Alberts, B. 2009. *Regional gravity field modeling using airborne gravimetry data,* Delft, NCG, Nederlandse Commissie voor Geodesie.

Angrisano, A., Gioia, C., Gaglione, S. & del Core, G. 2013. GNSS Reliability Testing in Signal-Degraded Scenario. *International Journal of Navigation and Observation,* 2013**,** 1-12

Askne, J. & Nordius, H. 1987. Estimation of tropospheric delay for microwaves from surface weather data. *Radio Science,* 22**,** 379-386

Bähr, H., Altamimi, Z. & Heck, B. 2007. *Variance component estimation for combination of terrestrial reference frames,* Univ.-Verlag Karlsruhe.

Baarda, W. 1968. A testing procedure for use in geodetic networks. *Publications on geodesy,* New Series, Vol. 2, No. 5, Delft

Baarda, W. 1976. Reliability and precision of networks. *In:* Eichhorn, G. (ed.) *VIIth International Course for Engineering Surveys of high precision.* Darmstadt, Germany.

Banville, S., Santerre, R., Cocard, M. & Langley, R. B. 2008. Satellite and receiver phase bias calibration for undifferenced ambiguity resolution. *Proc. ION NTM.*

BDS-ICD 2013. BeiDou Navigation Satellite System Signal In Space Interface Control Docoument. *Open Service Signal (Version 2.0).* Beijing: China Satellite Navigation Office.

BDS-OS-PS 2013. BeiDou Navigation Satellite System Open Service Performance Standard. *Version 1.0.* Beijing: China Satellite Navigation Office.

BDS. 2014. *BeiDou Navigation Satellite System* [Online]. Available: http://en.beidou.gov.cn/ [Accessed 03.02 2014].

Beser, J. & Parkinson, B. W. 1982. The application of NAVSTAR differential GPS in the civilian community. *Navigation,* 29**,** 107-136

Biacs, Z., Krakiwsky, E. & Lapucha, D. 1990. Reliability analysis of phase observations in GPS baseline estimation. *Journal of Surveying Engineering,* 116**,** 204-224

Bisnath, S. & Gao, Y. 2008. Current state of precise point positioning and future prospects and limitations. *Observing our changing earth.* Springer.

Black, H. & Eisner, A. 1984. Correcting satellite Doppler data for tropospheric effects. *Journal of Geophysical Research: Atmospheres (1984–2012),* 89**,** 2616-2626

Blewitt, G. 1989. Carrier phase ambiguity resolution for the Global Positioning System applied to geodetic baselines up to 2000 km. *Journal of Geophysical Research: Solid Earth (1978–2012),* 94**,** 10187-10203

Blewitt, G. 1990. An automatic editing algorithm for GPS data. *Geophysical Research Letters,* 17**,** 199-202

Blewitt, G., Melbourne, W., Bertiger, W., Dixon, T., Kroger, P., Lichten, S., Meehan, T., Neilan, R., Skrumeda, L. & Thornton, C. 1988. GPS geodesy with centimeter accuracy. *GPS-Techniques Applied to Geodesy and Surveying.* Springer.

Bock, Y. & Shimada, S. 1990. Continuously monitoring GPS networks for deformation measurements. *Global Positioning System: An Overview.* Springer.

Boehm, J. & Schuh, H. 2004. Vienna mapping functions in VLBI analyses. *Geophysical Research Letters,* 31

Bohm, J., Niell, A., Tregoning, P. & Schuh, H. 2006. Global Mapping Function (GMF): A new empirical mapping function based on numerical weather model data. *Geophysical Research Letters,* 33

Borio, D., Sokolova, N. & Lachapelle, G. 2009. Doppler measurements and velocity estimation: A theoretical framework with software receiver implementation. *ION/GNSS.* Savannah, Georgia.

Bossler, J. D., Goad, C. C. & Bender, P. L. 1980. Using the Global Positioning System (GPS) for geodetic positioning. *Bulletin géodesique,* 54**,** 553-563

Brozena, J., Mader, G. & Peters, M. 1989. Interferometric Global Positioning System: Three‐dimensional positioning source for airborne gravimetry. *Journal of Geophysical Research: Solid Earth (1978–2012),* 94**,** 12153-12162

Bruton, A. M., Glennie, C. L. & Schwarz, K. P. 1999. Differentiation for high-precision GPS velocity and acceleration determination. *GPS solutions,* 2**,** 7-21

Cannon, M. E., Lachapelle, G., Szarmes, M. C., Hebert, J. M., Keith, J. & Jokerst, S. 1997. DGPS kinematic carrier phase signal simulation analysis for precise velocity and position determination. *Navigation,* 44**,** 231-245

Chen, G. 1998. *GPS kinematic positioning for the airborne laser altimetry at Long Valley, California.* Ph.D Thesis, Massachusetts Institute of Technology.

Chen, G. & Herring, T. A. 1997. Effects of atmospheric azimuthal asymmetry on the analysis of space geodetic data. *Journal of Geophysical Research: Solid Earth (1978–2012),* 102**,** 20489-20502

Chen, W., Hu, C., Chen, Y., Ding, X. & Kwok, S. 2001. Rapid static and kinematic positioning with Hong Kong GPS active network. *ION GPS.*

Chen, W., Hu, C., Gao, S., Chen, Y., Ding, X. & Simon, C.-w. K. 2004. Absolute ionospheric delay estimation based on GPS PPP and GPS active network. *2004 International Symposium on GNSS/GPS.* Sydney, Australia.

Chen, X., Han, S., Rizos, C. & Goh, P. C. 2000. Improving real time positioning efficiency using the Singapore integrated multiple reference station network (SIMRSN). *Proceedings of the 13th International Technical Meeting of the Satellite Division of The Institute of Navigation (ION GPS 2000).*

Chu, F.-Y. & Yang, M. 2013. GPS/Galileo long baseline computation: method and performance analyses. *GPS Solutions,* 18**,** 1-10

Collins, J. P. & Langley, R. B. 1997. Estimating the residual tropospheric delay for airborne differential GPS positioning. *PROC ION GPS, INST OF NAVIGATION, ALEXANDRIA, VA,(USA), 1997,* 2**,** 1197-1206

Collins, P., Gao, Y., Lahaye, F., Héroux, P., MacLeod, K. & Chen, K. 2005. Accessing and processing realtime GPS corrections for precise point positioning—some user considerations. *Proceedings of ION GNSS 18th international technical meeting of the satellite division.* Long Beach, CA, US.

Collins, P., Lahaye, F., Heroux, P. & Bisnath, S. 2008. Precise point positioning with ambiguity resolution using the decoupled clock model. Fairfax, USA: ION GNSS

Crocetto, N., Gatti, M. & Russo, P. 2000. Simplified formulae for the BIQUE estimation of variance components in disjunctive observation groups. *Journal of Geodesy,* 74**,** 447-457

Dach, R., Hugentobler, U., Fridez, P. & Meindl, M. 2007. Bernese GPS software version 5.0. *Astronomical Institute, University of Bern.*

Dai, L., Han, S., Wang, J. & Rizos, C. 2001. A study on GPS/GLONASS multiple reference station techniques for precise real-time carrier phase-based positioning. *ION GPS 2001.* Salt Lake City, USA.

Dai, Z. 2013. *On GPS based Attitude Determination.* Ph. D, Universität Siegen.

Davis, J. L., Herring, T. A., Shapiro, I. I., Rogers, A. E. E. & Elgered, G. 1985. Geodesy by radio interferometry: Effects of atmospheric modeling errors on estimates of baseline length. *Radio science,* 20**,** 1593-1607

Deng, Z. 2012. *GPS Meteorology with Single Frequency Receivers.* Ph.D Thesis, University of Hannover.

Dixon, K. 2006. StarFire(TM): A Global SBAS for Sub-Decimeter Precise Point Positioning. *ION GNSS 19th International Technical Meeting of the Satellite Divesion.* Fort Worth, TX, USA: Proceedings of ION GNSS 2006.

Dixon, T. H. 1991. An introduction to the Global Positioning System and some geological applications. *Reviews of Geophysics,* 29**,** 249-276

DLR. 2013a. *HALO aircraft* [Online]. Available: http://www.dlr.de/dlr/en/desktopdefault.aspx/tabid-10658#gallery/6163 [Accessed 03.03 2014].

DLR. 2013b. *HALO Home* [Online]. Available: http://www.halo.dlr.de/ [Accessed 01.12 2013].

Dong, D. N. & Bock, Y. 1989. Global Positioning System network analysis with phase ambiguity resolution applied to crustal deformation studies in California. *Journal of Geophysical Research: Solid Earth (1978–2012),* 94**,** 3949-3966

Doppler, C. 1842. *Ueber das farbige Licht der Doppelsterne und einiger anderer Gestirne des Himmels,* Prag, Abh Kgl Bohm Ges Wissench.

Doran, H. E. 1992. Constraining Kalman filter and smoothing estimates to satisfy time-varying restrictions. *The Review of Economics and Statistics***,** 568-572

ESA. 2014. *Galileo General Introduction* [Online]. Available: http://www.navipedia.net/index.php/GALILEO_General_Introduction [Accessed 03.04 2014].

Förstner, W. 1979. Ein verfahren zur schätzung von varianz-und kovarianzkomponenten. *Allgemeine Vermessungsnachrichten,* 86**,** 446-453

Förstner, W. 1983. Reliability and discernability of extended Gauss-Markov models. *Deutsche Geodätische Kommission (DGK).* München, Report A 98:79-104

Förstner, W. 1987. Reliability analysis of parameter estimation in linear models with applications to mensuration problems in computer vision. *Computer Vision, Graphics, and Image Processing,* 40**,** 273-310

Fernandes, M. J., Pires, N., Lazaro, C. & Nunes, A. L. 2013. Tropospheric delays from GNSS for application in coastal altimetry. *Advances in Space Research,* 51**,** 1352-1368

Firuzabadì, D. & King, R. W. 2012. GPS precision as a function of session duration and reference frame using multi-point software. *GPS solutions,* 16**,** 191-196

Forsberg, R. & Olesen, A. V. 2010. Airborne gravity field determination. *In:* Xu, G. (ed.) *Sciences of Geodesy-I.* Heidelberg, London, New York: Springer.

Fotopoulos, G. & Cannon, M. E. 2001. An overview of multi-reference station methods for cm-level positioning. *GPS solutions,* 4**,** 1-10

Galas, R., Schöne, T., Cokrlic, M. & Semmling, M. 2013. On precise GNSS-based sea surface monitoring systems. *ELMAR, 2013 55th International Symposium.* IEEE.

Galileo-ICD 2010. European GNSS (Galileo) Open Service Signal in Space Interface Control Document. *2010.*

Ge, M., Douša, J., Li, X., Ramatschi, M., Nischan, T. & Wickert, J. 2012. A novel real-time precise positioning service system: Global precise point positioning with regional augmentation. *J. Glob. Position. Syst,* 11**,** 2-10

Ge, M., Gendt, G., Rothacher, M., Shi, C. & Liu, J. 2008. Resolution of GPS carrier-phase ambiguities in precise point positioning (PPP) with daily observations. *Journal of Geodesy,* 82**,** 389-399

Gelb, A. 1974. *Applied optimal estimation,* Cambridge, Massachusetts, and London, The MIT press.

Geng, J., Teferle, F. N., Meng, X. & Dodson, A. 2010. Kinematic precise point positioning at remote marine platforms. *GPS solutions,* 14**,** 343-350

Geng, J., Teferle, F. N., Meng, X. & Dodson, A. 2011. Towards PPP-RTK: Ambiguity resolution in real-time precise point positioning. *Advances in space research,* 47**,** 1664-1673

Genrich, J. F. & Bock, Y. 1992. Rapid resolution of crustal motion at short ranges with the Global Positioning System. *Journal of Geophysical Research: Solid Earth (1978–2012),* 97**,** 3261-3269

GFZ. 2013. *Terrestrial and Airborne Gravimetry* [Online]. Available: www.gfz-potsdam.de/en/research/organizational-units/departments/department-1/global-geomonitoring-and-gravity-field/topics/terrestrial-and-airborne-gravimetry/ [Accessed 31.01 2014].

Ghilani, C. D. 2010. *Adjustment computations: spatial data analysis*, John Wiley & Sons.

Grafarend, E., Kleusberg, A. & Schaffrin, B. 1980. An introduction to the variance-covariance component estimation of Helmert type. *Zeitschrift für Vermessungswesen,* 105**,** 161-180

Grejner-Brzezinska, D. A., Kashani, I., Wielgosz, P., Smith, D. A., Spencer, P. S., Robertson, D. S. & Mader, G. L. 2007. Efficiency and reliability of ambiguity resolution in network-based real-time kinematic GPS. *Journal of Surveying Engineering,* 133**,** 56-65

Grodecki, J. 1997. Estimation of variance-covariance components for geodetic observations and implications on deformation trend analysis. *Geodesy and Geomatics Engineering Technical Reports; 186,*

Haase, J., Murphy, B., Muradyan, P., Nievinski, F., Larson, K., Garrison, J. & Wang, K. N. 2014. First results from an airborne GPS radio occultation system for atmospheric profiling. *Geophysical Research Letters,*

Habrich, H. 2000. *Geodetic applications of the global navigation satellite system (GLONASS) and of GLONASS/GPS combinations,* Verlag des Bundesamtes für Kartographie und Geodäsie.

Han, S. 1997. Quality-control issues relating to instantaneous ambiguity resolution for real-time GPS kinematic positioning. *Journal of Geodesy,* 71**,** 351-361

Hannah, J. 2001. Airborne gravimetry: a status report. Dunedin: Department of Surveying, University of Otago.

He, K. & Xu, T. 2009. Kinematic Orbit Determination of GEO Satellite Based on Kalman filtering. *Journal of Geodesy and Geodynamics,* 29**,** 109-112 (In Chinese)

He, K. & Xu, T. 2011. Orbit determination of GEO satellite based on forward and backward Kalman filtering with elimination parameter. *Science of Surveying and Mapping,* 36**,** 53-55 (In Chinese)

Hein, G. W. 1995. Progress in airborne gravimetry: Solved, open and critical problems. *Proceedings of the IAG Symposium on Airborne Gravity Field Determination, IUGG XXI General assembly.* Boulder, Colorado, July.

Helmert, F. R. 1907. *Die Ausgleichungsrechnung nach der Methode der kleinsten Quadrate,* Leipzig, Berlin, BG Teubner.

Herring, T., King, R. & McClusky, S. 2010. GAMIT Reference Manual. GPS Analysis at MIT. *Release 10.4.* Massachussetts Institute Technology.

Herring, T. A., Davis, J. L. & Shapiro, I. I. 1990. Geodesy by radio interferometry: The application of Kalman filtering to the analysis of very long baseline interferometry data. *Journal of Geophysical Research: Solid Earth (1978–2012),* 95**,** 12561-12581

Hewitson, S. & Wang, J. 2006. GNSS receiver autonomous integrity monitoring (RAIM) performance analysis. *GPS Solutions,* 10**,** 155-170

Heyde, I., Barthelmes, F. & Scheinert, M. 2013. First Results of the aerogravity measurements during the geoscientific flight mission GEOHALO over Italy and the adjacent Mediterranean *EGU General Assembly 2013.* Vienna, Austria.

Hofmann-Wellenhof, B., Lichtenegger, H. & Wasle, E. 2008. *GNSS–global navigation satellite systems: GPS, GLONASS, Galileo, and more,* Wien, NewYork, Springer.

Hopfield, H. 1969. Two ‐ quartic tropospheric refractivity profile for correcting satellite data. *Journal of Geophysical research,* 74**,** 4487-4499

Huep, W. 1985. *Zur Positionsschätzung im gestörten KALMAN-Filter am Beispiel eines manövrierenden Wasserfahrzeuges.* Ph. D, Fachrichtung Vermessungswesen der Univ. Hannover.

IAC. 2014. *GLONASS Constellation Status* [Online]. Available: http://glonass-iac.ru/en/GLONASS/ [Accessed 02.04 2014].

Ifadis, I. 1986. The atmospheric delay of radio waves: Modeling the elevation dependence on a global scale. *Technical Report.* Gothenburg, Sweden: Chalmers University of Technology.

IGS. 2013. *IGS Products* [Online]. Available: http://igscb.jpl.nasa.gov/components/prods.html [Accessed 30 April 2014].

IGS. 2014. *The IGS Tracking Network* [Online]. Available: http://www.igs.org/network/complete.html [Accessed 12.02 2014].

InsideGNSS. 2010. *Russia to Put 8 CDMA Signals on 4 GLONASS Frequencies* [Online]. Available: http://www.insidegnss.com/node/1997 [Accessed 02.04 2014].

Janes, H., Langley, R. & Newby, S. 1991. Analysis of tropospheric delay prediction models: comparisons with ray-tracing and implications for GPS relative positioning. *Bulletin géodésique,* 65**,** 151-161

Jee, G., Lee, H. B., Kim, Y., Chung, J. K. & Cho, J. 2010. Assessment of GPS global ionosphere maps (GIM) by comparison between CODE GIM and TOPEX/Jason TEC data: Ionospheric perspective. *Journal of Geophysical Research: Space Physics (1978–2012),* 115

Jonkman, E. 1980. Doppler research in the nineteenth century. *Ultrasound in medicine & biology,* 6**,** 1-5

Julier, S. J. & LaViola, J. J. 2007. On Kalman filtering with nonlinear equality constraints. *Signal Processing, IEEE Transactions on,* 55**,** 2774-2784

Kalman, R. E. 1960. A new approach to linear filtering and prediction problems. *Journal of Fluids Engineering,* 82**,** 35-45

Kalman, R. E. & Bucy, R. S. 1961. New results in linear filtering and prediction theory. *Journal of Fluids Engineering,* 83**,** 95-108

Kim, D. & Langley, R. B. 2001. Instantaneous real time cycle-slip correction of dual-frequency GPS data. *Proceedings of the international symposium on kinematic systems in geodesy, geomatics and navigation.* Banff, Alberta, Canada.

Kim, H.-S. & Lee, H.-K. 2012. Elimination of Clock Jump Effects in Low-Quality Differential GPS Measurements. *Journal of Electrical Engineering & Technology,* 7**,** 626-635

Klobuchar, J. A. 1987. Ionospheric time-delay algorithm for single-frequency GPS users. *Aerospace and Electronic Systems, IEEE Transactions on***,** 325-331

Knight, N. L., Wang, J. & Rizos, C. 2010. Generalised measures of reliability for multiple outliers. *Journal of Geodesy,* 84**,** 625-635

Ko, S. & Bitmead, R. R. 2007. State estimation for linear systems with state equality constraints. *Automatica,* 43**,** 1363-1368

Koch, K. R. 1986. Maximum likelihood estimate of variance components. *Bulletin Gæodésique,* 60**,** 329-338

Koch, K. R. 1999. *Parameter estimation and hypothesis testing in linear models,* Springer.

Koch, K. R. 2013. Robust estimation by expectation maximization algorithm. *Journal of Geodesy,* 87**,** 107-116

Koch, K. R. & Kusche, J. 2002. Regularization of geopotential determination from satellite data by variance components. *Journal of Geodesy,* 76**,** 259-268

Koch, K. R. & Yang, Y. 1998. Robust Kalman filter for rank deficient observation models. *Journal of Geodesy,* 72**,** 436-441

Kouba, J. 2009a. A guide to using International GNSS Service (IGS) products. *International GNSS.* Ottawa: Geodetic Survey Division of Natural Resources Canada.

Kouba, J. 2009b. Testing of global pressure/temperature (GPT) model and global mapping function (GMF) in GPS analyses. *Journal of Geodesy,* 83**,** 199-208

Kouba, J. & Héroux, P. 2001. Precise point positioning using IGS orbit and clock products. *GPS solutions,* 5**,** 12-28

Kreye, C. & Hein, G. W. 2003. GNSS Based Kinematic Acceleration Determination for Airborne Vector Gravimetry-Methods and Results. *Proceedings of the ION GPS/GNSS 2003 Meeting.* Portland, Oregon.

Kubik, K. 1982. An error theory for the Danish method. *Symposium of Comm. III of ISP.* Helsinki.

Kusche, J. 2003. Noise variance estimation and optimal weight determination for GOCE gravity recovery. *Advances in Geosciences,* 1**,** 81-85

Kwon, J. H. & Jekeli, C. 2001. A new approach for airborne vector gravimetry using GPS/INS. *Journal of Geodesy,* 74**,** 690-700

Lachapelle, G. & Alves, P. 2009. Multiple reference station approach: overview and current research. *Journal of Global Positioning Syetems,* 1**,** 133-136

Lacoste, L. J. 1967. Measurement of gravity at sea and in the air. *Reviews of Geophysics,* 5**,** 477-526

Langley, R. B. 1999. Dilution of precision. *GPS world,* 10**,** 52-59

Leick, A. 2004. *GPS satellite surveying,* John Wiley & Sons.

Leick, A., Beser, J. & Rosenboom, P. 1998. Aspects of GLONASS carrier-phase differencing. *GPs Solutions,* 2**,** 36-41

Li, B., Feng, Y., Shen, Y. & Wang, C. 2010. Geometry‐specified troposphere decorrelation for subcentimeter real‐time kinematic solutions over long baselines. *Journal of Geophysical Research: Solid Earth (1978–2012),* 115

Li, B., Shen, Y., Feng, Y., Gao, W. & Yang, L. 2013. GNSS ambiguity resolution with controllable failure rate for long baseline network RTK. *Journal of Geodesy,* 88**,** 1-14

Li, D. 1985. *Theorie und Untersuchung der Trennbarkeit von groben Paßpunktfehlern und systematischen Bildfehlern bei der photogrammetrischen Punktbestimmung.* PhD thesis, Universität Stuttgart.

Li, D. 1989. A Thought of Optimization and Design of Geodetic Networks in Consideration of Accuracy and Reliability. *Festschrift Friedrich Ackermann zum 60. Geburtstag,*

Li, X., Ge, M., Douša, J. & Wickert, J. 2014. Real-time precise point positioning regional augmentation for large GPS reference networks. *GPS solutions,* 18**,** 61-71

Mader, G. L. 1999. GPS antenna calibration at the National Geodetic Survey. *GPS solutions,* 3**,** 50-58

Marreiros, J. P. R. 2012. *Kinematic GNSS precise point positioning.* Ph.D Thesis, University of Porto.

McCarthy, D. D. 1996. IERS Conventions (1996). *IERS Technical Note.*

Melbourne, W. G. 1985. The case for ranging in GPS-based geodetic systems. *In:* Goad, C. (ed.) *Proceedings of first International Symposium on Precise Positioning with the Global Positioning Systme.* Rockville, Maryland: U.S. Department of Commerce.

Mendes, V. B. & Langley, R. B. 1994. A comprehensive analysis of mapping functions used in modeling tropospheric propagation delay in space geodetic data. *Proceeding of the International Symposium on Kinematic Systems in Geodesy.* Banff, Alberta.

Mendes, V. B. & Langley, R. B. 1995. Zenith Wet Tropospheric Delay Determination Using Prediction Model: Accuracy Analysis. *Cartograpia e Cadastro,* 2**,** 41-47

Mendes, V. B. & Langley, R. B. 1998. Tropospheric zenith delay prediction accuracy for airborne GPS high-precision positioning. *Proceedings of The Institute of Navigation 54th Annual Meeting.*

Mercado, D. A., Flores, G., Castillo, P., Escareno, J. & Lozano, R. 2013. GPS/INS/optic flow data fusion for position and Velocity estimation. *Unmanned Aircraft Systems (ICUAS), 2013 International Conference on.* IEEE.

Mervart, L., Lukes, Z., Rocken, C. & Iwabuchi, T. 2008. Precise Point Positioning with ambiguity resolution in real-time. *Proceedings of ION GNSS.*

Mikhail, E. M. & Ackermann, F. E. 1976. Observations and least squares.

Mohamed, A. H. & Schwarz, K. P. 1999. Adaptive Kalman filtering for INS/GPS. *Journal of Geodesy,* 73**,** 193-203

Montenbruck, O., Hauschild, A., Steigenberger, P., Hugentobler, U., Teunissen, P. & Nakamura, S. 2013. Initial assessment of the COMPASS/BeiDou-2 regional navigation satellite system. *GPS solutions,* 17**,** 211-222

Moreno Monge, B. 2012. *Development of algorithms for the GNSS data processing: their application to the modernized GPS and Galileo scenarios.* Ph. D, Universidad Complutense de Madrid.

NAVCEN. 2014. *General Informaiton on GPS* [Online]. Available: http://www.navcen.uscg.gov/?pageName=GPSmain [Accessed 01.04 2014].

Niell, A. E. 1996. Global mapping functions for the atmosphere delay at radio wavelengths. *Journal of Geophysical Research,* 101**,** 3227-3246

Niell, A. E. 2001. Preliminary evaluation of atmospheric mapping functions based on numerical weather models. *Physics and Chemistry of the Earth,* 26**,** 475-480

NOAA. 2014a. *The GPS Control Segment* [Online]. Available: http://www.gps.gov/systems/gps/control/ [Accessed 01.04 2014].

NOAA. 2014b. *The GPS Space Segment* [Online]. Available: http://www.gps.gov/systems/gps/space/#generations [Accessed 01.04 2014].

OpeNaviGate. 2012. *GLONASS / GPS Integration* [Online]. Available: http://openavigate.blogspot.de/2012/01/glonass-gps-integration.html [Accessed 08.05 2014].

Parkinson, B. 1996. Introduction and Heritage of NAVSTAR, the Global Positioning System. Global Positioning System: Theory and Applications, Volume I. American Institute of Aeronautics and Astronautics. *Inc., Cambridge, Massachusetts,*

Parrot, D. 1989. Short-arc orbit improvement for GPS satellites. *Geodesy and Geomatics Engineering Technical Reports; 143,*

Persson, C. G. 1980. *MINQUE and related estimators for variance components in linear models,* Stockholm, Royal Institute of Technology.

Petit, G. & Luzum, B. 2010. IERS conventions (2010). DTIC Document.

Petrovic, S., Barthelmes, F. & Pflug, H. 2013. Airborne and shipborne gravimetry at GFZ with emphasis on the GEOHALO project. *IAG Scientific Assembly 2013.* Potsdam, Germany.

Radicella, S. & Leitinger, R. 2001. The evolution of the DGR approach to model electron density profiles. *Advances in Space Research,* 27**,** 35-40

Revnivykh, S. 2012. GLONASS Status and Modernization. *International GNSS Committee IGC-7.* Beijing.

Roßbach, U. 2001. *Positioning and navigation using the Russian satellite system GLONASS.* Ph.D Thesis, Univ. d. Bundeswehr München.

Rothacher, M. 2001. Comparison of absolute and relative antenna phase center variations. *GPS solutions,* 4**,** 55-60

Saastamoinen, J. 1972. Contributions to the theory of atmospheric refraction. *Bulletin Geodesique,* 105**,** 279-298

Sahin, M., Cross, P. A. & Sellers, P. C. 1992. Variance component estimation applied to satellite laser ranging. *Bulletin Geodesique,* 66**,** 284-295

Schüler, T. 2001. *On ground-based GPS tropospheric delay estimation.* Ph. D, Univ. der Bundeswehr München.

Schaffrin, B. 1997. Reliability measures for correlated observations. *Journal of Surveying Engineering,* 123**,** 126-137

Schaffrin, B. Some generalized equivalence theorems for least-squares adjustment. *In:* Sanso, F., ed. V Hotine-Marussi Symposium on Mathematical Geodesy, 2004. Springer, 107-112.

Schaffrin, B. & Grafarend, E. 1986. Generating classes of equivalent linear models by nuisance parameter elimination. *Manuscripta geodaetica,* 11**,** 262-271

Scheinert, M., Petrovic, S., Heyde, I., Barthelmes, F. & GEOHALO, G. 2013. The geodetic - geophysical flight mission GEOHALO: Results of airborne gravimetry and further geodetic products. *IAG Scientific Assembly 2013.* Potsdam, Germany.

Schmid, R., Steigenberger, P., Gendt, G., Ge, M. & Rothacher, M. 2007. Generation of a consistent absolute phase-center correction model for GPS receiver and satellite antennas. *Journal of Geodesy,* 81**,** 781-798

Schwarz, K. P., Cannon, M. E. & Wong, R. V. C. 1989. A comparison of GPS kinematic models for the determination of position and velocity along a trajectory. *Manuscripta geodaetica*, 14**,** 345-353

Schwarz, K. P. & Wei, M. 1995. Some unsolved problems in airborne gravimetry. *In:* Sünkel, H. (ed.) *Gravity and Geoid.* Berlin, Heidelberg: Springer.

Seeber, G. 2003. *Satellite geodesy: foundations, methods, and applications*, Walter de Gruyter.

Semmling, A. M., Beckheinrich, J., Wickert, J., Beyerle, G., Schön, S., Fabra, F., Pflug, H., He, K., Schwabe, J. & Scheinert, M. 2014. Sea surface topography retrieved from GNSS reflectometry phase data of the GEOHALO flight mission. *Geophysical Research Letters*,

Semmling, A. M., Beyerle, G., Schön, S., Beckheinrich, J., Wickert, J. & Scheinert, M. 2013. Airborne GNSS Reflectometry for Sea Surface Height Estimation as part of the GEOHALO Mission. *IAG Scientific Assembly 2013.* Potsdam, Germany.

Serrano, L., Kim, D. & Langley, R. B. 2004a. A single GPS receiver as a real-time, accurate velocity and acceleration sensor. *Proceedings of the 17th International Technical Meeting of the Satellite Division of the Institute of navigation.*

Serrano, L., Kim, D., Langley, R. B., Itani, K. & Ueno, M. 2004b. A gps velocity sensor: how accurate can it be?–a first look. *ION NTM.* San Diego, CA.

Shen, Y. & Xu, G. 2008. Simplified equivalent representation of GPS observation equations. *GPS Solutions*, 12**,** 99-108

Shi, C., Zhao, Q., Hu, Z. & Liu, J. 2013. Precise relative positioning using real tracking data from COMPASS GEO and IGSO satellites. *GPS solutions*, 17**,** 103-119

Shi, J. & Cannon, M. 1995. Critical error effects and analysis in carrier phase-based airborne GPS positioning over large areas. *Bulletin géodésique*, 69**,** 261-273

Shi, W. 2010. *Principles of modeling uncertainties in spatial data and spatial analyses*, CRC Press.

Simon, D. & Chia, T. L. 2002. Kalman filtering with state equality constraints. *Aerospace and Electronic Systems, IEEE Transactions on*, 38**,** 128-136

Simsky, A. & Boon, F. 2003. Carrier Phase and Doppler-Based Algorithms for Real-Time Standalone Positioning. *Proceedings of the GNSS 2003.* Graz, Austria.

Singh, D., Ghosh, J. K. & Kashyap, D. 2014. Precipitable water vapor estimation in India from GPS-derived zenith delays using radiosonde data. *Meteorology and Atmospheric Physics*, 123**,** 209-220

Snay, R. A. & Soler, T. 2008. Continuously operating reference station (CORS): history, applications, and future enhancements. *Journal of Surveying Engineering*, 134**,** 95-104

Stephenson, S., Meng, X., Moore, T., Baxendale, A. & Edwards, T. 2011. Precision of Network Real Time Kinematic Positioning for Intelligent Transport Systems. *European Navigation Conference.*

Stombaugh, T. S. & Clement, B. R. 1999. *Unraveling the GPS Mystery* [Online]. Ohio State University. Available: http://ohioline.osu.edu/aex-fact/0560.html [Accessed 02. 11 2013].

Szarmes, M., Ryan, S., Lachapelle, G. & Fenton, P. 1997. DGPS high accuracy aircraft velocity determination using Doppler measurements. *Proceedings of the International Symposium on Kinematic Systems (KIS).* Banff, AB, Canada.

Tahk, M. & Speyer, J. L. 1990. Target tracking problems subject to kinematic constraints. *Automatic Control, IEEE Transactions on*, 35**,** 324-326

Takasu, T. 2013. *RTKLIB ver 2.4.2* [Online]. Available: http://www.rtklib.com/prog/manual_2.4.2.pdf [Accessed 01.05 2014].

Teunissen, P. J. G. & Amiri-Simkooei, A. R. 2008. Least-squares variance component estimation. *Journal of Geodesy*, 82**,** 65-82

Teunissen, P. J. G., De Jonge, P. J. & Tiberius, C. C. J. M. 1996. The Volume of the GPS Ambiguity Search Space and its Relevance for Integer Ambiguty Resolution. *PROCEEDINGS OF ION GPS.* Citeseer.

Teunissen, P. J. G., Joosten, P. & Odijk, D. 1999. The reliability of GPS ambiguity resolution. *GPS Solutions*, 2**,** 63-69

Teunissen, P. J. G. & Kleusberg, A. 1998. *GPS for Geodesy,* Berlin, Heidelberg, Springer.

Teunissen, P. J. G., Odijk, D. & Zhang, B. 2010. PPP-RTK: Results of CORS network-based PPP with integer ambiguity resolution. *J Aeronaut Astronaut Aviat Ser A,* 42**,** 223-230

Thompson, L. G. D. & LaCoste, L. J. B. 1960. Aerial gravity measurements. *Journal of Geophysical Research,* 65**,** 305-322

Tiemeyer, B., Cannon, M., Lachapelle, G. & Schanzer, G. 1994. Satellite navigation for high precision aircraft navigation with emphasis on atmospheric effects. *Position Location and Navigation Symposium.* IEEE.

Torge, W. 1989. *Gravimetry,* Berlin; New York, Walter de Gruyter & Co.

Vennebusch, M., Böckmann, S. & Nothnagel, A. 2007. The contribution of very long baseline interferometry to ITRF2005. *Journal of Geodesy,* 81**,** 553-564

Wübbena, G. 1985. Software developments for geodetic positioning with GPS using TI-4100 code and carrier measurements. *In:* Goad, C. (ed.) *Proceedings of the First International Symposium on Precise Positioning with the Global Positioning System.* Rockville, Maryland: U.S. Department of Commerce.

Wübbena, G., Bagge, A., Seeber, G., Boeder, V. & Hankemeier, P. 1996. Reducing distance dependent errors for real-time precise DGPS applications by establishing reference station networks. *In Proceedings of the 9th International Technical Meeting of the Satellite Division of the Instiute of Navigation.* Kansas City, Missouri: Institute of Navigation.

Wang, J., Gopaul, N. & Scherzinger, B. 2009a. Simplified algorithms of variance component estimation for static and kinematic GPS single point positioning. *Journal of Global Positioning Systems,* 8**,** 43-52

Wang, J., Rizos, C., Stewart, M. P. & Leick, A. 2001. GPS and GLONASS integration: modeling and ambiguity resolution issues. *GPS solutions,* 5**,** 55-64

Wang, Q. & Xu, T. 2011. Combining GPS carrier phase and Doppler observations for precise velocity determination. *Science China Physics, Mechanics and Astronomy,* 54**,** 1022-1028

Wang, Q., Xu, T. & Xu, G. 2010. HALO_GPS (High Altitude and Long Range Airborne GPS Positioning Software)-Software User Manual. Potsdam, Germany: GeoForschungsZentrum.

Wang, Q., Xu, T. & Xu, G. 2011. Adaptively changing reference station algorithm and its application in GPS long range airborne kinematic relative positioning. *Acta Geodaetica et Cartographica Sinica,* 4**,** 429-434 (In Chinese)

Wang, X., Ji, J. & Li, Y. 2009b. The applicability analysis of troposphere delay error model in GPS positioning. *Aircraft Engineering and Aerospace Technology,* 81**,** 445-451

Wei, Z. & Ge, M. 1998. *Mathematical model for GPS relative positioning,* Beijing, China, Surveying and Mapping Press (In Chinese).

Wielgosz, P., Kashani, I. & Grejner-Brzezinska, D. 2005. Analysis of long-range network RTK during a severe ionospheric storm. *Journal of Geodesy,* 79**,** 524-531

Xu, G. 2002. GPS data processing with equivalent observation equations. *GPS solutions,* 6**,** 28-33

Xu, G. 2004. MFGsoft Software User Manual. *Version of 2004.* Potsdam, Germany: Geoforschungszentrum.

Xu, G. 2007. *GPS: Theory,Algorithms and Applications,* Berlin, Heideberg, New York, Springer.

Xu, G., Shen, Y., Yang, Y., Sun, H., Zhang, Q., Guo, J. & Yeh, T.-K. 2010. Equivalence of GPS Algorithms and Its Inference. *In:* Xu, G. (ed.) *Sciences of Geodesy-I Advances and Future Direcitons.* Heidelberg, New York: Springer.

Xu, P., Liu, Y., Shen, Y. & Fukuda, Y. 2007. Estimability analysis of variance and covariance components. *Journal of Geodesy,* 81**,** 593-602

Xu, T., He, K. & Xu, G. 2012. Orbit determination and thrust force modeling for a maneuvered GEO satellite using two-way adaptive Kalman filtering. *Science China Physics, Mechanics and Astronomy,* 55**,** 738-743

Yang, Y. 1991. Robust bayesian estimation. *Bulletin géodésique,* 65**,** 145-150

Yang, Y. 1994. Robust estimation for dependent observations. *Manuscripta geodaetica,* 19**,** 10-17

Yang, Y. 2010. Adaptively robust kalman filters with applications in navigation. *In:* Xu, G. (ed.) *Sciences of Geodesy-I Advances and Future Directions.* Heidelberg, Dordrecht, London, New York: Springer.

Yang, Y., Cheng, M. K., Shum, C. K. & Tapley, B. D. 1999. Robust estimation of systematic errors of satellite laser range. *Journal of Geodesy,* 73**,** 345-349

Yang, Y., Gao, W. & Zhang, X. 2010. Robust Kalman filtering with constraints: a case study for integrated navigation. *Journal of Geodesy,* 84**,** 373-381

Yang, Y., He, H. & Xu, G. 2001. Adaptively robust filtering for kinematic geodetic positioning. *Journal of Geodesy,* 75**,** 109-116

Yang, Y., Li, J., Xu, J., Tang, J., Guo, H. & He, H. 2011a. Contribution of the compass satellite navigation system to global PNT users. *Chinese Science Bulletin,* 56**,** 2813-2819

Yang, Y., Xu, T. & Song, L. 2005. Robust estimation of variance components with application in global positioning system network adjustment. *Journal of surveying engineering,* 131**,** 107-112

Yang, Y., Zhang, X. & Xu, J. 2011b. Adaptively constrained Kalman filtering for navigation applications. *Survey Review,* 43**,** 370-381

Zhang, B., Teunissen, P. J. & Odijk, D. 2011a. A novel un-differenced PPP-RTK concept. *J. Navig,* 64**,** S180-S191

Zhang, J. 2007. *Precise velocity and acceleration determination using a standalone GPS receiver in real time.* Ph.D, Royal Melbourne Institute of Technology.

Zhang, J., Zhang, K., Grenfell, R. & Deakin, R. 2006. Short note: On the relativistic Doppler effect for precise velocity determination using GPS. *Journal of Geodesy,* 80**,** 104-110

Zhang, J., Zhang, K., Grenfell, R., Li, Y. & Deakin, R. 2005. Real-time Doppler/Doppler rate derivation for dynamic applications. *Journal of Global Positioning Syetems,* 4**,** 95-105

Zhang, X. & Andersen, O. B. 2006. Surface ice flow velocity and tide retrieval of the Amery ice shelf using precise point positioning. *Journal of Geodesy,* 80**,** 171-176

Zhang, X., Guo, B., Guo, F. & Du, C. 2013. Influence of clock jump on the velocity and acceleration estimation with a single GPS receiver based on carrier-phase-derived Doppler. *GPS solutions,* 17**,** 549-559

Zhang, X., Li, X. & Guo, F. 2011b. Satellite clock estimation at 1 Hz for realtime kinematic PPP applications. *GPS solutions,* 15**,** 315-324

Zhao, Q., Guo, J., Li, M., Qu, L., Hu, Z., Shi, C. & Liu, J. 2013. Initial results of precise orbit and clock determination for COMPASS navigation satellite system. *Journal of Geodesy,* 87**,** 475-486

Zhou, J. 1985. On the Jie factor. *Acta Geodaetica et Geophysica,* 5**,** (In Chinese)

Zhou, J. 1989. Classical theory of errors and robust estimation. *Acta Geodetica Et Cartographica Sinica,* 18**,** 115-120, (In Chinese)

Zumberge, J., Heflin, M., Jefferson, D., Watkins, M. & Webb, F. 1997. Precise point positioning for the efficient and robust analysis of GPS data from large networks. *Journal of Geophysical Research,* 102**,** 5005-5017

Acknowledgments

The completion of this thesis would not have been possible without the support of many people and organizations.

First of all I would like to express my profound respect and gratitude to my supervisors, Prof. Dr.-Ing. Frank Neitzel of Berlin University of Technology (TU Berlin) and Prof. h.c. Dr.-Ing. Guochang Xu (formerly German Research Centre for Geosciences (GFZ), now Shandong University Weihai Branch (SDUW) in China), for supervising this thesis, for their continuous support, guidance and encouragement of my studies and research. They were always willing to share their insights with me and were patient with every question.

I am grateful to Prof. Dr. Frank Flechtner, head of GFZ Section 1.2 for his kindly help, organization of my work and improvements of my publication. Particularly I would like to thank my GFZ colleague Dr. Christoph Förste for his critical comments and helpful suggestions to improve the English in this thesis. Furthermore, the German abstract was translated by Dr. Christoph Förste since I am not very familiar with the German language.

My special words of thanks should go to Prof. Dr.-Ing. Dr. h.c. Harald Schuh and Prof. Dr.-Ing. Frank Flechtner of GFZ and TU Berlin, Prof. Dr.-Ing. Frank Neitzel of TU Berlin, and Prof. Dr. Phil. nat. Markus Rothacher of ETH Zürich for reviewing the thesis and attending dissertation defense.

I owe a special thank to my former GFZ colleague and advisor Dr. Tianhe Xu, whom I thank so much for his continuous and extensive support throughout the last years. His selfless help, detailed guidance and discussion are the source of my forward momentum. I also wish to thank my former GFZ colleagues Dr. Guanwen Huang and Dr. Qianxin Wang for their discussions, which helped to put ideas together.

I would also like to thank my GFZ colleagues Dr. Franz Barthelmes, Mr. Hartmut Pflug, Ms. Angelika Svarovsky, M. Sc. Yan Xu and Dr. Maiko Ritschel. I appreciate their kindly help, cooperation and discussions. I have enjoyed working with all of my colleagues.

Further, many thanks to my GFZ colleagues Dr. Maorong Ge, Dr. Zhiguo Deng, Dr. Jens Wickert, Dr. Maximilian Semmling, Dr. Ming Shangguan, Dr. Xinging Li, and many PhD students of TU Berlin and GFZ, Yumiao Tian, Nan Jiang, LiWah Wong, Rui Tu, Kejie Chen, Hua Chen and others, for their kindly help and discussions.

I am indebted to my host institute GFZ where I was doing my research from 2010 to 2014. TU Berlin is also thanked for my study during this period. The organizers and participants of the GEOHALO campaign are also thanked for kindly providing GNSS data of HALO aircraft. The partners of the International GNSS Service (IGS) are thanked for providing GNSS data and products.

Gratefully acknowledged are the China Scholarship Council (CSC) and the Education Section of the Embassy of the People’s Republic of China in the Federal Republic of Germany, which financially supported the work on my PhD research for four years. Also many thanks to GFZ for financially supporting me in the last four months.

Finally, I would like to express my gratitude to my parents for their endless support and understanding. Also thanks to my sister-in-law and my elder brother for encouraging me to study and helping me to take care of our parents. The person I wish to thank most is my girlfriend, Dr. Lu Zhang, who fills my heart with confidence, courage, and love all the time.

ISSN 2190-7110